OECD/MCCI-2005-TR06

OECD MCCI Project

Final Report

February 28, 2006

by:

M. T. Farmer, S. Lomperski, D. J. Kilsdonk, and R. W. Aeschlimann
Nuclear Engineering Division
Argonne National Laboratory
9700 S. Cass Avenue
Argonne, IL 60439 USA

S. Basu
Project Manager
U.S. Nuclear Regulatory Commission

Table of Contents

Table of Contents (Contd.)

List of Figures

List of Figures

List of Figures

List of Tables

0.0 EXECUTIVE SUMMARY

The purpose of the OECD/MCCI Program was to carry out reactor materials experiments and associated analysis to achieve the following two technical objectives: 1) resolve the ex-vessel debris coolability issue by providing both confirmatory evidence and test data for coolability mechanisms identified in previous integral effect tests, and 2) address remaining uncertainties related to long-term 2-D core-concrete interaction under both wet and dry cavity conditions. This report summarizes the results of eleven reactor material tests that were carried out to achieve these objectives.

In terms of the ex-vessel debris coolability issue, two types of separate effects tests were conducted to provide data on key melt coolability mechanisms that could provide a pathway for achieving long-term debris cooling and stabilization. The results of these tests contributed both confirmatory evidence and test data to support the development and validation of models that form the technical basis for extrapolating to plant conditions. In particular, the Small Scale Water Ingression and Crust Strength (SSWICS) tests provided data on the ability of water to ingress into core material, thereby augmenting the otherwise conduction-limited heat transfer process. Dryout heat flux data obtained from these experiments can be used directly in existing models for evaluating the effect of water ingression on mitigation of ex-vessel accident sequences involving core-concrete interaction. The crust strength data obtained as part of this work can be used to verify the concept of sustained melt/crust contact due to crust instability in the typical 5-6 m cavity span of most power plants.

The Melt Eruption Test (MET) focused on providing data on the melt entrainment coefficient under well-controlled experimental conditions. In particular, the experiment featured an inert basemat with remotely controlled gas sparging, since this is the most important parameter in determining the entrainment rate. Entrainment rate data obtained from this and other tests can be used directly in existing models for evaluating the effect of melt ejection on mitigation of the core-concrete interaction.

In terms of 2-D core-concrete interaction, there is significant uncertainty regarding the lateral vs. axial power split, which is principally due to a lack of experimental data to adequately qualify the computer codes insofar as long-term behavior is concerned. To help bridge this data gap, the approach was to conduct integral effect Core Concrete Interaction (CCI) tests that replicate as close as possible the conditions at plant scale, thereby contributing to the database that can be used to verify and validate the codes directly. To augment the amount of information gathered from these tests, the experiments were flooded from above after a pre-defined concrete ablation depth was reached to provide debris coolability data under conditions involving late phase flooding. The input power levels for the tests were selected so that the heat fluxes from the melt to concrete surfaces and the upper atmosphere were initially in the range of that expected early in the accident sequence (i.e., 150-200 kW/m^2).

The specific findings from the separate effect tests conducted to investigate individual coolability mechanisms are summarized as follows. The SSWICS test results indicate that water is able to ingress into cracks and fissures that form during quench (Figure 0-1), thereby augmenting the otherwise conduction-limited heat transfer rate (Figure 0-2). The effectiveness of this mechanism was found to decrease with increasing corium concrete content, but was not sensitive to concrete type. Surprisingly, the data did not show a significant effect of system pressure on the cooling rate, as would be expected on the basis of particle bed dryout models that are based on the premise of a counter-current flow limitation.

The SSWICS dryout heat flux data was used to empirically adjust and validate the Lister/Epstein dryout heat flux model for direct application to plant accident sequences (Figure 0-3). As part of this work, a simple expression for the crust cracking temperature was developed on the basis of the crust mechanical properties. This definition, in conjunction with the adjustment of a single empirical constant, allows the dryout limit to be evaluated for a wide range of compositions based on the corium and coolant thermophysical properties alone.

The SSWICS crust strength data demonstrated that the actual mechanical strength of core material quenched by an overlying water pool is far weaker (by as much as two orders of magnitude) than that estimated for solid corium. This indicates that the crack structure formed during quench, not the composition, is the main determinant of crust strength. Moreover, extrapolation of the data indicates that a plant-scale crust would not be mechanically stable. Rather, it will most likely fail and reestablish contact with the melt. Therefore, for plant accident conditions, the continued contact between the melt and crust may allow water ingression and melt eruption cooling mechanisms to proceed and contribute to termination of the core-concrete interaction.

In terms of the MET investigation of the melt eruption cooling mechanism, the reactor

Figure 0-1. Sectioned SSWICS Ingot Showing Crack Structure.

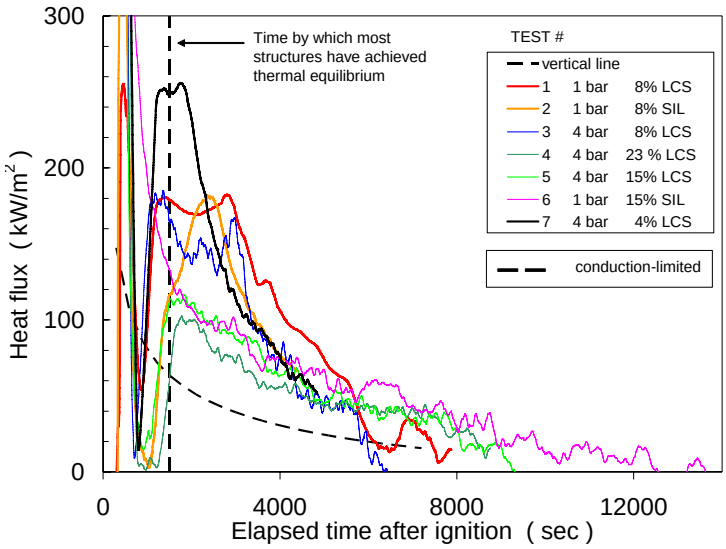

Figure 0-2. SSWICS Heat Flux Data.

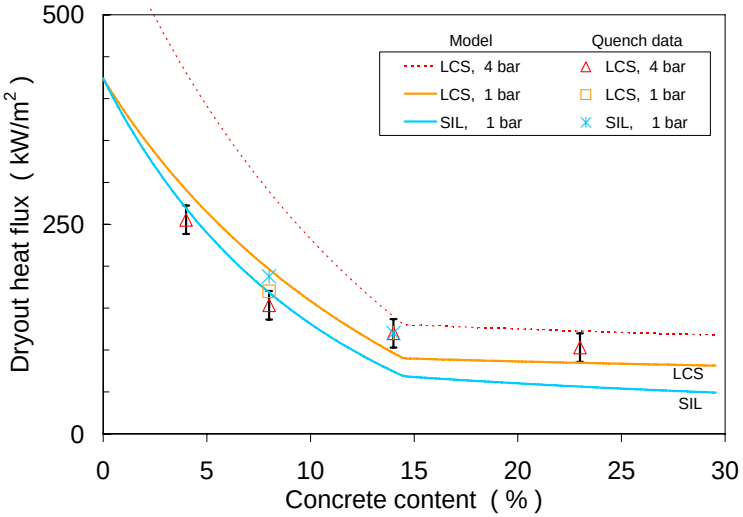

Figure 0-3. Lister/Epstein Model Compared to SSWICS Data.

material database was reviewed to provide a technical basis for model development and validation activities. This review indicated that the database includes both siliceous and limestone/common sand concrete types. Melt eruption data was obtained for all tests (both integral and separate effect) conducted with limestone/common sand concrete. The melt entrainment coefficients ranged from 0.06 to 0.25 %; the melts contained from 8 to 60 wt % LCS concrete. The entrainment data obtained as part of the CCI-2 experiment was particularly important since the eruptions occurred while the crust was floating and the input power was decreasing, so that the melt zone was not over-powered during the eruption process. Thus, the entrainment coefficient estimate for this test is believed to be representative of prototypic conditions.

The MET database review further indicated that no spontaneous eruptions occurred after cavity flooding for the three tests conducted with siliceous concrete. As discussed by Bonnet and Seiler, the gas sparging rate during core-concrete interaction is the key parameter influencing the melt entrainment process. Thus, the reduced gas content for this concrete type may have been a key contributor to the lack of eruptions for these three tests. This review also indicated that test occurrences (i.e., crust anchoring and early termination of power input) may have precluded eruptions from occurring in the tests with this concrete type.

Aside from the separate effect tests, the CCI tests featured late phase flooding to provide integral effect coolability data after ablation had proceeded for some time. In terms of phenomenology, the tests provided data on the bulk cooling, water ingression, melt eruption, and transient crust breach cooling mechanisms. In addition, Test CCI-2 provided data on water ingress at the interface between the core material and concrete sidewalls. This mechanism had been previously identified in the COTELS reactor material test series. Principal findings from these tests related to debris coolability are summarized as follows.

The heat flux during the five minute interval following cavity flooding was high for all tests (Figure 0-4). For the two tests conducted with siliceous concrete, the initial heat fluxes were close to the Critical Heat Flux (CHF) limitation of ~ 1 MW/m^2 under saturated boiling conditions. Thus, the heat fluxes were indicative of quenching of the upper surface crust that was present as an initial condition for both tests. However, for test CCI-2, the upper surface was essentially devoid of a surface crust when water was introduced. Thus, water was able to directly contact the melt, resulting in a bulk cooling transient in which the initial cooling rate approached 3 MW/m^2. The heat flux eventually fell below 1 MW/m^2 after ~ 5 minutes. At this time, a stable crust most likely formed at the melt-water interface, thereby terminating the bulk cooling transient.

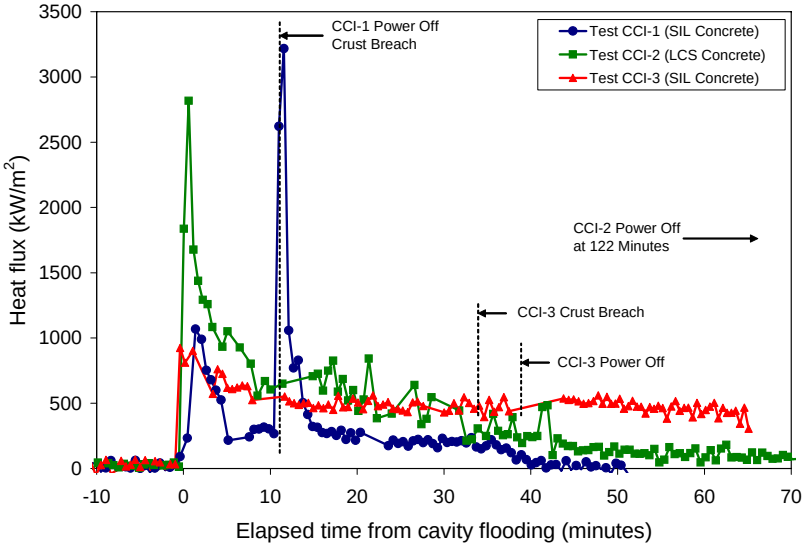

Figure 0-4. Debris/Water Heat Flux for CCI Tests.

The CCI tests did not generally exhibit a decrease

in overall melt temperature after cavity flooding (Figure 0-5). This is despite the fact that the heat flux and power supply responses both indicated substantial debris cooling. This type of behavior can be rationalized by a latent heat transfer process in which a quench front develops at the melt/water interface, as opposed to a sensible heat transfer process in which the entire melt mass is cooled by convective heat transfer with the heat dissipated to the overlying water by conduction across a thin crust at the melt/water interface. The posttest debris morphologies were also consistent with development of quenched debris zones, as opposed to bulk cooldown of the entire melt mass by conduction-limited cooling across a thin crust.

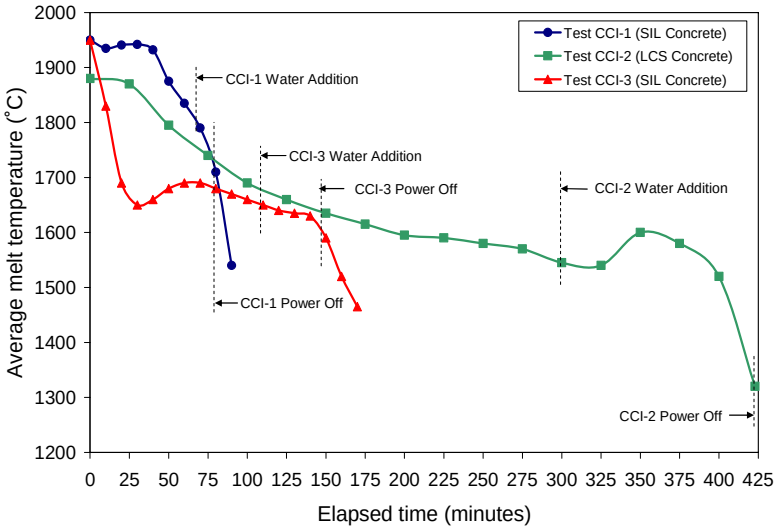

Figure 0-5. Melt Temperatures for CCI Tests.

After the initial transient, the debris/water heat fluxes measured during the CCI tests ranged from 250 to 650 kW/m^2. Heat fluxes for both siliceous concrete tests were lower than the test conducted with LCS concrete. In general, the data indicates that the heat flux increases with concrete gas content. The heat fluxes realized in the tests were several times higher than that predicted by the SSWICS water ingression correlation. Thus, the data suggests that the degree of interconnected cracks/fissures/porosity that form the pathway for water to ingress into solidifying core material is increased by the presence of gas sparging, particularly for the case in which the melt contains a high concrete fraction (e.g., > 15 wt %).

Aside from the water ingression mechanism, the CCI tests also provided integral data on the melt eruption cooling mechanism. As noted earlier, significant eruptions were observed for Test CCI-2. However, no spontaneous eruptions were observed after cavity flooding for the two tests conducted with siliceous concrete. The melt entrainment coefficient for CCI-2 was ~ 0.11 %, which is in the range of that required to stabilize a core-concrete interaction over a fairly significant range of melt depths.

In terms of the crust breach cooling mechanism, both siliceous concrete tests provided data on *in-situ* crust strength, while Test CCI-1 also provided data on the extent of cooling after crust breach. The data indicates that crust material formed during quench is very weak. This finding is consistent with the SSWICS test series crust strength measurements. However, the CCI strength measurements were significant because they were carried out under prototypic temperature boundary conditions before the material had cooled to room temperature.

Aside from the strength measurements, the crust breach event in CCI-3 caused a significant transient increase in the debris cooling rate. In particular, a large melt eruption occurred, resulting in a heat flux peak that exceeded 3 MW/m^2. After the breach, the heat flux steadily declined over the next five minutes to a plateau in the range of 250-300 kW/m^2, which is similar to the plateau observed prior to breach. In general, the data indicates that breach events may lead to significant transient increases in the debris cooling rate at plant scale.

Aside from providing valuable information for addressing the debris coolability issue, the CCI tests also provided information that can be used to reduce modeling uncertainties related to 2-D core-concrete interaction. Principal findings from the CCI tests in this area are summarized as follows.

All tests showed the overall trend of decreasing melt temperature as ablation progressed, which was due to a heat sink effect as relatively cool concrete slag was introduced into the melt, as well as the increasing heat transfer surface area as the melts expanded into the concrete crucibles. The reduction in melt temperature may have further reflected the evolution of the pool boundary freezing temperature that decreased as additional concrete was eroded into the melt over the course of the tests.

Tests CCI-1 and CCI-2 showed evidence of initial crust formation on the concrete basemat and sidewalls that resulted in an incubation period in which the ablation rates were very low and the melt temperature was relatively stable. Test CCI-3 also showed evidence of initial crust formation on the concrete basemat, but there was no evidence of sidewall crust formation for this test. In all cases, the crusts eventually failed, thereby allowing ablation to proceed. The duration of the incubation period for CCI-1 and CCI-2 appeared to be inversely proportional to concrete gas content, which suggests that crust failure may be driven in part by the mechanical forces that arise from the production of concrete decomposition gases at the core-concrete interface.

The long-term ablation behavior was found to be closely linked to concrete type (Figure 0-6). Lateral and axial ablation rates for the LCS concrete

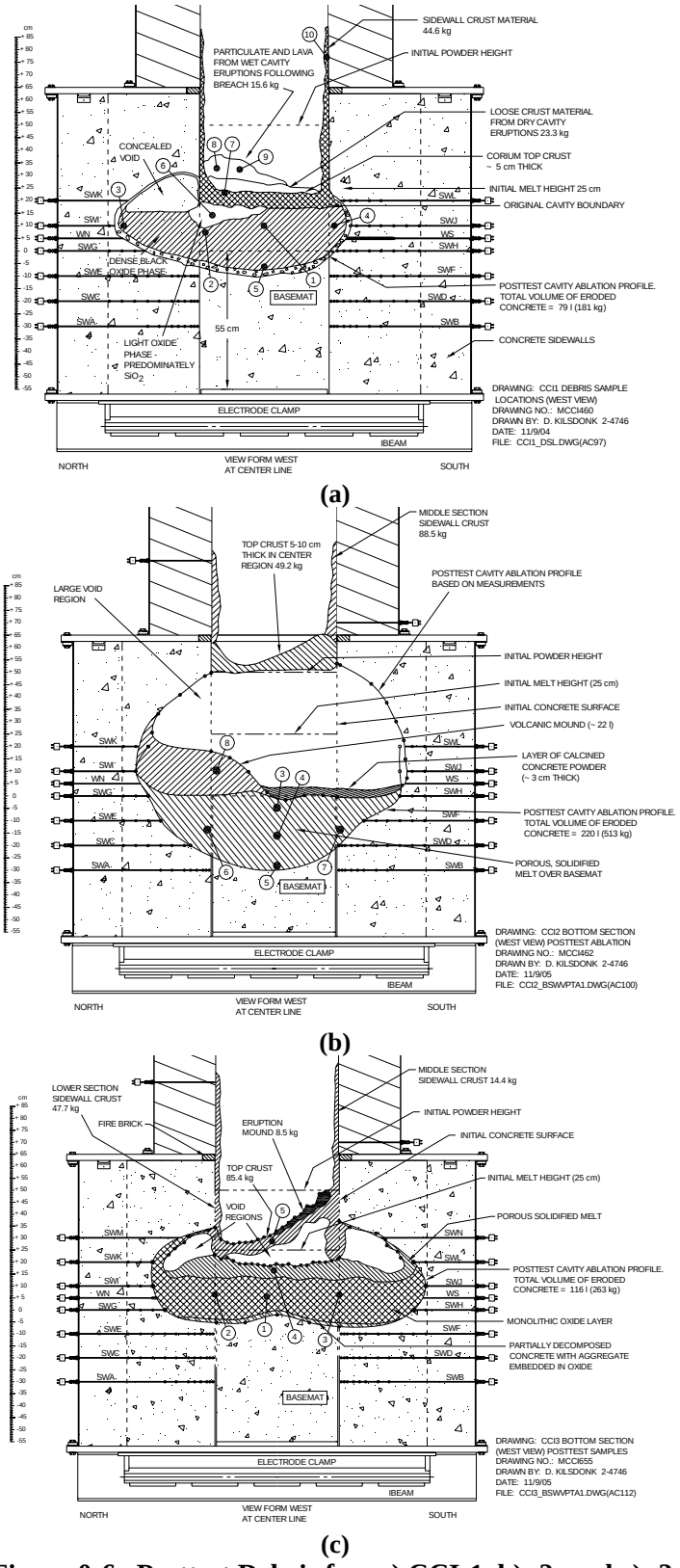

Figure 0-6. Posttest Debris for: a) CCI-1, b) -2, and c) -3.

test were virtually indistinguishable; the concrete erosion rate averaged 4 cm/hr over several hours of interaction before gradually decreasing. The surface heat flux during this time was ~ 60 kW/m^2. Thus, the lateral/axial heat flux ratio for this test was ~ 1.

The relatively uniform power split for CCI-2 can be contrasted with the results of the two tests conducted with siliceous concrete. For test CCI-1, the ablation was highly non-uniform, with most of the ablation concentrated in the North sidewall of the apparatus. Crust stability may have played a major role in determining the ablation progression for this experiment; i.e., the data suggests that after the crust failed on the North concrete sidewall, the input power was predominately dissipated through ablation of this sidewall, while crusts continued to protect the basemat and south sidewall surfaces during the balance of the interaction.

In contrast to Test CCI-1, Test CCI-3 exhibited fairly symmetrical behavior insofar as the progression of lateral ablation is concerned. However, unlike Test CCI-2, the lateral ablation was highly pronounced in comparison to axial ablation. In this regard, the results of tests CCI-1 and CCI-3 are consistent. Lateral ablation in CCI-3 averaged 10 cm/hr over the last hour of the experiment, while the axial ablation rate was limited to 2.5 cm/hr over the same time interval. The corresponding heat fluxes in the lateral and axial directions were 100 and 25 kW/m^2, respectively. On this basis, the lateral/axial surface heat flux ratio for test CCI-3 was estimated as ~ 4, which is significantly higher than the near-unity ratio deduced for test CCI-2 with LCS concrete.

Between the two concrete types used in the CCI tests, possible explanations for differences in the erosion behavior are chemical composition and concrete gas content. A third possible explanation was revealed during posttest examinations. In particular, the core-concrete interface for the siliceous concrete tests consisted of a region where the core oxide had locally displaced the cement that bonded the aggregate (Figure 0-7). Conversely, the ablation front for the LCS test

(a)

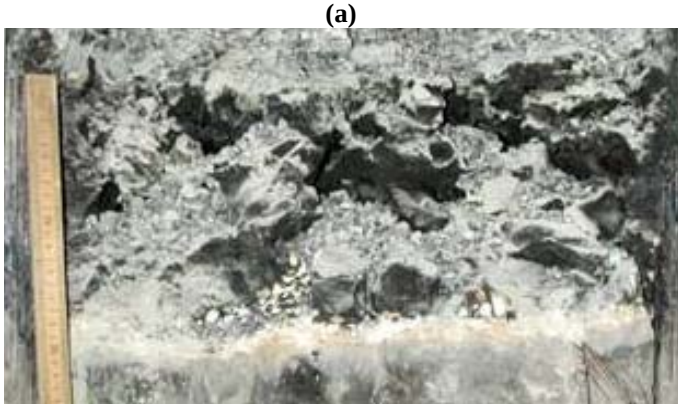

(b)

(c)

Figure 0-7. Debris Morphology for: a) CCI-1, b) -2, and c) -3.

consisted of a powdery interface in which the core and concrete oxides were clearly separated. Variations in the interface characteristics may have influenced the ablation behavior for the two concrete types.

In terms of the chemical analysis results obtained as part of the CCI test series, the corium in the central region of the test section was found to have a higher concentration of core oxides in comparison to that adjacent to the two ablating concrete sidewalls for all tests. Conversely, core oxides were found to be slightly concentrated near the concrete basemat in comparison to that found in the bulk of the corium. For both siliceous concrete tests, two zones appeared to be present: a heavy monolithic oxide phase immediately over the basemat that was enriched in core oxides, with a second overlying light oxide phase that was enriched in concrete oxides. The overlying oxide phase was porous and appeared to have been quenched after the cavity was flooded. This well-defined phase distribution can be contrasted with the debris morphology for CCI-2. In this test, the debris was highly porous and fragmented over the entire axial extent of the material remaining over the basemat (Figure 0-7). This open structure is consistent with the high degree of debris cooling that occurred after cavity flooding.

In terms of the applicability to plant conditions, these tests have provided information that will contribute to the database for reducing modeling uncertainties related to two-dimensional molten core-concrete interaction under both wet and dry cavity conditions. Furthermore, the tests have provided additional confirmatory evidence and test data for coolability mechanisms identified in earlier integral effect tests. Data from this and other test series thus forms the technical basis for developing and validating models of the various cavity erosion and debris cooling mechanisms. These models can then be deployed in integral codes that are able to link the interrelated phenomenological effects, thereby forming the technical basis for extrapolating the results to plant conditions.

One such model was upgraded to include the experimental findings related to debris coolability, and the model was used to scope out an approximate debris coolability envelope for the two concrete types that were evaluated as part of the program. The results for LCS concrete (Figure 0-8) indicate that melt stabilization may be achieved in under one meter of axial ablation as long as the cavity is flooded before the melt concrete content exceeds 15 wt % for initial melt depths ranging up to 40 cm. Under these conditions, stabilization may take up to 10 hours to achieve. However, if flooding is delayed past this point, then the possibility of stabilizing the melt becomes much less likely.

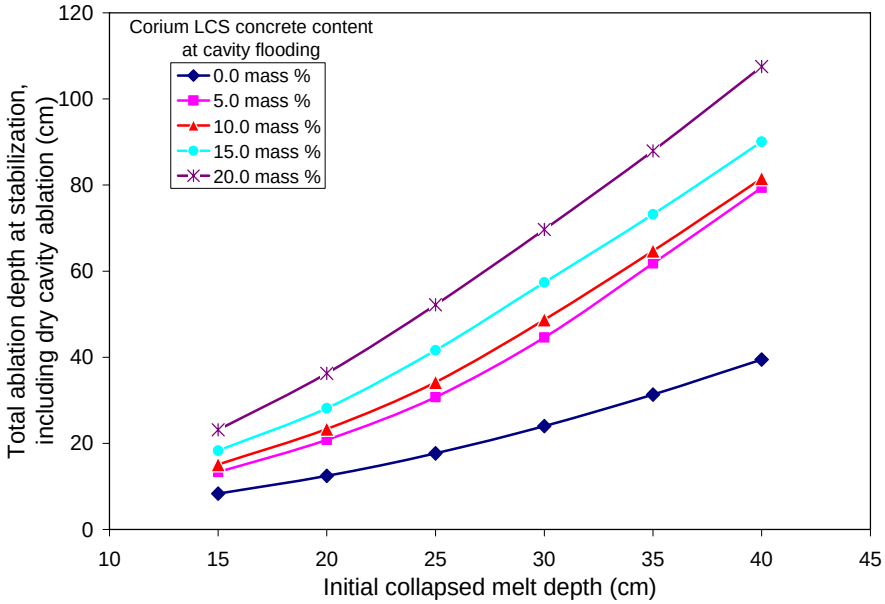

Figure 0-8. Prediction of Maximum Basemat Penetration after Cavity Flooding for LCS Concrete.

For the same set of modeling assumptions, the results for siliceous concrete (Figure 0-9)

indicate a much narrower coolability range. In particular, the results indicate that melt stabilization may not be achieved in under one meter of axial ablation unless the initial melt depth is fairly shallow (i.e., $\leq$ 20 cm), and the cavity is flooded before the melt concrete content exceeds 10 wt %. In this range, coolability may take up to two days to achieve assuming that melt eruptions are active during the quenching process. However, note that spontaneous eruptions have not been observed with water present in experiments conducted to date with this concrete type. Conversely, if the containment design is such that melt depths of up to 40 cm may be encountered, then stabilization may not be achieved unless the design can accommodate up to five meters of axial ablation, and only if the cavity is flooded early (i.e., concrete content $\leq$ 5 wt %). Under these conditions, stabilization will take in excess of one week to achieve. Note again that this result is based on the assumption that melt eruptions are active for the case of siliceous concrete, which has not been experimentally observed.

In summary, the tests carried out as part of this particular program have examined core-concrete interaction and debris coolability for the case of fully oxidized core melts. As a whole, the results of the two-dimensional CCI tests have indicated trends in the ablation front progression that cannot be explained on the basis of our current understanding of the phenomenology involved with this type of physical process. These trends need to be understood before the results can be extrapolated to plant scale. Furthermore, in real plant accident sequences, a significant melt metal fraction could be present that may result in a stratified pool configuration. This type of pool structure was not evaluated in the program. Thus, additional analysis and testing may be required with melts containing a significant metal fraction to further reduce phenomenological uncertainties related to core-concrete interaction, and to evaluate the effects of melt metal content on debris coolability.

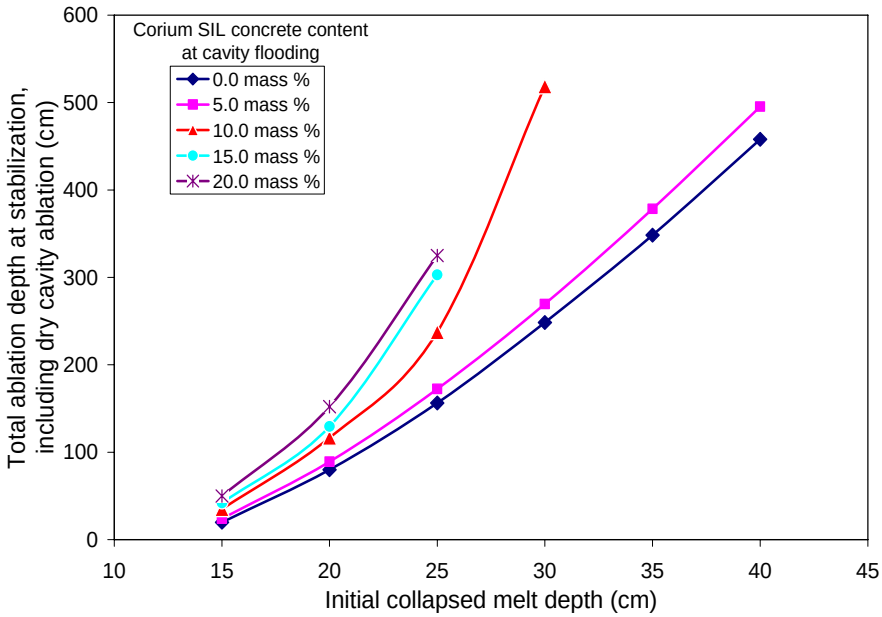

Figure 0-9. Prediction of Maximum Basemat Penetration after Cavity Flooding for Siliceous Concrete.

1.0 INTRODUCTION

1.1 Background

Although extensive research has been conducted over the last several years in the areas of Core-Concrete Interaction (CCI) and debris coolability, two important issues warrant further investigation. The first issue concerns the effectiveness of water in terminating a CCI by flooding the interacting masses from above, thereby quenching the molten core debris and rendering it permanently coolable. This safety issue was investigated in the Melt Attack and Coolability Experiments (MACE) program.[1,2] The approach was to conduct large scale, integral-type reactor materials experiments with core melt masses ranging up to two metric tons. These experiments provided unique, and for the most part repeatable, indications of heat transfer mechanism(s) that could provide long term debris cooling.[2] However, the results did not demonstrate definitively that a melt would always be completely quenched. This was due to the fact that the crust anchored to the test section sidewalls in every test, which led to melt/crust separation, even at the largest test section lateral span of 1.20 m. This decoupling is not expected for a typical reactor cavity, which has a span of 5-6 m. Even though the crust may mechanically bond to the reactor cavity walls, the weight of the coolant and the crust itself is expected to periodically fracture the crust and restore contact with the melt. The fractured crust will provide a pathway for water to recontact the underlying melt, thereby allowing other debris cooling mechanisms (e.g., water ingression and melt eruptions; see Farmer *et al.*[2]) to proceed and contribute to terminating the core-concrete interaction. Thus, one of the key aims of the current program was to measure crust strength to check the hypothesis that a corium crust would not be strong enough to sustain melt/crust separation in a plant accident.

The second important issue concerns long-term, two-dimensional concrete ablation by a prototypic core oxide melt. As discussed by Foit,[3] the existing reactor material database for dry cavity conditions is solely one-dimensional (e.g., see Copus *et al.,*[4] Thompson *et al.,*[5-6] and Fink *et al.*[7]). Although the MACE Scoping Test was carried out with a two-dimensional concrete cavity, the interaction was flooded soon after ablation was initiated to investigate debris coolability.[1] Moreover, due to the scoping nature of this test, the apparatus was minimally instrumented and therefore the results are of limited value from the code validation viewpoint. Aside from the MACE program, the COTELS test series also investigated 2-D CCI under flooded cavity conditions. However, the input power density for these tests was quite high relative to the prototypic case (Nagasaka *et al.*[8]). Finally, the BETA test series provided valuable data on 2-D core concrete interaction under dry cavity conditions, but these tests focused on investigating the interaction of the metallic (steel) phase with concrete (Alsmeyer[9]). Due to these limitations, there is significant uncertainty in the partitioning of energy dissipated for the ablation of concrete in the lateral and axial directions under dry cavity conditions for the case of a core oxide melt (Foit[3]). Accurate knowledge of this "power split" is important in the evaluation of the consequences of an ex-vessel severe accident; e.g., lateral erosion can undermine containment structures, while axial erosion can penetrate the basemat, leading to ground contamination and/or possible containment bypass. As a result of this uncertainty, there are still substantial differences among computer codes in the prediction of 2-D cavity erosion behavior under both wet and dry cavity conditions (Foit[3]). Thus, a second key aim of the current program was to provide the necessary data to help resolve these modeling differences.

1.2 Objectives

In light of the above issues, the OECD-sponsored Melt Coolability and Concrete Interaction (MCCI) program was initiated at Argonne National Laboratory. The project conducted reactor materials experiments and associated analysis to achieve the following technical objectives:

1. resolve the ex-vessel debris coolability issue through a program that focused on providing both confirmatory evidence and test data for the coolability mechanisms identified in previous integral effects tests, and

2. address remaining uncertainties related to long-term 2-D core-concrete interaction under both wet and dry cavity conditions.

Data from the various tests conducted as part of the program is used to develop and validate models and codes that eventually form the basis for extrapolating the experimental findings to plant conditions. Achievement of these technical objectives will demonstrate the efficacy of severe accident management guidelines for existing plants, and provide the technical basis for better containment designs of future plants.

The project completed a total of eleven reactor material tests to investigate melt coolability and 2-D core-concrete interaction mechanisms under both wet and dry cavity conditions. The objectives of this final report are to summarize key findings from the tests, and to evaluate the ramifications of these findings on debris coolability and core-concrete interaction at plant scale.

1.3 Approach

A summary of the three types of experiments that were utilized to meet the overall program objectives is provided in Table 1-1. In terms of the ex-vessel debris coolability issue, two types of separate effects tests were conducted to provide data on key melt coolability mechanisms identified in earlier integral effect tests.[1-2] These cooling mechanisms are summarized in Table 1-2, while a physical illustration of several key mechanisms is provided in Figure 1-1. The results of the tests provided both confirmatory evidence and test data to support the development and validation of models of these mechanisms that form the technical basis for extrapolating to plant conditions. In particular, the Small Scale Water Ingression and Crust Strength (SSWICS) tests[10-11] provided data on the ability of water to ingress into core material, thereby augmenting the otherwise conduction-limited heat transfer rate. Dryout heat flux data obtained from these experiments can be used directly in existing models for evaluating the effect of water ingression on mitigation of ex-vessel accident sequences involving CCI.[12-13] The crust strength data obtained as part of this work was used to validate the concept[11] of sustained melt/crust contact due to crust instability in the typical 5-6 m cavity span of most power plants.

The Melt Eruption Test (MET) focused on providing data on the melt entrainment coefficient under well-controlled experimental conditions. In particular, the experiment featured an inert basemat with remotely controlled gas sparging rate, since this is the most important parameter in determining the entrainment rate.[14] Entrainment rate data obtained from this and

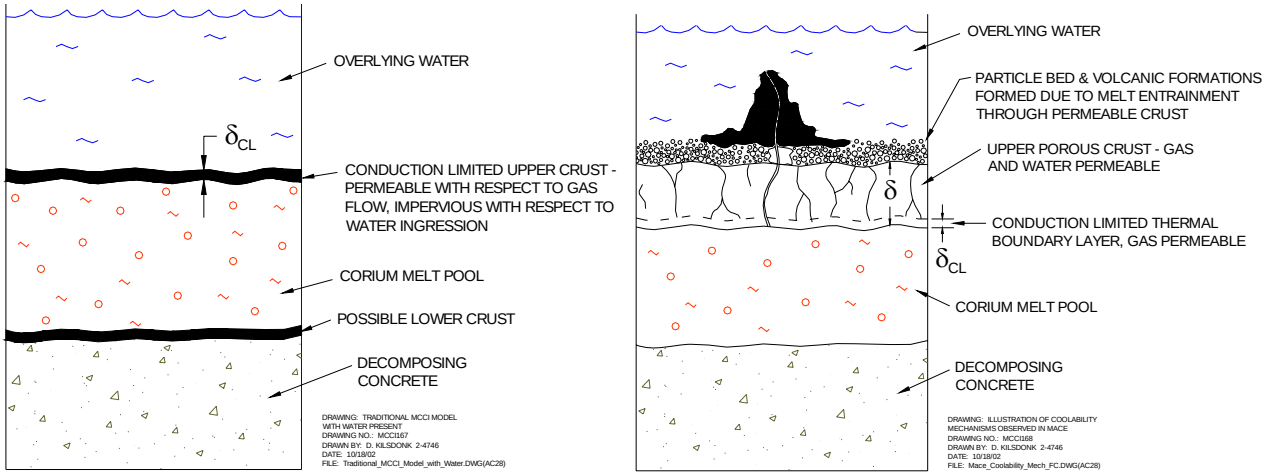

(a) **(b)**

Figure 1-1. CCI with (a) Conduction-Limited Crust at Melt/Water Interface, and (b) Active Coolability Mechanisms at Melt/Water Interface.

Table 1-1. Summary of MCCI Program Tests to Address LWR Safety Issues.

Issue	Experiment	Approach	Research Benefits
Debris Coolability	Melt Eruption Test (MET)	Conduct tests with an inert basemat and controlled gas sparging. Vary melt sparging rate and measure the corresponding melt ejection rate. Parameterize on melt composition since this variable influences the entrainment rate.	• Provide direct measurements of melt entrainment coefficient under well controlled experiment conditions. • Utilize entrainment data in existing models for evaluating the effect of ejections on mitigating accident sequences.
	Small Scale Water Ingression and Crust Strength (SSWICS)	Conduct water ingression tests to determine crust dryout limit; parameterize on melt composition since this is the key factor influencing cracking. Perform strength measurements on crust specimens to determine failure stress after quench.	• Dryout heat flux data can be used in models for evaluating the effect of water ingression on mitigation of accident sequences. • Utilize strength data to confirm that a floating crust boundary condition is applicable at plant scale.
Long Term 2-D CCI	2-D Core-Concrete Interaction (CCI)	Conduct realistic integral 2-D CCI tests to provide direct data for code verification and validation purposes.	• Reduce modeling uncertainties in lateral/axial power split during; resolve differences between codes in predicted 2-D cavity erosion behavior.

other tests can be used directly in existing models[13-14] for evaluating the effect of melt ejection on mitigation of ex-vessel accident sequences.

In terms of 2-D core-concrete interaction behavior, there is significant uncertainty regarding the lateral vs. axial power split,[3] which is principally due to a lack of experimental data to adequately qualify the computer codes insofar as long-term behavior is concerned. To help bridge this data gap, the approach was to conduct integral effect tests that replicated as close as

Table 1-2. Summary of Coolability Mechanisms Observed in MACE Integral Tests.

Mechanism	Description	Experimental Evidence
Bulk Cooling	Melt sparging rate is initially high enough to preclude stable crust formation at melt/water interface, resulting in high heat transfer rates due to conduction and radiation across the agitated (area enhanced) interface. Phase terminated when a stable interfacial crust forms.	High heat transfer rates measured during early phase of the melt-water interaction. Data indicates that a coherent crust cannot form; rather, crust segments are broken up and mixed into melt. Validated models have been developed for this mechanism.
Melt Eruptions	Melt dispersal occurs by an entrainment mechanism where sparging gas carries melt through defects in the crust into the overlying coolant. The dispersed material is quenched as a coolable bed of particles and high surface area volcanic formations.	Eruptions have been observed in all tests conducted with limestone-common sand concrete after crust formation. The particle beds are characterized by high porosity and large particle size.
Water Ingression	Corium shrinkage during quench is ~ 18 vol%. This causes voids/defects to appear in the frozen material. Water penetrates down through the voids/defects, augmenting the otherwise conduction-limited heat transfer process.	Melt/water heat flux far exceeds that which could by transferred by conduction across the (up to 10 cm) thick crusts formed during the tests. Posttest measurements indicate that crusts are permeable.
Crust Breach	Due to water ingression, thick crusts form and bond to the cavity walls. These crusts will not stable in the typical span of most plants. Thus, they will fail, leading to renewed cooling by the above mechanisms.	Partial crust failures observed in MACE integral effects tests. Various structural - mechanical analyses have shown that crusts will not be stable at reactor scale.

possible the conditions expected at plant scale, thereby providing a database that can be used to verify and validate the codes directly. To augment the amount of information gathered from these CCI tests,[15] they were flooded from above after a pre-defined concrete ablation depth was reached to provide debris coolability data under conditions involving late phase flooding. The input power levels were selected so that the heat fluxes from the melt to concrete surfaces and the upper atmosphere were initially in the range of that expected early in the accident sequence (i.e., 150-200 kW/m^2).

The purposes of this final report are to: i) summarize key results from the tests, and ii) evaluate the results in terms of satisfying the overall program objectives described above. To that end, the report begins by providing an overview description of the facilities and key results obtained for each of the test series shown in Table 1-1. Following these presentations, correlations area then presented that capture the key phenomenological findings from the tests. The report then concludes by providing a set of generic plant calculations with a numerical model that has been upgraded to incorporate the phenomenological correlations to determine the efficacy of water in quenching and stabilizing a core-concrete interaction when the interaction is flooded from above. Additional information regarding the apparatuses, procedures, and results are provided in the final reports that were prepared for each test series,[10-11,15] as well as various conference[16-19] and journal[20] papers. A bibliography of all technical reports and refereed publications prepared as part of the program is provided in Appendix A.

2.0 SSWICS TEST SERIES RESULTS

The Small-Scale Water Ingression and Crust Strength (SSWICS) experiments were separate effects tests used to address the ability of water to cool and thermally stabilize a molten core/concrete interaction when the reactants are flooded from above. The tests involved measuring the cooling rate of a 15 cm deep (nominally 75 kg) pool of molten corium with an overlying water layer. The test data was used to determine the extent to which water ingression into the crust increased the melt quench rate above the conduction-limited rate. The experiments provided information on the effects of melt composition and system pressure on the quench rate. The solidified corium ingot produced by the water ingression tests was later removed from the water ingression test apparatus and tested for mechanical strength. The objective of the strength tests was to provide data that could be used to validate the hypothesis that a plant-scale crust over a corium pool would be an unstable structure. The tests involved applying a mechanical load to the corium ingots to measure their mechanical strength. They were loaded along the centerline to the point of fracture. Samples were then taken from the centerline region of the ingot to characterize the phase distribution of the corium constituents. This section is devoted to summarizing the setups and findings of the SSWICS tests. Additional details are provided in final reports on the quench tests[10] and the crust strength measurements.[11]

2.1 Water Ingression Tests

The water ingression phenomenon was studied with an apparatus designed to measure the quench rate of a pool of corium 30 cm in diameter and 15 cm deep. The steel reaction vessel, shown in Figure 2-1, was fitted with MgO liners to protect it from the high temperature corium. Tungsten/rhenium (Type C) thermocouples measured temperatures around the perimeter of the corium melt and within the melt itself. The steam outlet led to a condenser and a collection tank with level measurement instrumentation. Measurement of the time varying liquid level in the condensate tank provided the rate of steam production from the water pool, which was used to calculate the corium cooling rate. A control valve on the steam line regulated system pressure for tests in which the corium was quenched at above-ambient pressure.

The main parameters varied in these tests were melt composition and system pressure. Seven quench tests were successfully conducted with corium melts containing varying amounts of either siliceous or limestone-common sand concrete. The variations in the concrete content represent different phases of a core-concrete interaction following the release of corium from the reactor vessel and initiation of a CCI. The corium was formulated to have a core-to-cladding oxide mass ratio of 2.44, which is typical of most pressurized water reactors. The melts were quenched at a pressure of either one or four bar. The test matrix for the water ingression tests is provided in Table 2-1.

Each test was preceded by a preheat phase (except Tests 1&2) to raise the vessel temperature to 100^{o}C to minimize heat sink influences on the energy balance used to calculate the corium cooling rate. Tests were initiated by igniting the thermite mixture with a current-driven heating coil buried within the powder-like mixture of chemicals. Ignition was detected through the initial rise in the upper plenum gas temperature as hot gases were released from the chemical reaction. The burn front around the coil moved quickly downwards and after ~10 seconds the reaction was detected by thermocouples near the basemat. Figure 2-2 shows the

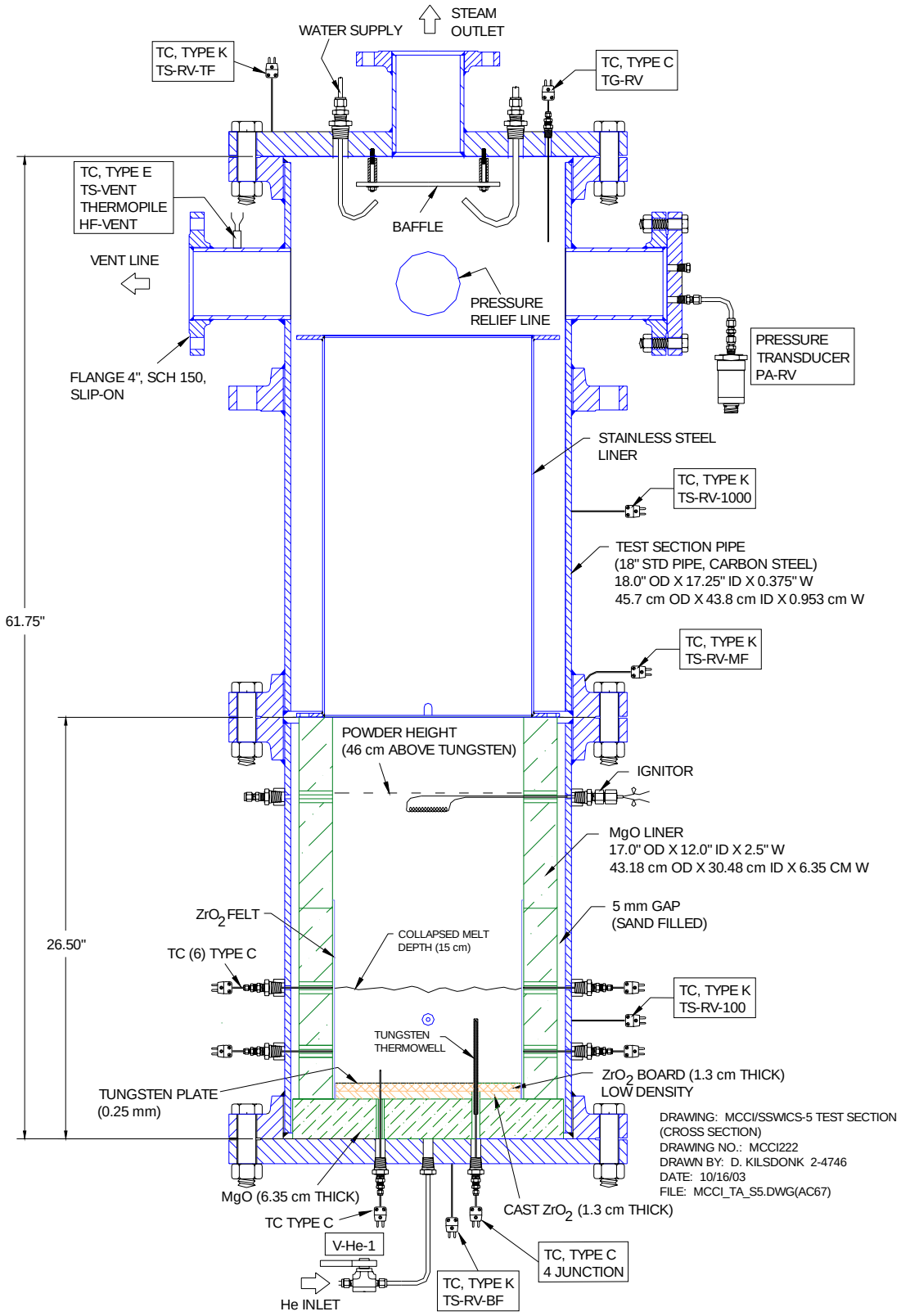

Figure 2-1. Side View of SSWICS Reaction Vessel.

Table 2-1 Summary of SSWICS Test Conditions for Quench Experiments.

Parameter	Test Number						
	1	**2**	**3**	**4**	**5**	**6**	**7**
Melt composition (wt % UO_2/ZrO_2/Cr/concrete)	61/25/6/8	61/25/6/8	61/25/6/8	48/20/9/23	56/23/7/14	56/23/6/14	64/26/6/4
Concrete type	LCS	SIL	LCS	LCS	LCS	SIL	LCS
Melt mass (kg)	75	75	75	60	68	68	80
Melt diameter / depth (cm)	30 / 15	30 / 15	30 / 15	30 / 15	30 / 15	30 /15	30 /15
Basemat type	Inert	Inert	Inert	Inert	Inert	Inert	Inert
Initial melt temperature (^oC)	~2300	~2100	~2100	~2100	~2100	~1950	~2100
Initial vessel and coolant temperature (^oC)	20	20	100	100	100	100	100
System pressure (bar)	1	1	4	4	4	1	4
Water injection period (sec)	665	760	183	195	622	215	194
Water injection flowrate (lpm)	4	4	12	13	6	14	13
Water injected (liters)	33	39	34	40	61	47	40
Condensate collected over course of test (kg)	24.7	16.1	28.9	21.9	22.7	27.6	31.4
Test duration (hours)	2.2	1.2	1.8	2.4	2.6	3.9	1.4

measured melt temperatures during Test 4, which had an initial melt temperature of approximately 2100 ^{o}C. All data is plotted so that the x-axis origin corresponds to the initial rise in the measured upper plenum gas temperature.

The next phase involved coolant injection to establish the water pool over the melt. Water was injected from the top of the upper plenum at a rate in the range of 5-15 l/min and for a duration of several minutes. For Test 4, the regulating valve was activated immediately after injection was completed. This is illustrated in Figure 2-3, which shows the rise in RV pressure following the closure of the water line valve denoted V-quench. Figure 2-4 shows the total amount of water injected into the system, F-integrated, as well as the inventories of the condensate tank and reaction vessel, which were determined by a mass balance.

Once the water injection phase was completed, there were no operator actions until the melt was quenched. The melt was considered quenched, and the test completed, once all basemat thermocouple readings had fallen to the saturation temperature. Sample pictures of solidified corium ingots are provided in Figures 2-5 and 2-6.

Quench Test Data Reduction

The main objective of each quench test was to measure the time-varying heat flux through the corium surface to the overlying layer of water (denoted q). This was compared to the calculated conduction-limited heat flux, q_c, to establish whether heat transfer was enhanced by an active mechanism such as crack propagation within the crust. The corium heat flux was not measured directly, but was derived instead from an energy balance. To a first approximation, all the energy lost from the corium during the quench process can be thought to pass through the corium surface, where it produces boiling in an overlying pool of saturated water. The heat flux at the corium surface is then related to the steam generation rate by the following:

$$q = \frac{1}{A} \dot{m}\, h_{lv} \tag{2-1}$$

where A = corium surface area (0.071 m^2), $\dot{m}$ = mass flow rate of steam from the water pool and h_{lv} = heat of vaporization of water. In an ideal system, all of the vapor produced by the pool boiling will travel to the heat exchanger, where it is condensed and collected in the condensate tank. In this case, the rate of condensate collection is identical to the steaming rate and so a measure of mass flow into the CT can be used to calculate the steaming rate and thus the heat flux. The mass flow rate into the CT is calculated from the time derivative of a differential pressure signal. The surface heat flux is then:

$$q = \frac{1}{A}\frac{1}{g}\frac{\pi}{4} D^2 \frac{\partial \Delta P}{\partial t} h_{lv} \tag{2-2}$$

where D = inner diameter of the CT (0.203 m), ΔP = measured differential pressure, and g = the gravitational constant. The mass flow rate into the CT during the intermediate and later stages of a test was always rather low and produced a very slow rise in tank level. The derivative was calculated with pairs of averaged ΔP readings (an average of 5 measurements at 0.5 Hz) centered on a Δt of 180 s.

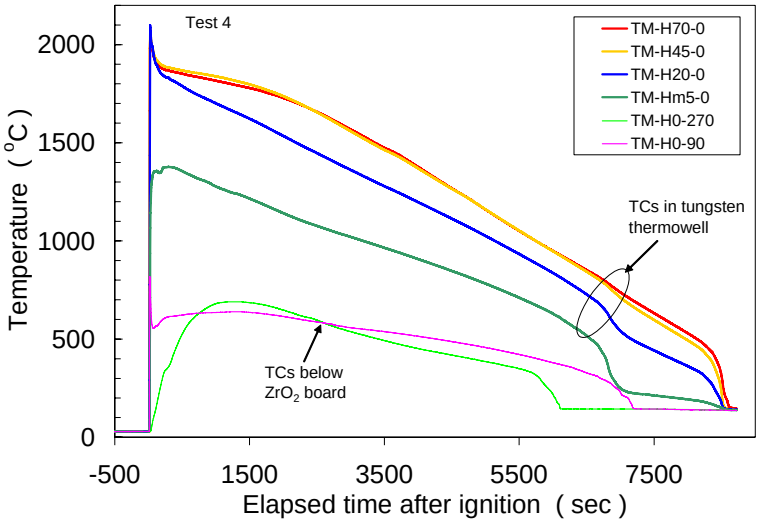

Figure 2-2. Measured Melt Temperatures for Test 4.

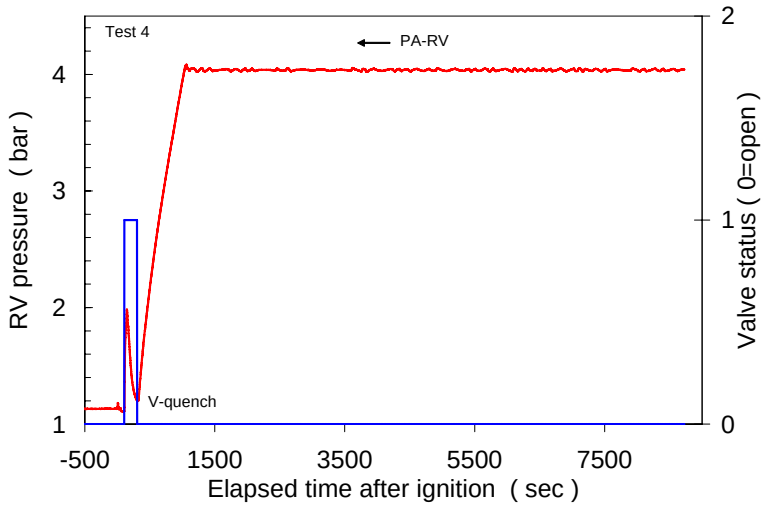

Figure 2-3. Test 4 Reaction Vessel Pressure.

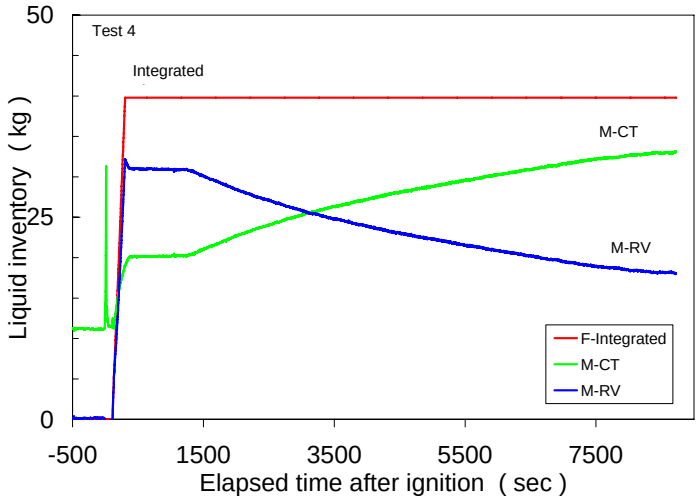

Figure 2-4. Test 4 Coolant Inventory in Reaction Vessel and Condensate Tank.

Figure 2-5. Top View of Test 1 Ingot with 8% LCS Concrete (left) and Test 2 with 8% Siliceous Concrete (right).

Figure 2-6. Bottom View of Test 1 Ingot (left) and Test 2 (right). The Red Material is Sealant Used to Eliminate Water Bypass During the Permeability Tests.

Figures 2-7 and 2-8 show selected test results in the form of heat flux derived from two sets of measurements: 1) the CT ΔP data, and 2) an energy balance on the heat exchanger used to condense the steam. The measured injection flow rate is also plotted to highlight the role of subcooled water addition on the apparent heat flux. The vertical scales of the graphs are expanded to focus on the heat flux after water injection, which is when most transient effects have subsided. Cropped from each plot is the large peak that accompanied initial coolant injection. Heat fluxes during this initial phase were generally of the order of a few MW/m^2, which is characteristic of a critical heat flux limitation for subcooled pool boiling.

The early drop to zero in the heat flux plotted in Figure 2-7 is the result of a temporary loss of steam flow to the HX while the structures and coolant heated to the saturation temperature. This behavior was typical, except during Test 6 (Figure 2-8), which was the only test in which both the coolant and structures were preheated to the saturation temperature. Preheat temperatures and system pressures are included in Table 2-1.

General Assessment of Test Findings

The heat flux data from all seven tests has been combined in Figure 2-9 for comparison. The curves are based on the same type of CT ΔP data used in the preceding figures, but it has been smoothed with a 5-minute moving average to increase the distinctiveness of each curve. Figure 2-10 is similar with 1-minute moving averages plotted on a semi-log scale to include the early phase peaks.

A cross-test comparison of the heat fluxes should be made cautiously because the role of heat sinks varied from test to test. The RV heat capacity was significantly reduced after Test 2 by replacing the MgO upper liner with a less massive steel liner. In addition, both the system preheats and saturation temperatures varied between tests. Still, there is value in comparing the heat fluxes if attention is focused on the latter portion of each transient, when the influence of heat sinks had diminished. A direct comparison is meaningful for the period beyond an elapsed time of ~1500 s because at that time the structures are near thermal equilibrium with the coolant. In addition, pool boiling resumes and so there is no sensible heat addition to the coolant. An inspection of the plotted results for the period beyond ~1500 s leads to the following observations:

1. Cooling rate plateaus are evident for three of the four tests with the highest heat fluxes (1, 3 & 7). This is consistent with the corium cooling rate equilibrating at the dryout limit, as would be expected if water ingression was active during the quench process. It is possible that Test 2, the other high heat flux test, also produced a plateau but that it is obscured by the extended period of heat sink activity.
2. The test with the highest cooling rate plateau, Test 7 with 4% concrete, had the lowest concrete content. The next three highest plateaus are all 8% concrete melts. For the first hour of each transient, there is a clear trend indicating an inverse relationship between cooling rate and mass fraction of concrete in the melt.
3. The three tests with the lowest heat fluxes exhibited no plateau and resemble in form the cooling curve predicted by the 1-D conduction solution. This is the expected result if water ingression is not a significant cooling mechanism and quenching of the melt is dominated by conduction-limited heat transfer. The three tests with the lowest heat fluxes had the highest melt concrete contents (15 and 23%).

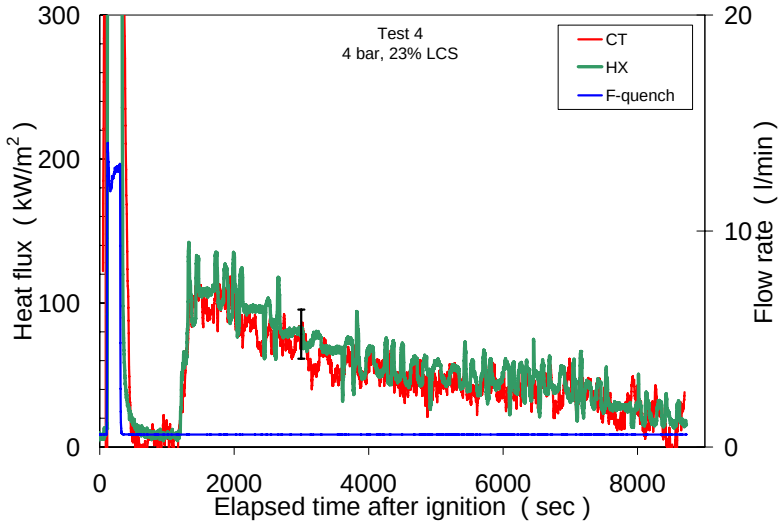

Figure 2-7 Heat Flux for Test 4.

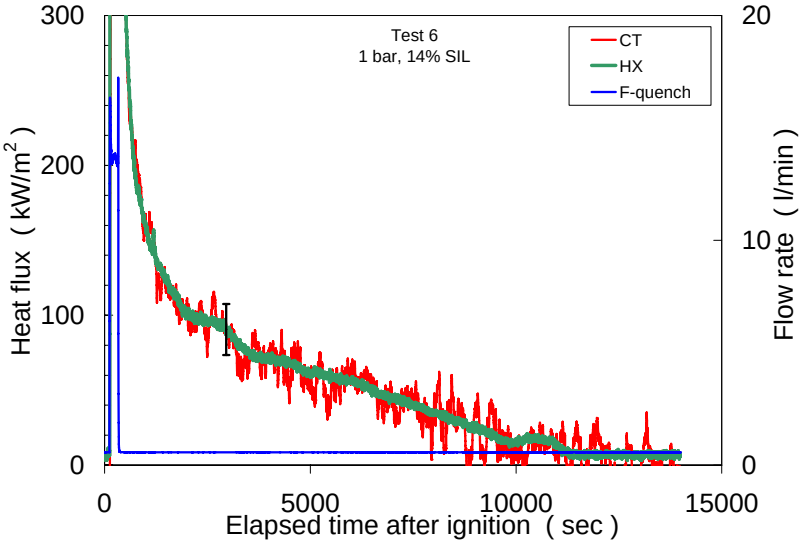

Figure 2-8. Heat Flux for Test 6.

4. The effect of pressure can be considered by comparing Test 1 with Test 3, both of which contained 8% LCS concrete. The heat flux for the 4 bar test is very similar to that of the 1 bar test, which is contrary to the expectation of a significant increase in heat flux with pressure. This suggests that system pressure has little effect on the water ingression rate.

5. Tests 1 and 2 can be used to compare the cooling rate of corium containing siliceous concrete to that having LCS concrete. Both tests were conducted at 1 bar with corium containing 8% concrete. Figure 2-9 shows two similar curves for these tests. Alternatively, if cooling rate is not strongly influenced by system pressure, then Tests 5 & 6 also provide evidence of a composition-influenced cooling rate. The plot shows that the cooling rate for test 5 (15% LCS at 4 bar) was only slightly higher than that of Test 6 (15% siliceous at 1 bar). These findings suggest that the cooling rate for corium containing LCS concrete is comparable to that containing siliceous concrete.

Comparison with Conduction-Limited Cooling

Water ingression-enhanced cooling is identified by comparing the measured corium heat flux with the conduction-limited solution. For an accurate determination of the conduction-limited heat flux, one must account for lateral and axial heat losses that are present during the experiment. An estimate of this heat flux under experimental conditions was made using a 3-D model of the RV lower plenum. The model was constructed using the thermal analyzer SINDA/3D (Network Analysis, Inc.), which is a CAD-type program and a processor for the finite-difference analysis thermal analyzer SINDA/G. Details of the model and boundary conditions used in the calculations are provided elsewhere.[10]

The calculated conduction-limited heat flux has been included in Figure 2-9 for comparison with the data. For all cases, the measured heat flux is significantly higher than the conduction-limited case during the first few thousand seconds of a test. Later, the measured heat flux falls below that of the conduction limited solution, which is expected since the previously enhanced heat flux has left relatively little thermal energy in the melt compared to what would remain if heat transfer were conduction limited. The plot suggests that the corium cooling rate has been enhanced above that of the conduction-limited rate. It is proposed that the enhancement is associated with the water ingression mechanism. And as noted earlier, the observed increase in cooling rate for decreasing melt concrete content supports the notion that the effectiveness of the water ingression mechanism increases with decreasing concrete content. It must be noted, however, that additional analysis is required to identify the precise level of heat flux enhancement associated with water ingression. Steam flow measurements were used to infer the heat flux at the corium surface. However, it is likely that heat losses through the MgO liner supplemented the steam flow and increased the apparent heat flux at the corium surface. Though it is beyond the scope of this study to quantify steam generation due to these heat losses, and thereby arrive at a numerical value for the heat flux associated with water ingression, the data provides an unambiguous measure of the maximum heat flux associated with water ingression.

2.2 Water Percolation Tests

For the case in which water ingression plays a significant role in melt cooling, a plateau in the curve of surface heat flux versus time has been predicted. Several of the water ingression tests do indeed show evidence of an early heat flux plateau. However, because of the transient nature of these tests, a true plateau may be too brief to be easily identifiable, or may not occur at all even with significant water ingression-enhanced cooling. Thus it is of great value to have an alternative, independent method of determining the dryout heat flux. Such a method uses measurement of the permeability of the solidified corium. Previous studies with porous beds have related the dryout heat flux to the permeability of the bed:[21]

$$q''_{dry} = \frac{\kappa \rho_v h_{lv} (\rho_l - \rho_v) g}{2 \mu_v} \tag{2-3}$$

where ρ_l = coolant density, ρ_v = steam density, μ_v = steam dynamic viscosity, and κ = the permeability of the porous medium. Water percolation tests were used to measure the permeability of the corium ingots produced in the quench experiments. A dryout heat flux was

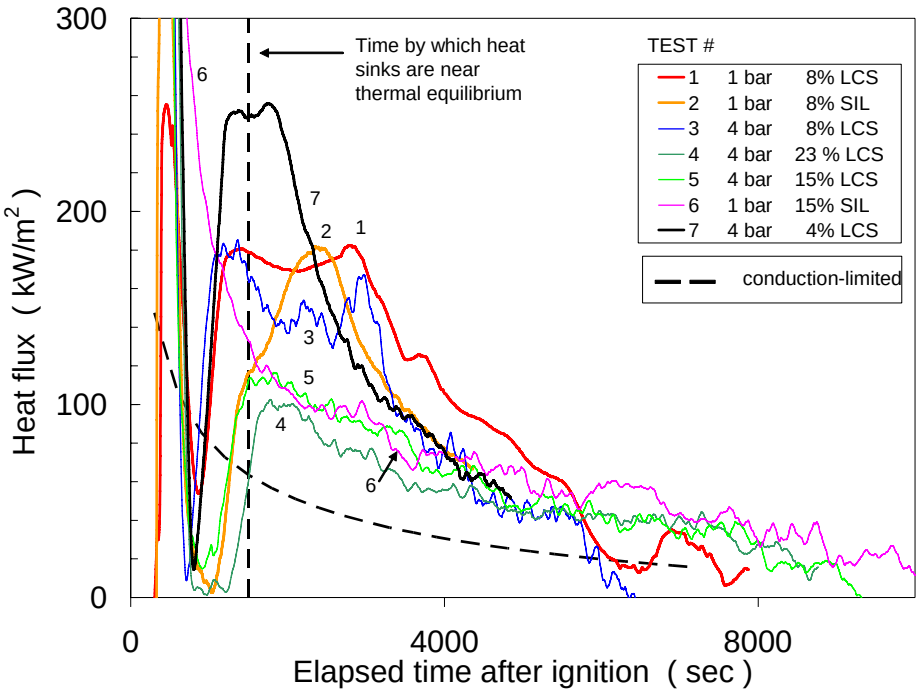

Figure 2-9. Heat Flux Derived from CT ΔP Data Plotted as 5 Minute Moving Averages.

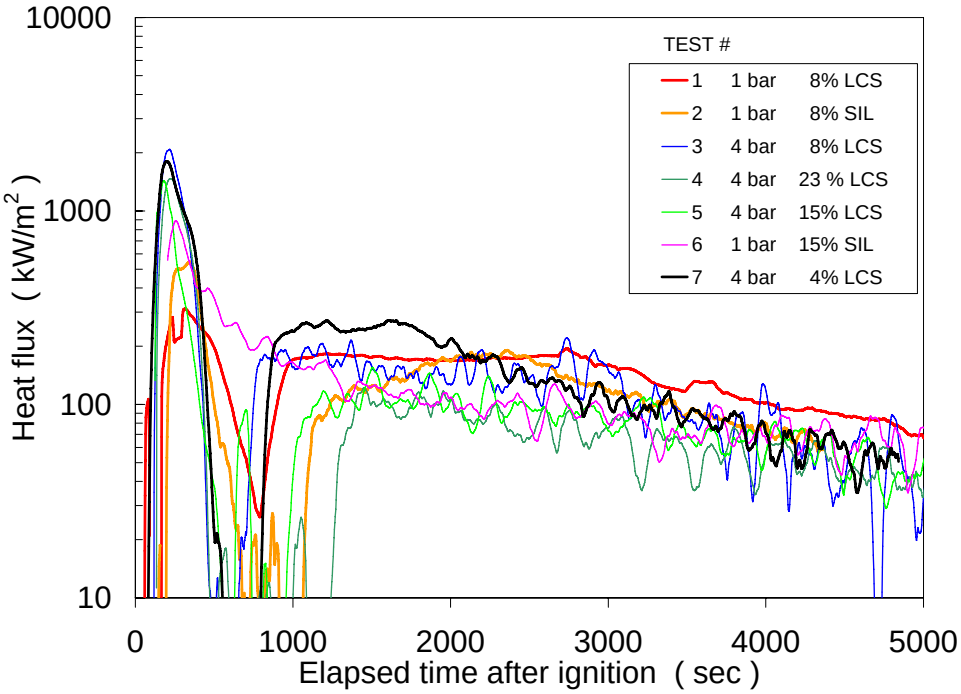

Figure 2-10. Heat Flux Data as 1 Minute Moving Averages Plotted on Expanded Scale.

then estimated from the permeability and the above equation for comparison with the heat flux data from the quench experiments.

Both the permeability and dryout heat flux are expected to increase with decreasing melt concrete content. In Figure 2-11, the dryout heat flux is plotted using the saturated water and steam properties at the test pressure. The data is in general agreement with the expected trend.

The permeability tests provide a single, objective measurement of dryout heat flux for each ingot, in contrast to the somewhat subjective identification of a plateau in the quench test heat flux plots. Ideally, these are independent measurements of the same corium characteristic. Both data sets are combined in Figure 2-12 to check agreement between the different types of measurements. Heat fluxes derived from the permeability data are shown as short dashed lines

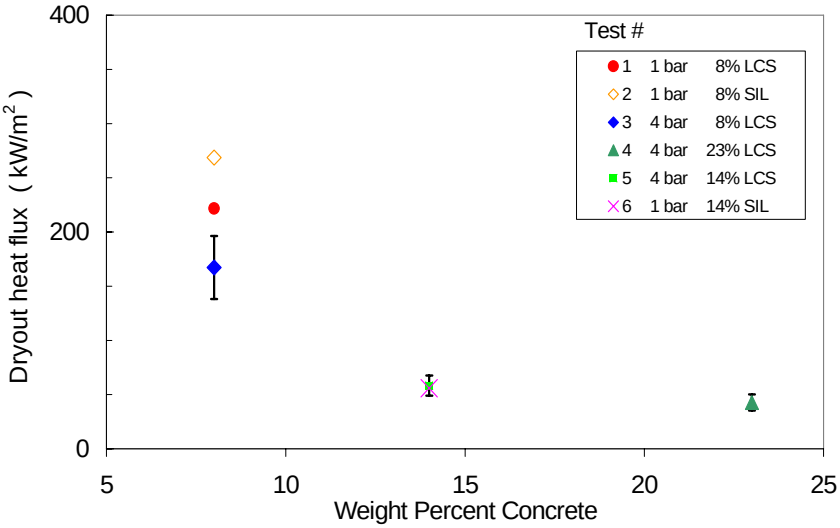

Figure 2-11. Dryout Heat Flux as Determined by Permeability Measurements.

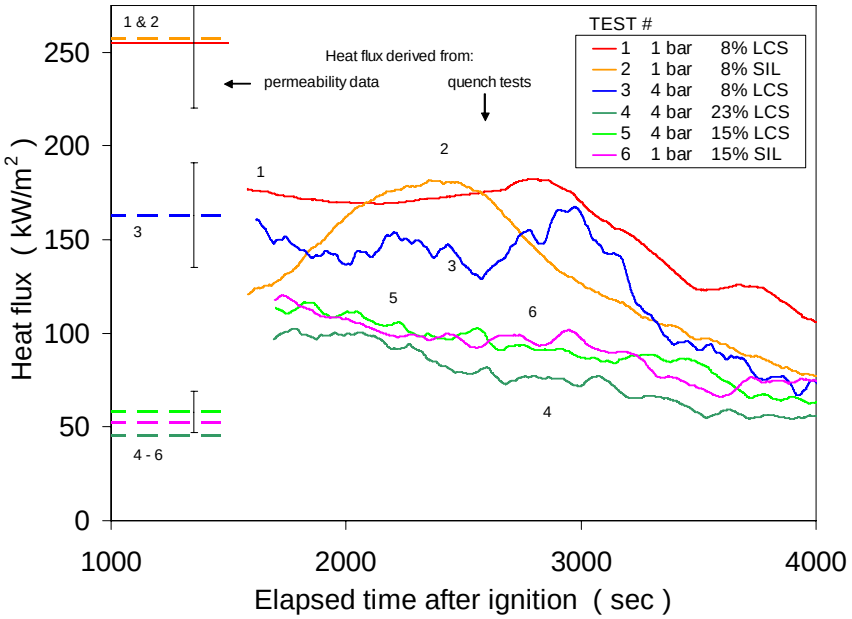

Figure 2-12. Comparison Between Dryout Heat Fluxes as Determined by Permeability Measurements and Heat Flux Measured During Quench Tests.

along the left side of the graph. Quench test data is shown from 1500 s onwards, which is the approximate time in each test when steam production had fully recovered from coolant injection and structure heating. Test 7 is not included since no permeability data was obtained for that test. The crack structure of the ingot was so extensive that it broke apart during removal from the RV.

Only Test 1 exhibits an unambiguous plateau, but Figure 2-12 shows that the trend in the permeability-derived dryout heat flux matches that of the quench tests. A ranking of the average heat flux during the first ~½ hour after steam recovery would match that of the dryout heat flux data. The three tests with the highest concrete content generated the lowest steaming rate during this ½ hour, and also produced the corium samples with the lowest permeability. Tests 1 and 2, in contrast, are associated with the highest steaming rates and permeabilities. It is recognized that the magnitude of each permeability-based dryout heat flux does not match up well with the corresponding plateau or early-phase average. Such a match cannot be expected because a) Eq. 2-3 was developed for an idealized particle bed whereas a corium ingot is a solid mass with cracks, and b) the cooling corium can never be in overall thermal equilibrium and is unlikely to support a constant surface heat flux for very long; lateral heat losses to the crucible also contribute to a natural decline in the heat flux that can obscure a dryout limit-generated plateau. Still, the agreement in the heat flux trends is a positive sign that the measurement methodology is appropriate and the characterization of uncertainties reasonable. More important, the data clearly identifies a trend towards decreasing heat flux with increasing concrete content, and indicates a maximum dryout heat flux in the range of ~100 to ~300 kW/m^2 for corium containing 4-23% siliceous or limestone/common sand concrete.

2.3 Data Compared With Predictions of a General Water Ingression Model

The trends in the quench test data largely follow those predicted by the Jones model.[21] However, validation of that model is not the principal role for the data. The model is of limited use for general predictions because it includes the crust permeability, which varies with melt composition and must be determined empirically. Given the wide range of potential corium compositions that can develop during a severe accident, a model without composition-dependent empirical factors is of more general use. Such a model, based on the work of Lister,[22] has been developed by Epstein. [23] The main purpose of the SSWICS experiments is to produce data to verify the Lister/Epstein dryout heat flux model. A brief outline of the model is included below. Additional details are provided elsewhere.[10,24]

Lister's study considered the mechanism by which hot rock is cooled by water percolating down into cracks and fissures. The central idea is that thermal stresses are generated in rock as it cools, which can result in cracking and the production of pathways for water penetration. The water penetration enhances cooling, which promotes further cracking and can produce a self-propagating crack front traveling downward through the rock. The appeal of the model is that it predicts a maximum cooling rate (our dryout heat flux) using only the thermal and mechanical properties of the rock, the coolant properties, and a single empirical constant. Epstein's contribution was to adapt the model for the case of corium quenching. He developed an expression that includes the effect of convective heat transfer from the melt to the underside of the crust. For the SSWICS experiments, convective heat transfer is small compared to the heat flux through the crust because there is no gas-induced agitation to enhance heat transfer (recall that an inert basemat was used for each test). For this special case, Epstein's expression

for the dryout heat flux can be reduced to an expression containing thermophysical and bulk properties of the corium and steam, and a single empirical constant: [10]

$$q''_{dry} = C\left(\frac{h_{lv}(\rho_l - \rho_v)g}{\nu_v}\right)^{5/13}\left(\frac{Nk_{cr}^2(\Delta e_{sat})^2}{c_{cr}\Delta e_{cr}}\right)^{4/13}\left(\alpha_{\exp}\left[T_{sol} - \left(T_{sat} + \frac{\sigma_{tensile}}{\alpha_{\exp}E_{cr}}\right)\right]\right)^{15/13} \quad (2\text{-}4)$$

where:

C	=	empirical constant to be adjusted according to experiment,
Δe_{sat}	=	corium specific enthalpy change upon quench from the freezing temperature to water saturation temperature,
Δe_{cr}	=	corium specific enthalpy change upon cooldown from the freezing temperature to the cracking temperature.
c_{cr}	=	crust specific heat,
E_{cr}	=	crust elastic modulus,
k_{cr}	=	crust thermal conductivity,
N	=	numerical constant = 0.1 K-m$^{1/2}$,
T_{sol}	=	crust solidus temperature,
T_{sat}	=	coolant boiling temperature,
α_{exp}	=	corium linear expansion coefficient,
$\sigma_{tensile}$	=	crust tensile strength,
ν_v	=	kinematic viscosity.

One of the key simplifications made as part of this work in arriving at Eq. 2-4 is the definition of a temperature at which a cooling mass of solidified corium cracks. In general, it could be expected to develop cracks at some point after thermal stresses exceed the material tensile strength. As a first approximation, we have assumed that cracking occurs when thermal stresses reach the tensile stress. The model also requires specification of the corium freezing temperature. Definition of the freezing temperature is not as straightforward for corium as for conventional materials since it transforms from a liquid to a solid over a wide temperature range. Figure 2-13 shows calculated corium liquidus and solid temperatures, which vary with the amount of concrete but are largely independent of concrete type. This simple curve fit is based on the experimental data obtained by Roche.[25] Equation 2-4 was obtained by equating the freezing temperature of corium with the solidus temperature.

The dryout heat flux predicted by Eq. 2-4 is plotted in Figure 2-14 for corium with either siliceous or LCS concrete. For both types of corium, the heat flux decreases with increasing concrete content. There is a particularly rapid drop for mixtures of less than 15% concrete and the shape of the curves matches that of the solidus curve.

The dryout heat fluxes derived from the quench test data are plotted in Figure 2-14. Each data point represents a 200 s average centered on 1500 s, which reduces the effects of short term fluctuations. Close inspection of Figures 2-9 or 2-10 reveals that the data could be evaluated anywhere between 1500 and 2000 s without substantially altering the results. The error bars shown in the figure represent an uncertainty estimate of 17 kW based on the maximum drift in the ΔP sensor over an interval of 200 s.

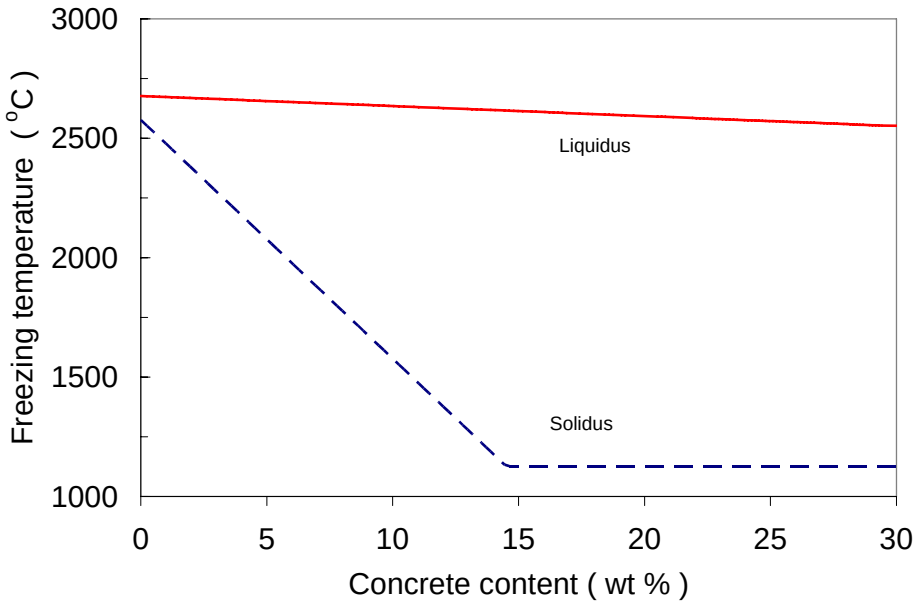

Figure 2-13. Oxide Solidus and Liquidus Temperatures; Fitted Curves to Data Obtained by Roche.[25]

The heat flux predictions of the Lister/Epstein model were generated by adjusting the empirical constant *C* to produce the overall best fit to the test data. The resulting value of *C* is 5.5. As part of this assessment, the crust mechanical property data in Eq. 2-4 were approximated using a volume-weighted method based on the properties of the individual corium constituents; see Reference 24 for details. The most striking feature of Figure 2-14 is the similarity in the model and data trends of heat flux versus concrete content. Though only seven tests were performed, the data appears to support the model's prediction of a rapid rise in dryout heat flux for concrete contents less than ~15%. For corium with greater amounts of concrete, the dryout heat flux is relatively low and nearly independent of concrete content, i.e., water ingression enhanced cooling is not very effective and the corium is cooled almost entirely by conduction.

The curve fit used in Figure 2-14 for the 4 bar data provides a suitable fit also for the 1 bar data, highlighting the finding that the test data does not exhibit the expected pressure dependence. Jones' model predicts a twofold heat flux increase between 1 and 4 bar. The Lister/Epstein model also predicts an increase, but it is in the range of ~50% for LCS concrete. Despite these predictions, the data shows no distinct trend related to pressure. The data could be consistent with the pressure dependence predicted by the Lister/Epstein model for concrete contents >14%, but only because the variation with pressure is comparable to the measurement uncertainty of ±17 kW.

Figure 2-15 provides a second comparison between the Lister/Epstein model predictions and the SSWICS data. The three curves in the plot are the same as those in Figure 2-14 while the data points are the permeability-based measurements from Figure 2-11. It can be seen that the permeability data agrees reasonably well with the model predictions, which is expected since this data was shown to be in general agreement with the quench test data. More of note is the excellent match in the trend of heat flux versus concrete content. Like the quench test data, the permeability-based data follows the elbow-like curve with a significant rise in heat flux for

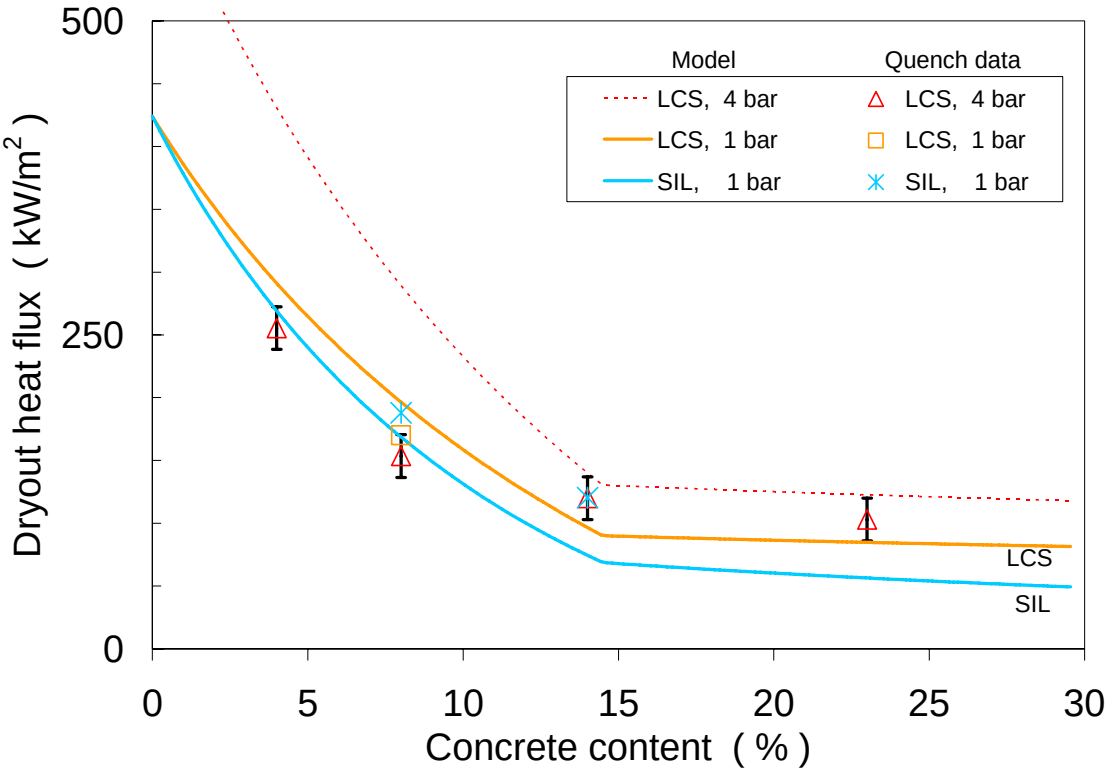

Figure 2-14. Dryout Heat Flux Predicted by Lister/Epstein Model vs. Corium Concrete Content.

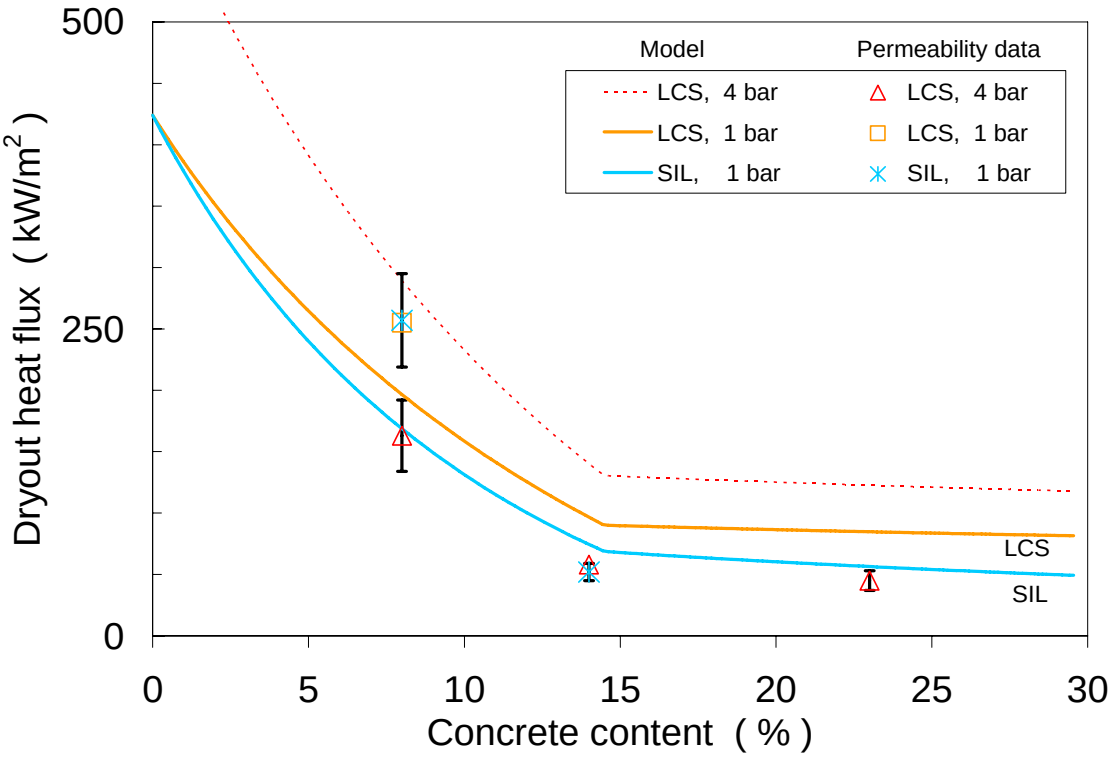

Figure 2-15. Lister/Epstein Model Compared to Permeability-Based Data.

corium with concrete contents <14%. The irregular shape of the Lister/Epstein heat flux curves is based on the particular properties of corium. The fact that both the quench test and permeability-based data mirror the curves lends credibility to the model and the assumptions upon which it is based.

2.4 Crust Strength Measurements

The objective of these tests was to provide data to validate the hypothesis that a plant-scale crust would be too weak to remain detached from, and suspended over, a corium pool. It is believed that a structurally weak crust would break under the combined load of its own weight and that of an overlying water layer, reestablishing contact with the corium beneath. The crust strength tests involved applying a mechanical load to the corium ingots produced by the quench tests to measure their mechanical strength. The strength was determined through a structural model that relates the load to the yield strength. The fracture stress of these ingots should be representative of material formed at plant scale because the ingots were of prototypic chemical composition and cooled by the quench mode expected for a plant accident.

The test rig used to apply static loads to the sectioned ingots is shown in Figure 2-16. It consisted of a heavy gauge steel frame on which a hydraulic press had been mounted and oriented to apply loads to the sample from above. A 35 mm-diameter piston transmitted the load to the sample surface while a load cell between the piston and hydraulic press measured the applied force. The corium sample was supported around the outer edge by a thin steel ring (30.2 cm O.D. and 7 mm thick wall) to approximate the simply-supported boundary condition used in the model to evaluate the sample strength. Displacement sensors monitored movement of the piston and the underside of the sample while the load was applied.

Before load testing, each ingot was sectioned to reduce its thickness so that the failure mode, tension along the centerline, duplicated that expected for the plant scale crust.[11] The ingots were cut with a band saw into disks ranging in thickness from 40 to 100 mm. The corium was cut while still within the MgO liner, which was retained for support during transport and load testing. Figure 2-17 shows a bottom view of the 90 mm section cut from the Test 3 ingot. The crack structure is typical of all ingots except that of Test 7, which was so fragmented that it broke apart before it could be load tested.

Figure 2-18 provides an example of the type of data collected for the strength tests. It shows the applied load and displacement measurements made in testing a 45 mm thick section cut from the Test 5 ingot. The load was applied in steps with short waiting periods between load increases. It can be seen that each increase produced detectable movement in both the piston and the displacement sensor beneath the sample. Also evident is a slight decline in the measured load immediately after each step increase. This relaxation phenomenon was observed in all of the strength tests. Sample failure was identified when an attempted load increase caused a relatively large jump in displacement and a reduction in the effective load. Failures were often accompanied by an audible cracking sound. The peak in the load curve was used to calculate the effective yield strength of the sample.

The stresses generated by the peak load were calculated with a simple analytical expression used for circular plates. For a concentrated axial load at the center of a simply supported circular plate under the conditions in which $D/t \geq 4$, the maximum tensile stress develops at the centerline of the plate and is given by the following equation:[26]

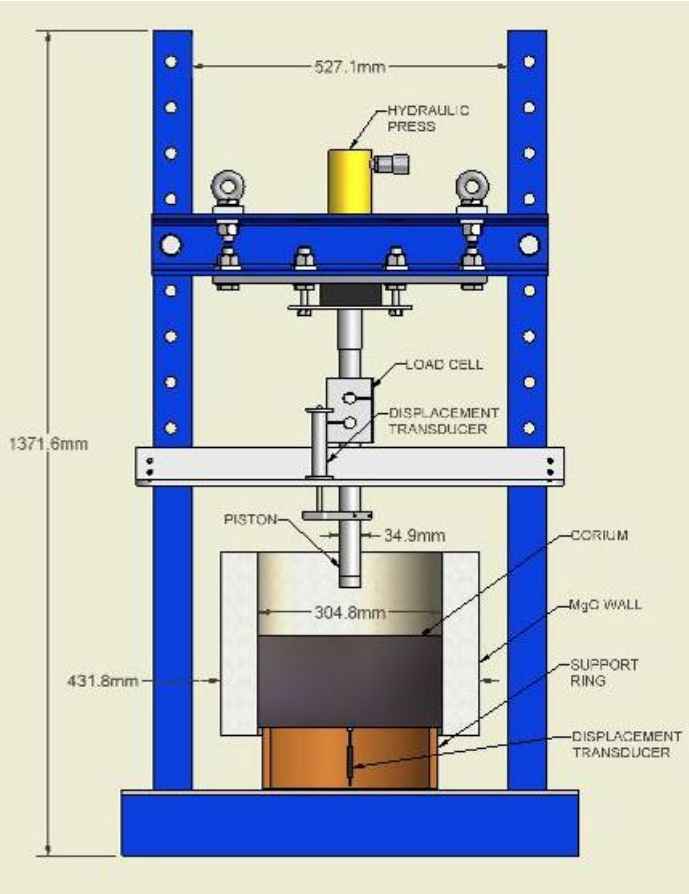

Figure 2-16. Crust Loading Apparatus.

Figure 2-17. Bottom View of Sectioned Ingot Produced in Test 3.

$$\sigma_{\max} = \frac{3P}{2\pi t^2}\left[(1+\nu)\ln\left(\frac{R}{r_o'}\right)+1\right] \tag{2-5}$$

where σ_{max} = maximum stress in plate, P = applied load, t = crust thickness, R = plate radius, ν = Poisson's ratio, and r'_o is the effective radius of the circular column that is in contact with, and applying the load to, the crust. This parameter is related to actual column radius and the crust thickness through the equation:

$$r_o' = \sqrt{1.6\,r_o^2 + t^2} - 0.675t \tag{2-6}$$

Figure 2-19 shows the maximum centerline stresses generated within each test specimen. The stresses were calculated with the peak recorded load, a piston radius of 17.5 mm, and the sample dimensions listed in Table 2-2. Poisson's ratio was assumed to be 0.3, the approximate value for the main crust constituent, UO_2. Stresses were plotted versus concrete content to show the relationship between crust strength and the amount of concrete. Chemical analyses indicated that the distribution of chemical constituents within each ingot was generally homogenous. Thus the concrete content of each sample is near the average concrete content defined in the thermite formulation (Table 2-2). Reference 11 contains detailed results from the chemical analyses showing the distributions of chemical constituents within each ingot.

There is no readily apparent data trend in Figure 2-19 and most of the strength measurements fall in the range of 1-3 MPa. The error bars shown in the plot are based on uncertainty in segment thickness, which is roughly ± 5 mm and considered to be the largest quantifiable source of uncertainty in the strength measurements.

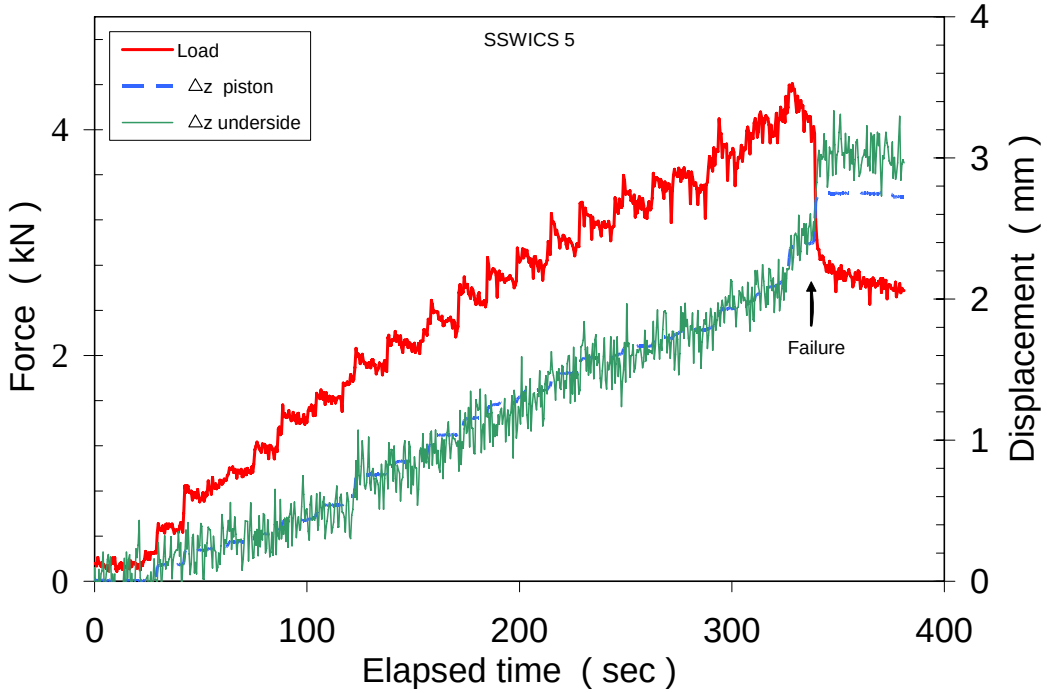

Figure 2-18. Test 5 Sample; 45 mm Thick Segment from Bottom of the Ingot.

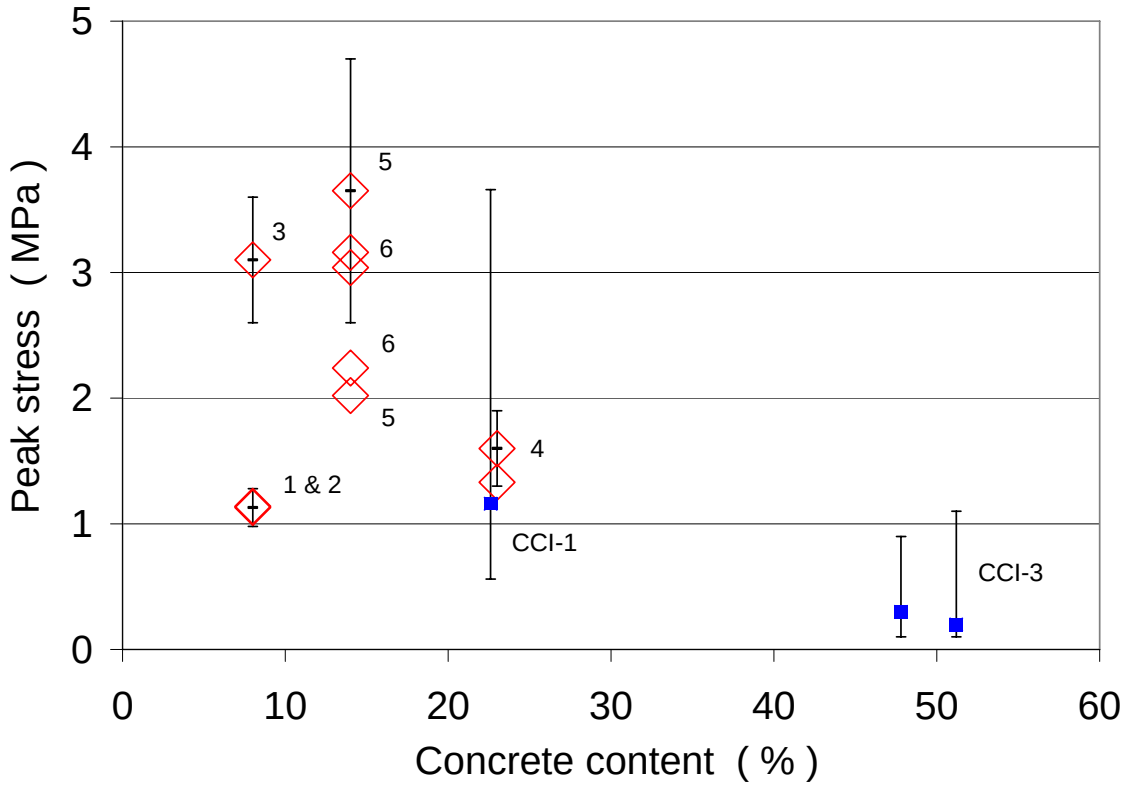

Figure 2-19. Peak Centerline Stress vs. Sample Concrete Content. CCI Data: In-Situ Measurements at High Temperature During Core-Concrete Interaction.

Also included in Figure 2-19 are in-situ measurements of crust strength made during large-scale corium/concrete interaction tests CCI-1 and CCI-3, which are described later in this report. These measurements of the crust strength were made under prototypic temperature conditions and before cool down. The crusts were in the range of 50-70 mm thick with molten corium underneath and a layer of water on top. The strength determinations were made by measuring the force required to break the crusts with a steel lance. The data are useful because they provide an opportunity to compare the mechanical strength determined at room temperature with measurements made on crusts under actual accident conditions. There are large uncertainty ranges associated with the data, which is based on uncertainties in the crust thicknesses at the time they were broken. Nonetheless, it is evident from the plot that the room temperature measurements compare very favorably with the high temperature CCI data.

Figure 2-20 combines the stress data with the calculated tensile strength for corium containing either LCS concrete or siliceous concrete.[24] It is clear from the plot that, independent of composition, the measured crust strength is far below the estimated value for solid corium. This indicates that the crack structure, not the composition, is the main determinant of crust sample strength.

The load-tested segments ranged in size from 40 to 100 mm, which corresponds to aspect ratios from 7.5 to 3. Since the target minimum aspect ratio is 4, it is of interest to see if the data exhibits any dependency upon sample thickness, which might indicate flawed measurements, particularly for the thickest segments. The data have been plotted in Figure 2-21 (note that there are two data points at 100 mm; the data for Tests 1 and 2 are nearly identical and appear as one point on the plot). It is reassuring that the figure shows no correlation between segment

Table 2-2 Summary of Crust Strength Tests.

Parameter	Test Number									
	1	2	3	4		5			6	
Melt composition (wt % UO_2/ZrO_2/Cr/concrete)	61/25/6/8	61/25/6/8	61/25/6/8	48/20/9/23		56/23/7/14			56/23/6/14	
Slab depth (mm) ($\sigma \sim \pm 5$ mm)	100	100	90	55-60	55-60	55	45	50	55	40
Region of ingot*	T	T	T	M	B	M	B	T	M	B
Concrete content (%)	8	8	8	23	23	14	14	14	14	14
Peak load (kN)	8.2	8.2	15.3	3.2	2.7	3.6	4.4	4.5	4.1	3.0
Estimated stress for peak load (MPa)	1.1	1.1	2.7	1.6	1.3	2.0	3.6	3.0	2.2	3.2
Stress uncertainty (MPa)	0.2	0.2	0.4	0.3	0.3	1.0	0.8	1.0	0.5	0.7
Total piston displacement at peak load (mm)	10.0	9.1	8.2	2.4	5.3	2.3	2.4	5.0	3.8	4.8
Bottom surface displacement at peak load (mm)	N.A.**	N.A.	N.A.	N.A	N.A.	2.1	2.2	8.9	3.2	3.8

***T = top; M = middle; B = bottom segment. **N.A. = not applicable**

thickness and measured strength, which is in accordance with the results expected under ideal conditions. Also included in the figure is the calculated peak centerline stress of a plant-scale crust having a diameter of 6 m and density of 7000 kg/m^3. The crust is presumed to be anchored at the perimeter and subjected to a distributed load equal to the weight of the crust itself. The plot is useful in illustrating that if such a crust has a mechanical strength similar to that of the SSWICS sections, it must be at least 200-300 mm thick to be self-supporting. The crust must be even thicker, of course, if an overlying water layer or a particle bed must also be supported. The results of the strength tests indicate that the crack structure within the corium ingots greatly reduces mechanical strength. The data clearly demonstrates that an actual plant-scale crust would be far weaker than an equivalent corium plate free of defects. Moreover, extrapolation of the data indicates that a plant-scale crust would not be mechanically stable. Rather, it will most likely fail and reestablish contact with the melt. Therefore, for plant accident conditions, the continued contact between the melt and crust will allow water ingression and melt eruption cooling mechanisms to proceed and contribute to termination of the core-concrete interaction.

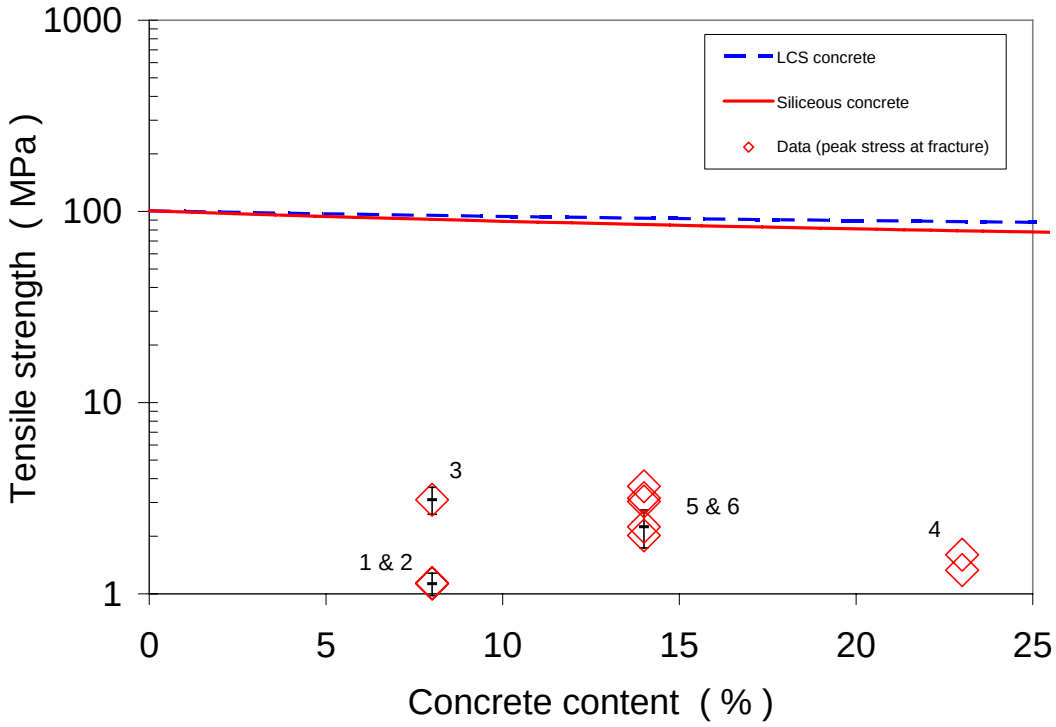

Figure 2-20. Peak Centerline Stresses Compared to the Calculated Tensile Strength of Two Types of Corium/Concrete Mixtures.[24]

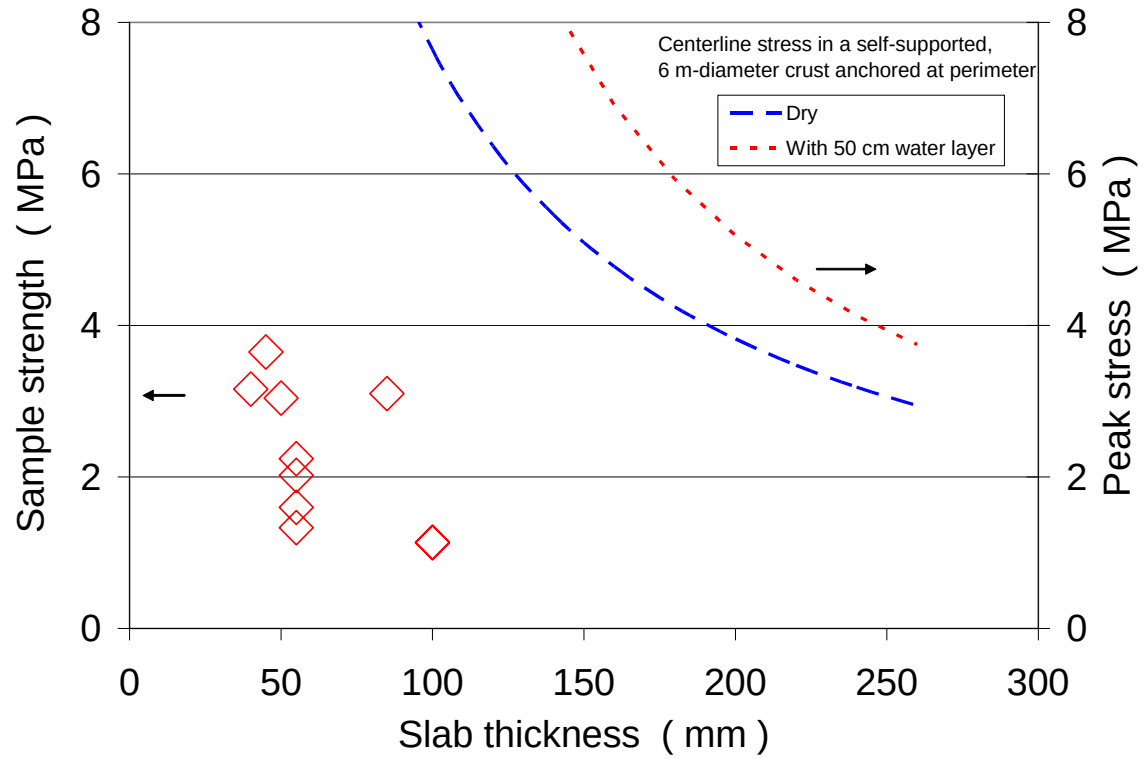

Figure 2-21. Comparison of Measured Strength of SSWICS Corium Segments with the Peak Centerline Stress in a Plant-Scale Crust.

3.0 CCI TEST SERIES RESULTS

The Core-Concrete Interaction (CCI) experiments were integral-type tests that were intended to provide information in several areas, including: i) lateral vs. axial power split during dry core-concrete interaction, ii) integral debris coolability data following late phase flooding, and iii) data regarding the nature and extent of the cooling transient following breach of the crust formed at the melt-water interface. The experimental approach was to investigate the interaction of Pressurized Water Reactor (PWR) core melts with specially designed 2-D concrete test sections. The initial phase of the tests was conducted under dry cavity conditions. After a predetermined time interval and/or ablation depth was reached, the cavities were flooded with water to obtain data on the coolability of core melts after the interaction had progressed for some time. The initial melt compositions were predominately oxidic. A significant metal phase was not involved, but may be present during an accident. Based on the initial melt density of ~6500 kg/m^3, the steel may be layered below the oxide phase. Thus, data from these tests may not be directly applicable to reactor accident sequences, but the results are nonetheless useful for code validation purposes. The input power levels of 120-150 kW used in the tests were selected so that the heat fluxes from the melt to concrete surfaces and the upper atmosphere were initially in the range of that expected early in the accident sequence (i.e., 150-200 kW/m^2).

Three successful experiments were conducted as part of the test series; specifications for the individual experiments are provided in Table 3-1. Additional details regarding these tests are provided in the summary report for this test series.[15]

The CCI test facility consisted of a test apparatus, a power supply for Direct Electrical Heating (DEH) of the corium, a water supply system, two steam condensation (quench) tanks, a ventilation system to filter and exhaust the reaction product gases, and a data acquisition system. Key facility features are illustrated in Figure 3-1.

3.1 Test Apparatus

The apparatus for containment of the core material consisted of a test section that was 3.4 tall with a square internal cross-section measuring 50 x 50 cm. The concrete crucibles were located at the bottom of the test section. A top view of the lower test section is shown in Figure 3-2, while a cross-sectional view showing the concrete sidewalls and basemat is provided in Figure 3-3. As shown in the figures, the concrete basemat had an initial cross-sectional area of 50 x 50 cm, and both the basemat and sidewalls were 55 cm deep. This design could accommodate up to 35 cm of radial and/or axial ablation.

The concrete and MgO sidewalls were contained within a flanged steel form that secured the lower section to the remaining test section components via an aluminum transition plate. The lower section was fabricated with vertical, flanged casting seams between the MgO and concrete so that the sidewalls could be removed after the test to expose the solidified corium for further examination. A layer of crushed UO_2 pellets was used to protect the interior surface of each MgO sidewall against thermo-chemical attack by the corium. Tungsten back-up plates were embedded in the sidewalls to act as a final barrier to terminate sidewall attack in the event that the UO_2 layer did not provide adequate protection.

Melt generation was achieved through an exothermic chemical reaction yielding the target initial melt mass over a timescale of ~ 30 seconds. After the reaction, DEH was supplied to the melt to simulate decay heat through two banks of 9.5 cm diameter tungsten electrodes that

Table 3-1. Specifications for CCI Tests.

Parameter	Specification for Test:		
	CCI-1	**CCI-2**	**CCI-3**
Corium	PWR + 8 wt% SIL	PWR + 8 wt% LCS	PWR + 15 wt% SIL
Concrete type[a]	SIL (US-type)	LCS	SIL (EU-type)
Basemat cross-section	50 cm x 50 cm	50 cm x 50 cm	50 cm x 50 cm
Initial melt mass (depth)	400 kg (25 cm)	400 kg (25 cm)	375 kg (25 cm)
Test section sidewall construction	Nonelectrode walls: concrete Electrode walls: Inert	Nonelectrode walls: concrete Electrode walls: Inert	Nonelectrode walls: concrete Electrode walls: Inert
Lateral/Axial ablation limit	35/35 cm	35/35 cm	35/35 cm
System pressure	Atmospheric	Atmospheric	Atmospheric
Melt formation tech.	Chemical reaction (~30 s)	Chemical reaction (~30 s)	Chemical reaction (~30 s)
Initial melt temperature	1950 ºC	1880 ºC	1950 ºC
Melt heating technique	DEH	DEH	DEH
Power supply operation prior to water addition	Constant @ 150 kW	Constant @ 120 kW	Constant @ 120 kW
Criteria for water addition	1) 5.5 hours of operation with DEH input, or 2) lateral/axial ablation reaches 30 cm	1) 5.5 hours of operation with DEH input, or 2) lateral/axial ablation reaches 30 cm	1) 5.5 hours of operation with DEH input, or 2) lateral/axial ablation reaches 30 cm
Inlet water flowrate/temp.	2 lps/20 ºC	2 lps/20 ºC	2 lps/20 ºC
Water depth over melt	50 ± 5 cm	50 ± 5 cm	50 ± 5 cm
Power supply operation after water addition	Constant voltage	Constant voltage	Constant voltage
Test termination criteria	1) Melt temperature falls below concrete solidus, 2) ablation is arrested, or 3) 35 cm ablation limit is reached.	1) Melt temperature falls below concrete solidus, 2) ablation is arrested, or 3) 35 cm ablation limit is reached.	1) Melt temperature falls below concrete solidus, 2) ablation is arrested, or 3) 35 cm ablation limit is reached.
Operational Summary	Successful: non-symmetrical ablation behavior	Successful: symmetrical ablation behavior	Successful: symmetrical ablation behavior

[a]SIL denotes siliceous concrete, LCS denotes Limestone/Common Sand concrete.

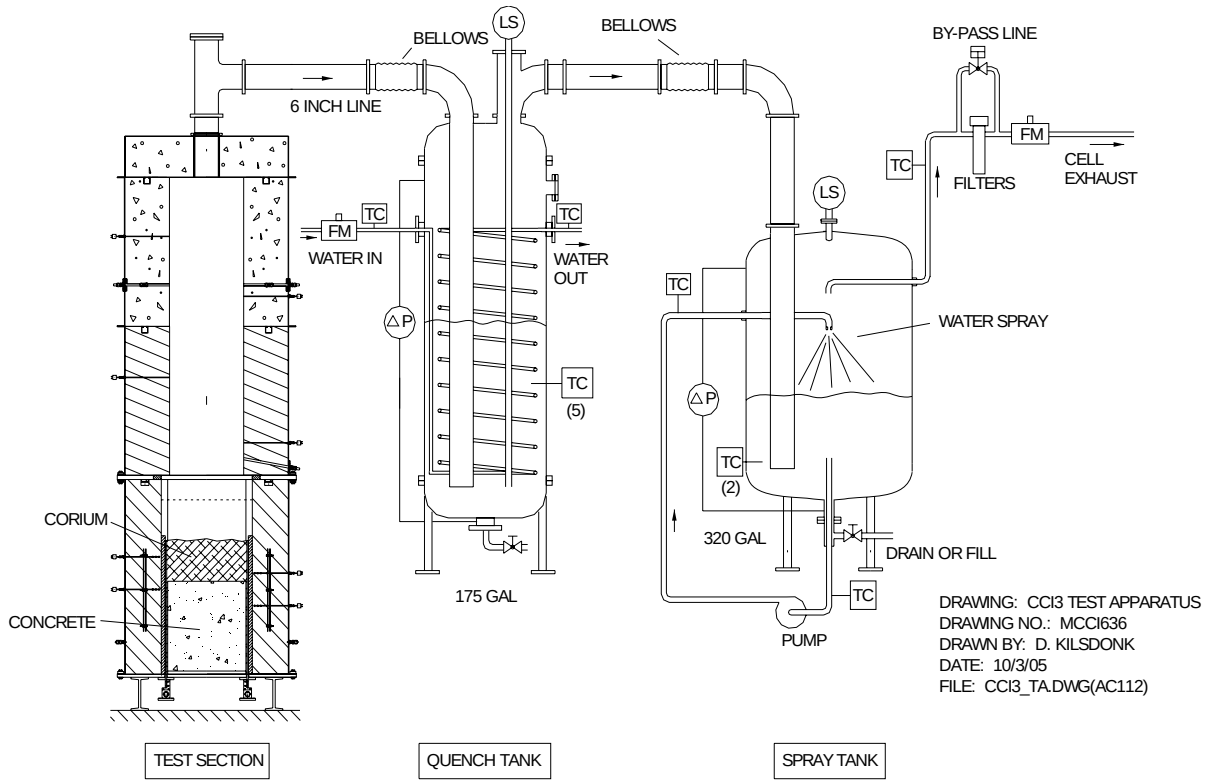

Figure 3-1. Key Elements of the CCI Test Apparatus.

were positioned with a pitch of 1.9 cm. As shown in Figures 3-2 and 3-3, the electrodes lined the interior surfaces of the two opposing MgO sidewalls. They were attached by copper clamps and water-cooled bus bars to a 560 kW AC power supply. As shown in Figure 3-2, the electrodes extended 120 cm across each sidewall. At the start of the experiment, the electrical current was drawn through the center 50 cm lateral span of electrodes that were in direct contact with the melt. As the test progressed and the concrete sidewalls were eroded, additional electrodes were exposed to corium. Current was drawn through the newly exposed heating elements, thereby maintaining a uniform internal heating pattern in the melt over the course of the experiment. Given the overall electrode span of 120 cm, up to 35 cm of radial sidewall ablation could be accommodated while maintaining uniform heat input.

As shown in Figure 3-1, a large (15 cm diameter) gas line was used to vent the helium cover gas and the various gas species arising from the core-concrete interaction (i.e., CO, CO_2, H_2O, and H_2) into two adjacent tanks that were partially filled with water. In the initial phase of the experiment, while the cavity remained dry, the tanks served to cool the reaction product gases and filter aerosols generated from the core-concrete interaction. In the late phase, after the cavity was flooded, the tanks served to condense the steam and, based on the measured condensation rate, provide data on the corium cooling rate. In either case, the helium cover gas and noncondensables (CO, CO_2, and H_2) passed through the tanks and were vented through an off-gas system that included a demister, filters, and a gas flow meter. The gases were exhausted through the containment ventilation system and a series of high efficiency filters before finally being released from the building stack.

After a specified period of core-concrete interaction, the cavity was flooded using an instrumented water supply system. The water entered the test section through two weirs located in the opposing (non-electrode) sidewalls of the top test section. After initial water addition, the water level over the corium was kept roughly in the range of 50 ± 5 cm by periodically adding makeup. Once a stable crust formed at the melt-water interface, an insertable lance was used in an attempt to break the crust to obtain data on the nature and extent of debris cooling that occurs following transient crust breach. As described in Section 1.0, this is a cooling mechanism that is expected to be active at plant scale owing to the mechanical instability of crusts that would form in the typical 5-6 m cavity span of most plants. The lance was simply a 2.54 cm diameter, 304 stainless steel rod with a pointed tip. The lance was inserted through a seal in the lid of the test section. The driving force for the lance was a 450 kg dead weight that was remotely lowered with the cell crane during the test.

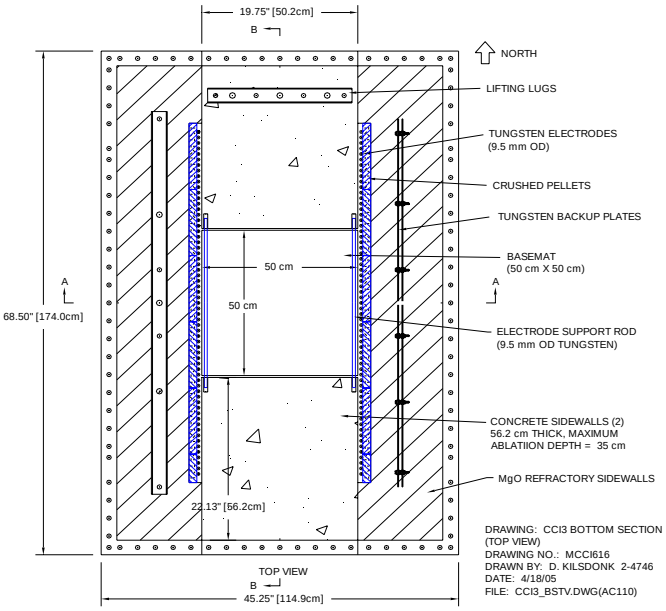

Figure 3-2. Top View of Lower Test Section.

3.2 Instrumentation

The CCI facility was instrumented to monitor and guide experimental operation and to log data for subsequent evaluation. Principal parameters monitored during the course of the test included the power supply voltage, current, and gross input power to the melt; melt temperature and temperatures within the concrete basemat and sidewalls; crust lance position and applied load; supply water flow rate; water volume and temperature within the test apparatus, and water volume and temperature within the quench system tanks. Other key data recorded by the DAS included temperatures within test section structural sidewalls, off gas temperature and flow rate, and pressures at various locations within the system.

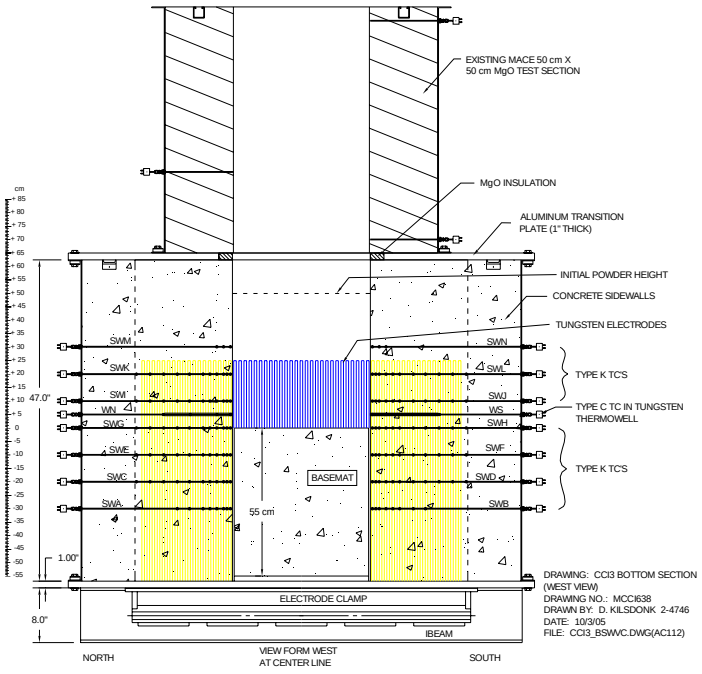

Figure 3-3. Side View of Lower Test Section.

The concrete sidewall instrumentation locations are shown in Figure 3-3, while a plan view of the basemat thermocouple layout is provided in Figure 3-4. Both the basemat and sidewalls were instrumented with multi-junction, Type K thermocouple assemblies to determine the 2-D ablation profile as a function of time. In addition, seven Type C thermocouple assemblies that were protected by tungsten thermowells were mounted vertically within the basemat and horizontally through the concrete sidewalls. The purpose of these instruments was to provide data on the axial and lateral melt temperature distributions versus time. Other significant test instrumentation included a stationary (lid mounted) video camera for observing physical characteristics of the core-concrete interaction.

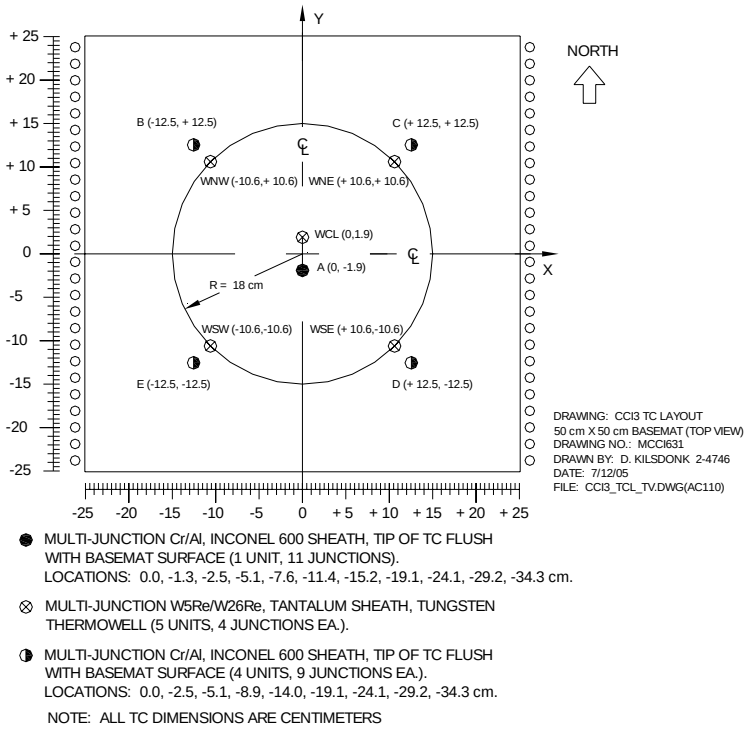

Figure 3-4. Plan View of Basemat Instrumentation.

3.3 Corium and Concrete Compositions

As shown in Table 3-1, concrete type was the key parametric variation among the three tests conducted as part of the experimental series. Both tests CCI-1 and CCI-3 were conducted with siliceous concrete, but the raw materials were from different geographic origins, while test CCI-2 was conducted with LCS concrete. The chemical compositions of the three concrete types are shown in Table 3-2. The compositions were determined through chemical analysis of samples taken from concrete archives that were produced while fabricating the basemat and sidewall components for each test.

Table 3-2. Chemical Composition of CCI Concretes.

Oxide	CCI-1 Wt%	CCI-2 Wt%	CCI-3 Wt%
Al_2O_3	0.77	2.49	3.53
CaO	8.54	25.88	16.79
Fe_2O_3	0.79	1.39	1.49
MgO	0.60	11.47	0.85
MnO	0.00	0.03	0.04
K_20	0.12	0.55	0.81
SiO_2	82.48	21.61	59.91
Na_2O	0.00	0.31	0.66
SrO	0.00	0.00	0.04
TiO_2	0.051	0.135	0.155
SO_3	0.514	0.505	0.434
CO_2	0.901	29.71	9.80
H_2O, Free	1.808	3.255	2.293
H_2O, Bound	1.92	1.11	1.40
Total	98.48	98.47	98.19

As shown in Table 3-1, the initial corium compositions were typical of a fully oxidized PWR core melt containing various proportions of calcined concrete as an initial constituent. The compositions of the concrete additives were consistent with the type of concrete used for the sidewalls and basemat for each test. Aside from lowering the melting point of the mixtures,[25] the additives were incorporated to account for concrete erosion that is expected to occur during the corium spreading phase following breach of the Reactor Pressure Vessel (RPV).[27]

Table 3-3. Initial Melt Compositions for CCI Test Series.

Constituent	CCI-1 (Wt%)	CCI-2 (Wt%)	CCI-3 (Wt%)
UO_2	60.97	60.62	56.32
ZrO_2	25.04	24.90	23.13
Calcined Concrete	8.08[a]	8.07[b]	14.14[a]
Cr	5.91	6.41	6.41

[a]Calcined siliceous concrete: 79.0/0.9/15.6/4.5 wt% SiO_2/MgO/CaO/Al_2O
[b]Calcined LCS concrete: 42.0/14.1/38.8/5.1 wt% SiO_2/MgO/CaO/Al_2O_3

Table 3-4. Detailed Thermite Compositions for CCI Tests.

Const.	CCI-1		CCI-2		CCI-3	
	Wt%	Mass (kg)	Wt %	Mass (kg)	Wt %	Mass (kg)
UO_2	60.97	243.88	60.62	242.48	56.32	211.41
ZrO_2	25.04	100.16	24.90	99.60	23.13	86.82
SiO_2	6.38	25.52	3.39	13.56	11.17	41.92
MgO	0.07	0.28	1.14	4.56	0.12	0.45
Al_2O_3	0.38	1.52	0.41	1.64	0.64	2.40
CaO	1.25	5.00	3.13	12.52	2.21	8.31
Cr	5.91	23.64	6.41	25.64	6.41	24.06
Total	100.00	400.00	100.00	400.00	100.00	375.37

As part of the development work for the SSWICS test series,[10] specially designed exothermic chemical mixtures (or "thermites") were developed to produce the melt compositions shown in Table 3-1. The reader is referred to the individual data reports[10,15] for additional information regarding the detailed thermite compositions. The initial bulk melt compositions produced from these reactions are summarized in Table 3-3, while the detailed post-reaction compositions are provided in Table 3-4.

3.4 Results and Discussion

The key information obtained from the three tests included melt temperature, local concrete ablation rates, and debris/water heat flux after cavity flooding. A comparison of these measurements is provided in Figures 3-5 through 3-8, which provide the estimated average melt temperature, maximum lateral and axial concrete ablation rates, and debris/water heat flux plotted for each of the three tests. Time t=0 in these graphs corresponds to initial melt contact with the test section concrete basemats (i.e., completion of the thermite burn).

As shown in Figure 3-5, the initial melt temperature for the tests was in the range of range of 1880-1950 ºC. The differences were due to uncertainty/variability in the thermite reaction temperatures for the three different chemical mixtures used to generate the initial melt compositions. During dry cavity operations, all tests showed the overall trend of decreasing melt temperature as ablation progressed, which was due to a heat sink effect as relatively cool concrete slag was introduced into the melt, as well as the increasing heat transfer surface area as the melts expanded into the concrete crucibles. The decline in melt temperature may further

reflect the evolution of the pool boundary freezing temperature that decreased as additional concrete was eroded into the melt over the course of the tests.

Somewhat different behavior was noted for CCI-1, in which the melt temperature was relatively constant over the first ~40 minutes of the interaction. One possible contributor to this trend was the fact that this test was run at a 25 % higher power level in comparison to CCI-2 and CCI-3 (i.e. 150 kW vs. 120 kW; see Table 1-1). However, the lack of a temperature decline may have also been caused by crust formation at the core-concrete interfaces that acted to insulate the melt. Relatively low heat transfer rates to the concrete boundaries were evidenced by the low ablation rates exhibited over the first 40 minutes. However, once the surface crusts failed, ablation proceeded rapidly, and the CCI-1 melt temperature fell rapidly in comparison to the other tests. This initial stable crust behavior may have been linked to the exceptionally low gas content for this concrete type in comparison to others used in the test series (see Table 3-5). In particular, gas sparging at the core-concrete interface may provide the mechanical force required to dislodge the crust material from the interface, thereby allowing ablation to proceed. If this interpretation is correct, then the absence of significant gas sparging allowed the insulating crusts to remain stable over an extended period of time in Test CCI-1, which in turn caused the melt temperature to increase.

Aside from Test CCI-1, examination of Figures 3-5 through 3-7 indicates that Tests CCI-2 and CCI-3 also showed evidence of early crust formation phases that influenced the

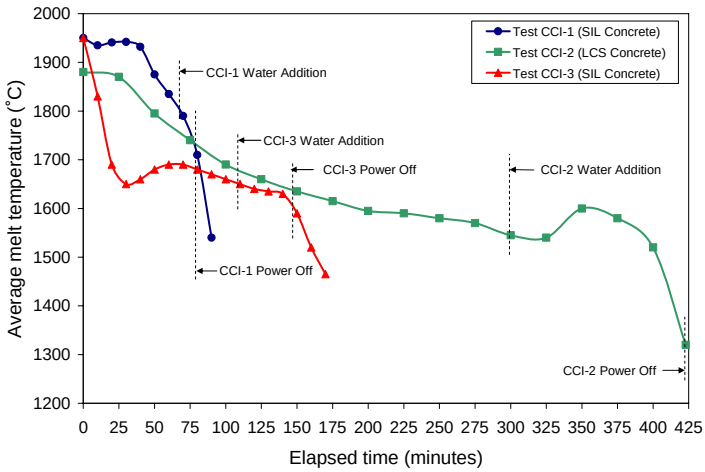

Figure 3-5. Average Melt Temperatures for CCI Tests.

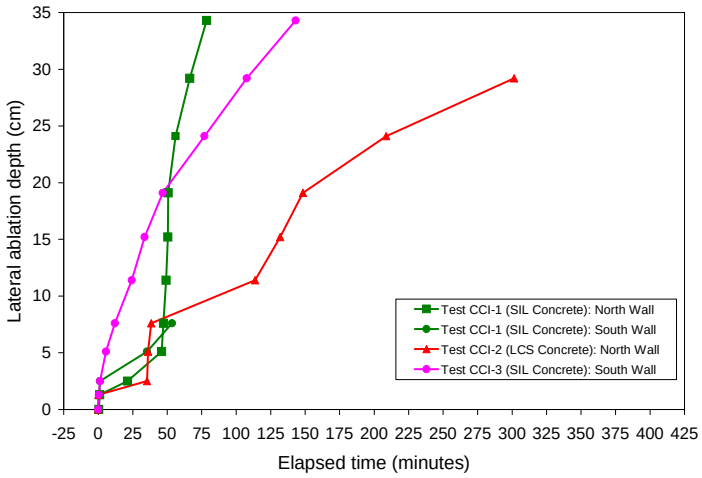

Figure 3-6. Lateral Ablation for CCI Tests.

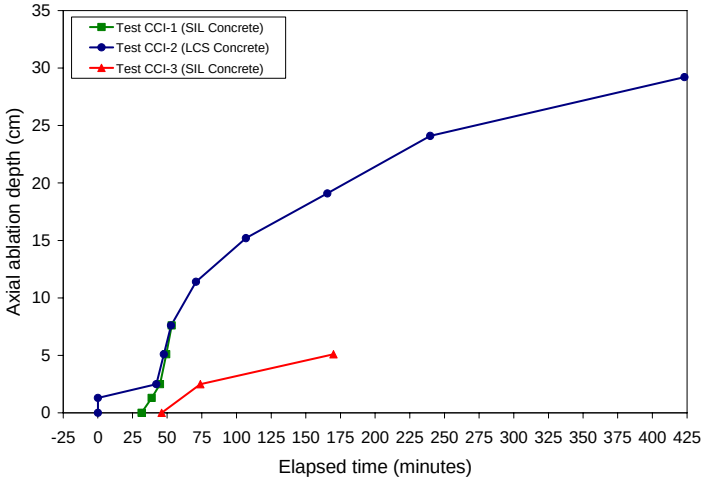

Figure 3-7. Axial Ablation for CCI Tests.

overall ablation behavior. For CCI-2, both axial and lateral ablation rates were quite low and the melt temperature relatively constant until ~ 30 minutes, after which time a period of rapid erosion occurred. However, unlike CCI-1, these erosion bursts were not sustained. Rather, after ~ 5 cm of ablation, both the axial and lateral ablation rates slowed significantly and approached a quasi-steady state. The reduced period of crust stability for CCI-2 is consistent with the idea that gas sparging can disrupt surface crusts, since the gas content of the CCI-2 concrete was significantly greater compared to CCI-1 (see Table 3-5).

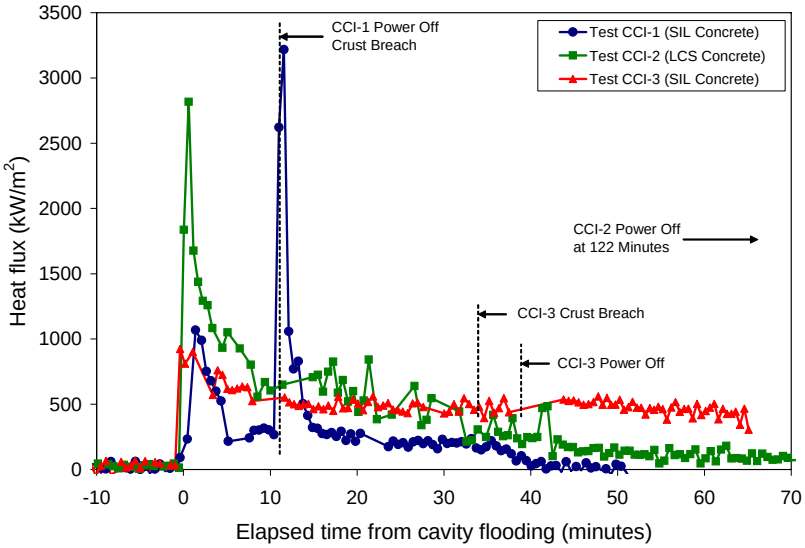

Figure 3-8. Debris/Water Heat Flux for CCI Tests.

Unlike tests CCI-1 and CCI-2, sidewall erosion in test CCI-3 commenced immediately upon contact with melt, and progressed steadily throughout the balance of the test. Conversely, the data suggests that the concrete basemat was protected by an insulating crust until ~ 50 minutes, at which point the crust failed and erosion commenced, albeit at a reduced rate relative to lateral ablation.

Aside from the initial cavity erosion behavior, examination of Figures 3-6 and 3-7 indicates that the long-term ablation process is influenced by concrete type. Estimates of average lateral and axial ablation rates for the three tests are provided in Table 3-6. To the extent possible, data points for these estimates were selected near the end of the dry cavity erosion phase for each test so that the erosion rate estimates are indicative of the long-term behavior. Assuming a quasi-steady erosion process, then the heat flux at the core-concrete interface is related to the ablation rate through the expression:

$$q_c'' = \rho_c h_{dc} \dot{\delta} c, \qquad (3\text{-}1)$$

Table 3-5. Properties of Concretes Used in CCI Test Series.

Concrete Property	Property for Test:		
	CCI-1	CCI-2	CCI-3
Type	SIL (US)	LCS	SIL (EU)
Liquidus Temperature[23] (ºC)	1250	1295	1250
Gas Content (wt %)	4.6	34.1	13.5
Decomposition Enthalpy (MJ/kg)[a]	1.60	2.27	1.72
Density (kg/m^3)	2300	2330	2270

[a]Evaluated at concrete liquidus temperature

Table 3-6. Lateral/Axial Ablation Rate and Power Split Estimates for CCI Tests.

Test	Concr. Type	Lateral Ablation		Axial Ablation		Lateral -Axial Heat Flux Ratio	Data Points Utilized for Ablation Rate Estimates
		Ablation Rate (cm/hr)	Heat Flux (kW/m^2)	Ablation Rate (cm/hr)	Heat Flux (kW/m^2)		
CCI-1	SIL (US)	N: 39.1	395	26.1	265	–[a]	N Lateral: (19.1 cm, 51 min) (29.2 cm, 66 min) S Lateral: (7.6 cm, 54 min) (5.1 cm, 35 min) Axial: (7.6 cm, 53 min) (1.3 cm, 39 min)
		S: 8.4	86				
CCI-2	LCS	4.0	58	4.0	59	1.0	Lateral: (19.1 cm, 148 min) (29.2 cm, 302 min) Axial: (15.2 cm, 107 min) (24.1 cm, 240 min)
CCI-3	SIL (EU)	10.0	97	2.5	25	4.0	Lateral: (19.1 cm, 47 min) (29.2 cm, 107 min) Axial: (2.5 cm, 117 min) (5.1 cm, 178 min)

[a]Heat flux ratio not evaluated for this test due to large asymmetry in lateral cavity erosion.

where ρ_c is the concrete density, h_{dc} is the concrete decomposition enthalpy, and $\dot{\delta}_c$ is the ablation rate. The property data required to evaluate the above expression is provided in Table 3-5; the corresponding heat flux estimates are provided in Table 3-6. As shown in the table, lateral and axial ablation rates for Test CCI-2, which was conducted with LCS concrete, were virtually indistinguishable; the concrete erosion rate averaged 4 cm/hr over several hours of interaction before gradually decreasing; the corresponding surface heat flux was ~ 60 kW/m^2. Thus, the lateral/axial heat flux ratio for this test was approximately unity.

The relatively uniform power split for CCI-2 can be contrasted with the results of the two tests conducted with siliceous concrete. For test CCI-1, the ablation was highly non-uniform, with most of the ablation concentrated in the North sidewall of the test apparatus. As described above, this test was conducted at a higher power density in comparison to CCI-2 and CCI-3. Moreover, the concrete for this test had exceptionally low gas content (see Table 3-5). Based on the discussion provided above, it thus appears that crust stability played a major role in determining the ablation progression for this experiment. In particular, the data suggests that after the insulating crust failed on the North concrete sidewall, the input power was dissipated predominately through ablation of this sidewall, while crusts continued to protect the basemat and south sidewall surfaces. As shown in Table 3-6, the ablation rate averaged 39 cm/hr in the North wall over the last 30 minutes of dry cavity operations; the average concrete surface heat flux was ~ 395 kW/m^2. Conversely, brief ablation bursts that reached 8.4 cm/hr in the South wall and 26 cm/hr axially occurred early in the experimental sequence, but the data suggests that crusts subsequently reformed on these surfaces, resulting in very little ablation over the balance of test operations. Based on these transient effects, a power split estimate was not formulated for this test, since the estimate would be highly speculative.

In contrast to Test CCI-1, the second test conducted with siliceous concrete (CCI-3) exhibited fairly symmetrical ablation insofar as the progression of the ablation fronts into the two opposing sidewalls of the apparatus is concerned. However, unlike Test CCI-1, the lateral

ablation was highly pronounced in comparison to axial for this particular test. In this regard, the results of tests CCI-1 and CCI-3 are consistent. As shown in Table 3-6, lateral ablation averaged 10 cm/hr over the last hour of the experiment, while the axial ablation rate was limited to 2.5 cm/hr over the same timeframe. The corresponding heat fluxes in the lateral and axial directions were 97 and 25 kW/m^2, respectively. On this basis, the lateral/axial surface heat flux ratio for test CCI-3 was estimated as ~ 4, which is significantly higher than the near-unity ratio deduced for test CCI-2 with LCS concrete. Thus, this data clearly indicates that there is a strong effect of concrete type on the spatial heat flux distribution at the core-concrete interface during dry core-concrete interaction. Between these two concrete types, possible explanations for differences in the erosion behavior are chemical composition (LCS concrete has a high CaO/SiO_2 ratio in comparison to siliceous; see Table 3-2), and concrete gas content (LCS has ~ 2.5 times as much gas as siliceous; see Tables 3-2 and 3-5).

A third possible explanation was revealed during posttest examinations; i.e., the nature of the core-concrete interface was noticeably different for Test CCI-2 in comparison to Tests CCI-1 and CCI-3. As shown in Figures 3-9 and 3-10, the ablation front for the two tests conducted with siliceous concrete consisted of a region where the core oxide had locally displaced the cement that bonded the aggregate. Conversely, the ablation front for Test CCI-2 consisted of a powdery interface in which the core and concrete oxides were clearly separated. The interface characteristics may have influenced the heat transfer rate across the boundaries, thereby resulting in different ablation behavior for the two concrete types.

Aside from the overall cavity erosion behavior, video footage from the tests indicated that a crust was present over the melt upper surface during most of the dry cavity ablation phase for all three tests. The crusts contained vent openings which allowed melt eruptions to occur as the tests progressed. The frequency and intensity of the eruptions were directly correlated to the gas content of the concrete for a given test.

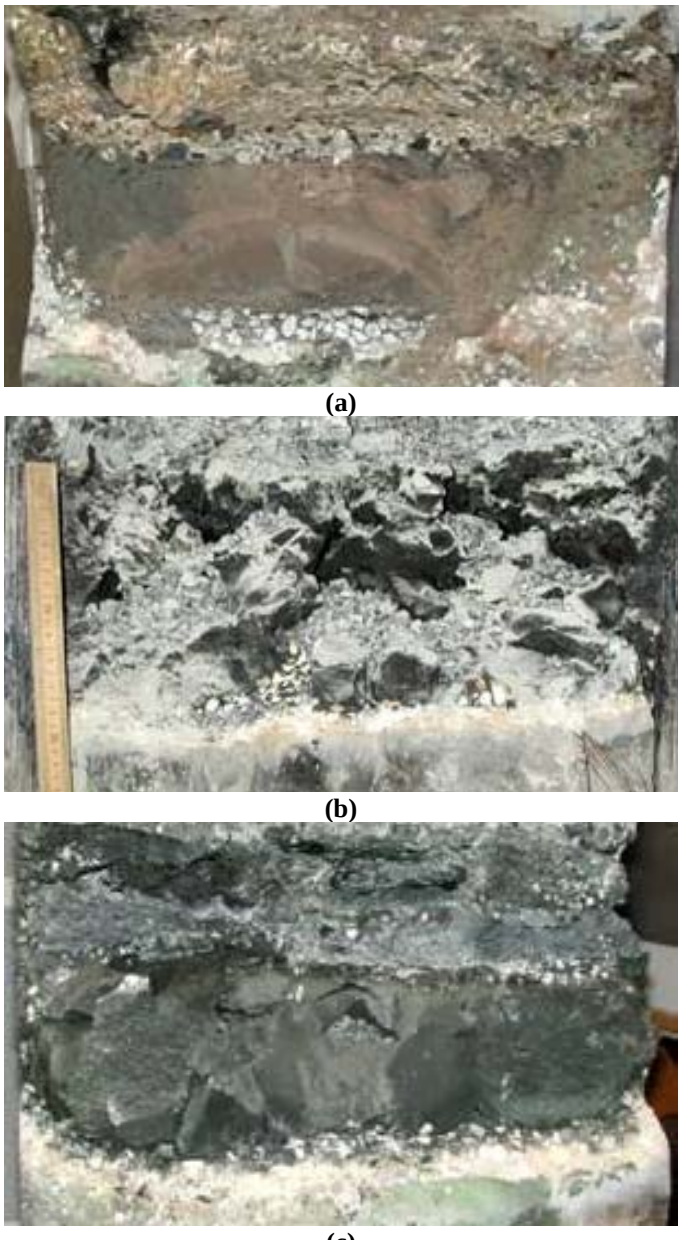

(a) **(b)** **(c)**

Figure 3-9. Axial Debris Morphology for Test: (a) CCI-1, (b) CCI-2, and (c) CCI-3.

In terms of the chemical analyses conducted as part of the test series, samples were collected to characterize the lateral and axial composition variations of the solidified debris, and also to characterize the composition of corium regions that played key roles in the coolability aspects of the tests (e.g., porous crust zones formed at the melt/water interface, and the material erupted after cavity flooding in CCI-2). Analysis of samples taken to characterize the lateral composition variation indicate that for all tests, the corium in the central region of the test section had a higher concentration of core oxides in comparison to samples collected near the two ablating concrete sidewalls. Conversely, samples taken to characterize the axial composition variation over the vertical extent of the solidified corium remaining over the basemat indicate the general trend of slightly increasing core oxide concentration as the concrete surface is approached.

For both tests conducted with siliceous concrete, two zones appeared to be present: a heavy monolithic oxide phase (10-15 cm deep) immediately over the basemat that was enriched in core oxides, with a second overlying porous, light oxide phase (5-10 cm deep) that was enriched in concrete oxides. This axial phase distribution is clearly evident in Figure 3-9. The overlying oxide phase was porous and appeared to have been quenched after the cavity was flooded. This well-defined phase distribution can be contrasted with the debris morphology for CCI-2. As shown in Figure 3-9, the debris for this test was highly porous and fragmented over the entire axial extent of the material remaining over the basemat. This open structure is consistent with the high degree of debris cooling that occurred during this test.

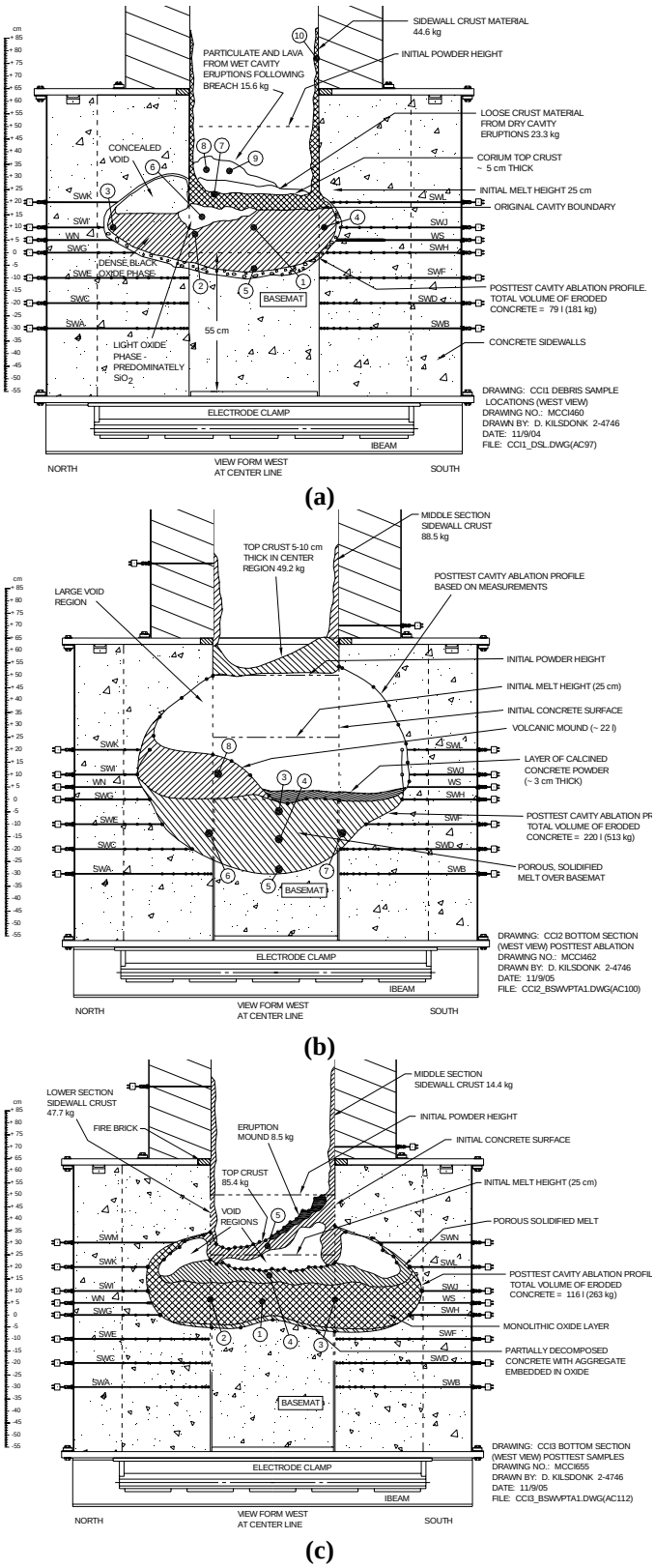

Figure 3-10. Posttest Debris for (a) CCI-1, (b) CCI-2, and (c) CCI-3.

Aside from examining the thermalhydraulic aspects of core-concrete interaction under dry cavity conditions, a second and equally important aspect of the test series was to investigate debris coolability under late-phase flooding conditions. In terms of phenomenology, four cooling mechanisms were targeted for investigation at the onset of the MCCI program: i) bulk cooling, ii) water ingression through cracks/fissures in the solidifying material, iii) melt eruptions, and iv) transient crust breach. As a whole, the test series provided data on all four of these mechanisms. In addition, Test CCI-2 provided data on water ingress at the interface between the core material and concrete sidewalls. In this test, thermocouple measurements clearly indicated that water was able to penetrate at this interface and effectively cool the concrete sidewalls to saturation, thereby terminating the lateral cavity erosion process. This mechanism had been previously identified in the COTELS reactor material test series,[8] even though these tests were conducted at a relatively high power density in comparison to those reported herein.

As shown in Figure 3-8, the heat flux during the first 5 minutes following cavity flooding was high for all tests. For the two tests conducted with siliceous concrete, the initial heat fluxes approached the Critical Heat Flux (CHF) limitation of ~ 1 MW/m^2 under saturated boiling conditions. Thus, the heat fluxes were indicative of quenching of the upper surface crust that was present as an initial condition for both tests. Although the lance was used to puncture the crust for these tests before water addition, the crusts were floating and the openings were generally small compared to the remaining crust surface area over the melt. However, for test CCI-2, the upper surface was essentially crust–free at the time of cavity flooding due to the insulating effect of the overlying crust mantles that had formed over the previous five hours of dry cavity operations. Thus, water was able to directly contact the melt, resulting in a bulk cooling transient in which the cooling rate approached 3 MW/m^2. As is evident from Figure 3-8, the heat flux eventually fell below 1 MW/m^2 after ~ 5 minutes. At this time, a stable crust most likely formed at the melt-water interface, thereby terminating the bulk cooling transient.

As is evident from Figure 3-5, the tests did not generally exhibit a pronounced decrease in overall melt temperature after cavity flooding. This is despite the fact that the heat flux and power supply responses indicated substantial debris cooling. This type of behavior can be rationalized by a latent heat transfer process in which a quench front develops at the melt/water interface, as opposed to a sensible heat transfer process in which the entire melt mass is cooled by convective heat transfer where the heat is dissipated to the overlying water by conduction across a thin crust at the melt/water interface. Indeed, after incipient crust formation at the interface, the bulk melt temperature response, power supply response in constant voltage operating mode,[a] and posttest debris morphology are consistent with the development of quenched debris zones as opposed to bulk cooldown of the entire melt mass by conduction-limited cooling across a thin crust at the interface. In fact, as shown in Figure 3-5, the average melt temperature in test CCI-2 actually increased for a period after water addition, while the debris was undergoing extensive cooling.

In order to compare the general cooling behavior, characteristic heat flux estimates were developed for each of the three tests by averaging the heat flux data over the time interval from 15-25 minutes after cavity flooding. This particular interval was selected since structure source/sink effects had effectively died away at this point, and also the onset of the melt eruption

[a]After water addition, the power supply was run in constant voltage mode to maintain the specific power density in the remaining melt zone approximately constant should a solidification (quench) front develop during the interaction. This was done since the DEH technique does not appreciably heat solidified corium.

phase had not yet been initiated in Test CCI-2.[15] Thus, the debris cooling rates should be indicative of the crust-limited heat transfer phase of the experiments. The heat flux estimates derived from the data shown in Figure 3-8 are provided in Table 3-7. Also shown in the table is the gas content of the concrete used for each test (taken from Table 3-5), as well as the concrete content of the upper crust/debris region that was in contact with the water during the time interval under consideration. As is evident from the table, the debris/water heat fluxes ranged from 250 to 650 kW/m^2. The heat fluxes for both siliceous concrete tests were lower than Test CCI-2, which was conducted with LCS concrete. Further examination of the data indicates that the heat flux increased with concrete gas content. For reference, the SSWICS water ingression heat transfer correlation (see Eq. 2-4 and Figure 2-14) predicts an ingression-limited heat flux in the range of 60-90 kW/m^2 for the concrete types and crust concrete contents shown in Table 3-7. Thus, the heat fluxes realized in the tests are several times higher than that predicted by the correlation. However, note that the SSWICS correlation was developed on the basis of core melts quenched in the absence of gas sparging. Thus, if water ingression did contribute to the overall debris quenching rate in the CCI tests, then this comparison suggests that the degree of interconnected cracks/fissures/porosity that form the pathway for water to ingress into solidifying core material is increased by the presence of gas sparging, particularly for the case in which the melt contains a high concrete fraction (e.g., > 15 wt %).

As noted above, the power supply response and melt temperature evolution after cavity flooding in the tests was indicative of a latent heat transfer (i.e., quenching) process, as opposed to convective cooling of the entire melt mass. The heat flux estimates shown in Table 3-7, in conjunction with the findings from the posttest examinations, provide the necessary information to check this hypothesis using an alternative approach. In particular, under the condition in which the crust at the melt/water interface is impervious to water ingression, then the quasi-steady crust thickness can be evaluated from the well-known expression:

Table 3-7. Debris-Water Heat Fluxes for CCI Tests Averaged Over the Time Interval 15-25 Minutes after Cavity Flooding.

Test	Concrete Type	Heat Flux (kW/m^2)	Concrete Gas Content (Wt %)	Crust Concrete Content (Wt %)	Note(s)
CCI-1	SIL (US)	250	4.6	22.3	Assumed heat transfer surface area: 0.25 m^2 (PTE indicates that water did not penetrate sidewall crusts to cool the top surface of the corium interacting with the sidewalls).
CCI-2	LCS	650	34.1	69.4	Assumed surface heat transfer area: 0.50 m^2 (PTE indicates that water was able to contact the entire melt upper surface area). Water ingress at the interface between the corium and concrete walls also contributed to cooling, but this effect has not been separated from the overall heat flux estimate.
CCI-3	SIL (EU)	500	13.5	47.8	See Note for Test CCI-1.

$$q''_{cr} = \frac{k_{cr}(T_{frz} - T_{sat})}{\delta_{cr}} \quad \Rightarrow \quad \delta_{cr} = \frac{k_{cr}(T_{frz} - T_{sat})}{q''_{cr}} \tag{3-2}$$

where q''_{cr} is the conduction-limited heat flux to the overlying water, k_{cr} is the crust thermal conductivity, T_{frz} is the crust freezing temperature, T_{sat} is water saturation temperature (100 ºC), and δ_{cr} is the crust thickness. Assuming a representative crust freezing temperature near the concrete liquidus of 1250 ºC (see Table 3-5) and a crust thermal conductivity of ~ 1.5 W/m- ºC,[28] then Eq. 3-2 predicts a crust thickness range of 3-7 mm over the range of heat fluxes shown in Table 3-7. As discussed earlier in this section, the thickness of the porous crusts formed at the melt water interface was in the range of 5-10 cm. These thicknesses are approximately an order of magnitude greater than the range predicted on the assumption of conduction-limited heat transfer. Thus, this simple analysis indicates that: i) water ingression contributed to the overall debris cooling rate realized in the experiments, and ii) the degree of interconnected porosity that forms the pathway for water ingression is increased by gas sparging during the quench process.

Aside from the water ingression mechanism, the tests also provided data on the nature and extent of the melt eruption cooling mechanism after cavity flooding. In particular, significant eruptions were observed for Test CCI-2 that was conducted with LCS concrete. However, no spontaneous eruptions were observed after cavity flooding for the two tests conducted with siliceous concrete. The absence of eruptions for this concrete type is consistent with the results of the one-dimensional MACE Test M4 that was also conducted with siliceous concrete.[2] As discussed by Bonnet and Seiler[14], the gas sparging rate during core-concrete interaction is the key parameter influencing the melt entrainment process during eruptions. Thus, the reduced gas content for this concrete type may have been a key contributor to the lack of eruptions for these two tests. Test occurrences may have also contributed to the lack of eruptions. In particular, in Test CCI-1 input power was terminated 10 minutes after cavity flooding,[15] and this short operational duration could have adversely affected the eruption process. For Test CCI-3, a partially anchored bridge crust formed during the test sequence that could have precluded eruptions from occurring.[15]

Aside from these findings, sufficient information was gathered during Test CCI-2 to evaluate the melt entrainment coefficient after cavity flooding, which is the key parameter required for modeling of this process.[14] This analysis[29] indicates that the average entrainment coefficient, defined as the ratio of the melt volumetric entrainment rate to the hot gas volumetric flowrate, was ~ 0.11 % for CCI-2. This entrainment rate is consistent with that observed in previous MACE integral effect tests,[29] and is well within the range of that required to stabilize a core-concrete interaction over a fairly significant range of melt depths.[13-14]

In addition, the entrainment coefficient data for CCI-2 is significant since the eruptions occurred under a floating crust boundary condition (as evidenced by the posttest examinations that indicated the absence of a continuous void region below the crust upper surface), and while the input power was decreasing, so that the melt zone was not over-powered during the eruption process. Thus, the data upon which the entrainment coefficient is based are deemed to be prototypic. On this basis, the entrainment coefficient may be used to evaluate the effects of the melt eruption cooling mechanism on mitigating the core-concrete interaction under plant accident conditions for the case of LCS concrete.

In terms of the crust breach cooling mechanism, both tests conducted with siliceous concrete provided data on *in-situ* crust strength, while Test CCI-1 also provided data on the

extent of debris cooling after the crust was breached. Unfortunately, neither crust strength nor crust breach cooling data was obtained for the test conducted with LCS concrete, since the mantle crusts that formed in the upper region of the test section over the five hour period preceding water addition precluded the lance from contacting the crust material that formed when the cavity was flooded. The *in-situ* crust strength data obtained from the two tests conducted with siliceous concrete are provided in Table 3-8. As is evident from the table, the crusts were very weak, with failure strengths nearly two orders of magnitude below that expected for fully dense, monolithic crust material (see Figure 2-20). Thus, these measurements support the findings from the SSWICS test series (see Section 2.0), which indicated that crust material formed during quench is structurally quite weak. However, the CCI strength measurements are significant because they were carried out under prototypic temperature boundary conditions before the material had cooled to room temperature. This can be contrasted with the SSWICS measurements that were carried out at room temperature after the specimens had been removed from the test section.

Table 3-8. Results of *In-Situ* Crust Strength Measurements for CCI Tests.

Test	Concr. Type	Region Description	Wt % Concrete in Crust	Strength (MPa)	Uncertainty Range (MPa)
CCI-1	SIL (US)	Porous crust layer over solidified melt	22.3	1.2	0.5 – 3.7
CCI-3	SIL (EU)	Porous crust layer over solidified melt	47.8	0.2	0.1 – 0.9
		Partially anchored bridge crust over porous crust	51.2	0.3	0.2 – 0.6

Aside from the crust strength measurements, examination of Figure 3-8 indicates that the CCI-1 crust breach event caused a significant transient increase in the debris cooling rate. In particular, a large melt eruption occurred, resulting in a transient cooling event in which the peak heat flux exceeded 3 MW/m^2. After the breach, the heat flux from the debris upper surface steadily declined over the next five minutes to a plateau in the range of 250-300 kW/m^2, which is similar to the plateau observed prior to the breach event. In general, the data obtained from this procedure indicates that these breach events may lead to significant transient increases in the debris cooling rate under plant accident conditions.

In terms of the findings from the chemical analyses that relate to debris coolability, the composition of the top crust regions (5-10 cm thick) formed in all tests were found to be elevated in concrete oxides relative to the core material immediately over the basemat. This finding is consistent with formation of these crusts late in the experimental sequence when the cavities were flooded. In addition, the analysis of the sample collected from the material that was erupted in test CCI-2 after cavity flooding was very close to the composition of samples collected from the top crust. This indicates that the concrete-rich oxide phase that fed the eruptions was present at the top of the melt under test conditions, as opposed to forming by gravity-driven stratification after the test was terminated.

4.0 MET TEST RESULTS

The Melt Eruption Test (MET) was a separate effects experiment focused on determining the extent that core debris is rendered coolable as a result of eruptive-type processes through the crust atop the melt. The specific objectives of this test were to: i) characterize the debris resulting from eruptions into overlying water and determine the extent to which this material is coolable, ii) evaluate the augmentation in surface heat flux during periods in which eruptions occur, and iii) provide sufficient information to evaluate the melt entrainment coefficient from the heat flux and gas flow rate data for input into models that calculate ex-vessel debris coolability. The experimental approach was to utilize a test section that featured an inert basemat with remotely controlled gas sparging to mock-up concrete decomposition gases. The use of an inert basemat for this type of test would eliminate the tendency for the melt to separate from the crust by the mechanism of basemat densification upon melting. The externally supplied gas source for concrete decomposition gas simulation provided control over the principal parameter influencing the melt entrainment rate.[14] Moreover, the gas flow rate (as opposed to the input power) could, if melt separation occurred, be used to reestablish melt/crust contact through an increase in the melt pool void fraction.

One MET was attempted as part of the program; specifications for this experiment are provided in Table 4-1. Unfortunately, this test was not operationally successful. However, as described later in this section, melt eruption data was successfully obtained as part of the CCI test series, as well as in other test programs[1-2] that formed the technical basis for the current work. These results are also summarized in this section in order to provide the modeling basis for the plant calculations that are provided in Section. 6.0.

The MET test facility consisted of a test apparatus, a power supply for Direct Electrical Heating (DEH) of the corium, a basemat gas sparging system, a water supply system, two steam condensation (quench) tanks, a ventilation system to filter and exhaust the reaction product gases, and a data acquisition system. Key facility features are illustrated in Figure 4-1. Additional details regarding the overall facility design and test operating procedure are provided elsewhere.[30]

4.1 Test Apparatus

The test section for containment of the corium melt was 3.4 m tall with a square internal cross-section measuring 50 cm x 50 cm. The porous MgO basemat was located at the bottom of the test section (Figure 4-2). Like the SSWICS and CCI tests, the initial 350 kg melt mass for the experiment was generated *in-situ* using an exothermic chemical reaction over a timescale of ~ 30 seconds. The initial melt composition following the reaction is provided in Table 4-2.

After the melt generation phase, DEH was utilized to maintain melt temperature through two banks of tungsten electrodes located on opposite sidewalls of the test section. Operationally, the power supply would be used to initially heat the melt to the target temperature of ~ 2000 ºC prior to water addition. Thereafter, the overall heating rate would be adjusted to correspond to a specified decay heat level for the experiment (viz., nominally 300 W/kg fuel).

The inert basemat was constructed from castable MgO. The basemat was cast with an array of 1 mm diameter gas sparging holes with a surface density of 7 holes/100 cm^2. The upper surface of the MgO was also protected by a ~ 5 cm thick layer of crushed UO_2 pellets, which

served two purposes: i) prevent freeze-induced plugging of the holes after the melt generation phase, and ii) enhanced the uniformity of the gas flow through the melt by acting as a secondary sparger plate. During the melt generation phase, a slow gas purge through the basemat was used to ensure that a uniform flow field was established and maintained. A layer of crushed pellets was also used to protect the interior surface of each MgO sidewall against thermo-chemical attack by the corium.

Table 4-1. MET Specifications.

Parameter	Specification
Corium Composition	100 % oxidized PWR with 25 wt % siliceous concrete
Initial melt mass	350 kg
Basemat Type	Porous inert (MgO) with remotely controlled gas sparging.
Basemat Cross-Sectional Area	50 cm x 50 cm
Initial melt depth	25 cm
Initial melt temperature	2000 ºC
Melt formation technique	Chemical reaction (~30 seconds)
Melt heating technique	Direct Electrical (Joule) Heating
System operating pressure	Atmospheric
Criteria for water addition	Melt temperature stabilizes at 2000 ºC or maximum achievable
Inlet water temperature	20 ºC
Inlet water flow rate	2 liters/second
Sustained water depth over melt	50 ± 5 cm
Power supply operating mode after water addition	Constant voltage (i.e., constant specific power density in melt zone of ~ 300 W/kg UO_2)
Test termination criteria	1) Corium is quenched, or 2) steady state conditions are reached at maximum melt sparging rate.

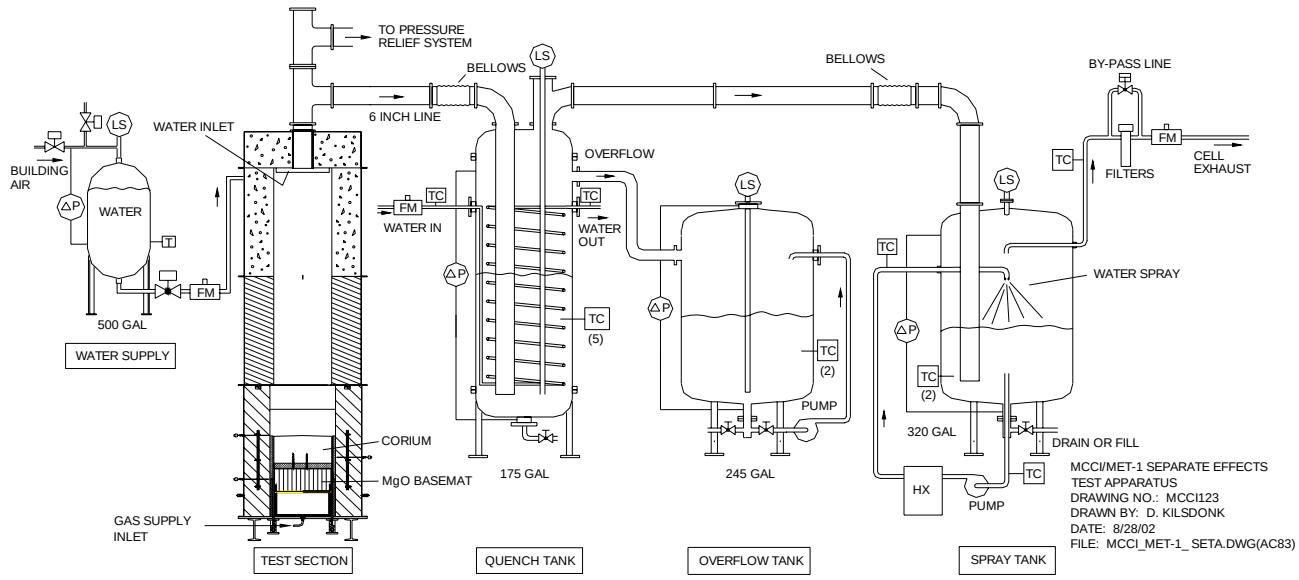

Figure 4-1. Key Elements of the MET Apparatus.

The gas used to simulate the basemat decomposition gases was a specialty blend of argon and helium, with the relative ratio of these two gases (50% argon-50% helium), selected such that the mixture density was within 20 % of the decomposition gas for the given concrete type under fully oxidized melt conditions. Gas flow to the basemat was monitored and controlled with a gas supply system that had both primary and back-up flow path capabilities. The system is shown schematically in Figure 4-3. Following cavity flooding, this system would be used to provide an initial constant melt superficial gas velocity of ~3 cm/sec. The flowrate would be held constant at this level until steady state conditions were achieved with no coolability mechanisms active for a period of 10 minutes. After steady state was reached, the superficial gas velocity would be increased by 3 cm/sec and held at the new level until state conditions were reached for an additional 10 minutes. This overall procedure would be repeated until the debris was completely quenched, or steady state was reached at the peak gas flow rate of ~ 15 cm/sec

Table 4-2. MET-1 Initial Melt Composition.

Constituent	Wt %	Mass (kg)
UO_2	48.53	169.86
ZrO_2	19.94	69.79
SiO_2	18.12	63.42
MgO	0.18	0.63
Al_2O_3	1.06	3.71
CaO	3.54	12.39
Cr	8.63	30.20
Total	100.00	350.00

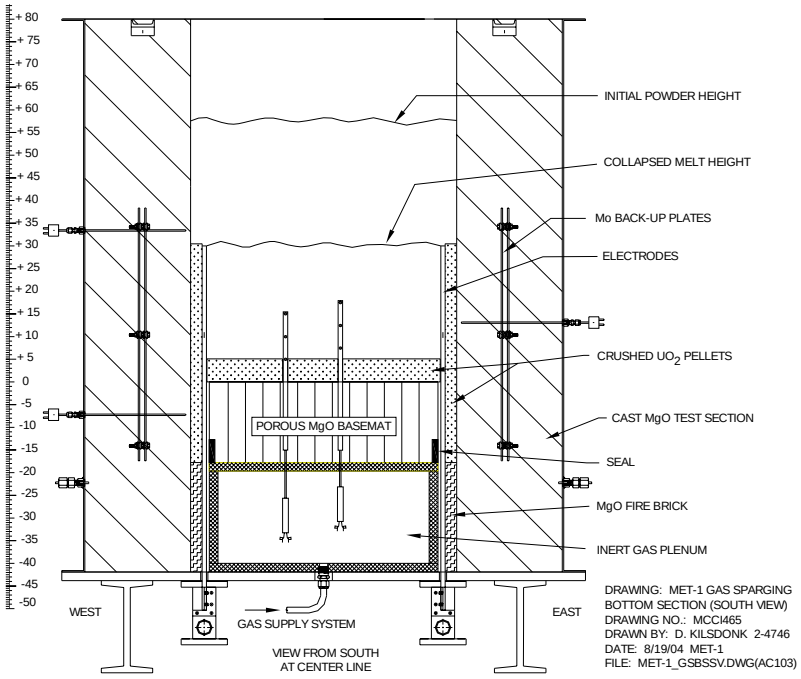

Figure 4-2. MET Lower Test Section Design.

Water would be delivered above the melt by two weirs located at the top of the test section on the sidewalls adjacent to those with the electrodes. Water would initially be added at a steady rate to ensure that the quench process was not water-starved. Thereafter, makeup would be added to maintain the head roughly in the range of 50 ± 5 cm as the quench process continued.

A 15 cm diameter line on the lid of the test section vented noncondensable gases and steam to the adjacent primary quench tank, which was cooled with a large coil. An overflow tank collected excess condensate from the quench tank. Downstream from the quench tank was a secondary spray tank that performed an identical condensation/gas cleanup function.

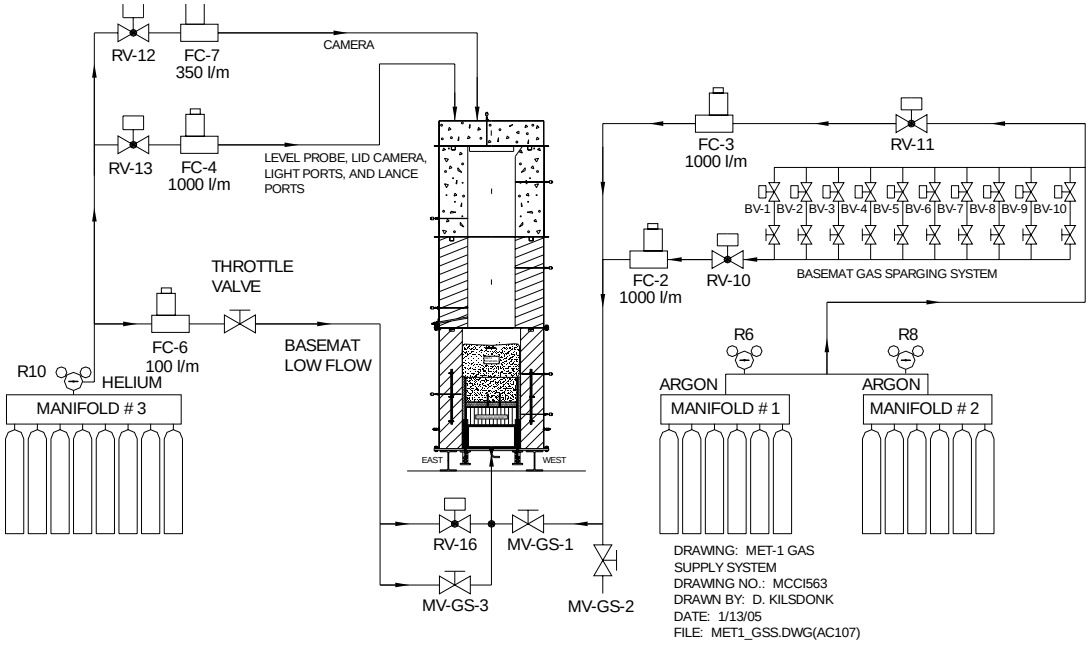

Figure 4-3. MET-1 Basemat Gas Sparging System.

After passing through the quench system, the basemat sparging gas and any noncondensables arising from the melt/water interaction were vented through an off gas system that included a demister, filters, and gas flow meter. The off gases were eventually exhausted through the containment cell ventilation system where they flowed through a series of high efficiency filters before finally being released from the building stack.

Aside from characterizing the debris formed as a result of eruptive processes, the key data to be obtained from this test would be the melt entrainment rate as a function of the gas sparging rate. The slope of the line fit to the entrainment rate data then determines the melt entrainment coefficient, which is the key piece of information needed for model development.[14]

4.2 Instrumentation

Instrumentation was selected to provide all measurements necessary to determine the time dependent melt/water heat flux and the melt temperature distribution. In terms of evaluating the melt/water heat flux, the water supply tank was equipped with level sensors and a flowmeter to measure the water addition rate to the test section. The test section was equipped with water level sensors, thermocouples, and pressure transducers to monitor the water level over the melt and also to correct the steaming rate for quenching of extraneous structures above the melt surface. The quench system tanks were instrumented with thermocouples, level sensors, and pressure transducers to monitor transient energy deposition in the system so that the necessary energy balance information could be extracted.

A plan view of the basemat instrumentation layout is provided in Figure 4-4, while an elevation view of the Type C melt temperature thermocouple locations is shown in Figure 4-5. As is evident from these figures, a total of five three-junction Type C thermocouple assemblies within tungsten thermowells were provided to measure melt temperature. The basemat was also cast with three four-junction Type K thermocouple assemblies to monitor the basemat temperature during the test. The information from these TC's would be used to evaluate the heat

loss into the underlying MgO using standard inverse heat conduction techniques. Other significant test instrumentation included both stationary (lid mounted) and insertable (water cooled) video cameras for observing various stages of the interaction.

4.3 Results

The event sequence for MET-1 is provided in Table 4-3. Time t=0 in this table, as well as all data plots, corresponds to completion of the thermite burn, as evidenced by rapidly escalating temperatures recorded by thermocouples located immediately above the UO_2 pellet layer protecting the MgO basemat (see Figure 4-5). Key data relevant to the interpretation of the experimental results includes the power supply operating parameters and temperatures in the melt zone; these data are provided in Figures 4-6 through 4-8, respectively.

As shown in Table 4-3, the melt generation phase of the experiment went according to plan; the thermite burn produced a well-defined melt pool at ~ 1860 ˚C. The melt was highly fluid at this temperature, as evidenced by the very thin sidewall crusts that were deposited above the collapsed melt pool height during the burn.

After the burn was completed, the input power was ramped up to a level of ~ 140 kW for the preheat stage of the test. As noted in Table 4-3, the effective resistance of the melt was very unstable at this point, resulting in power oscillations of ±10 kW.

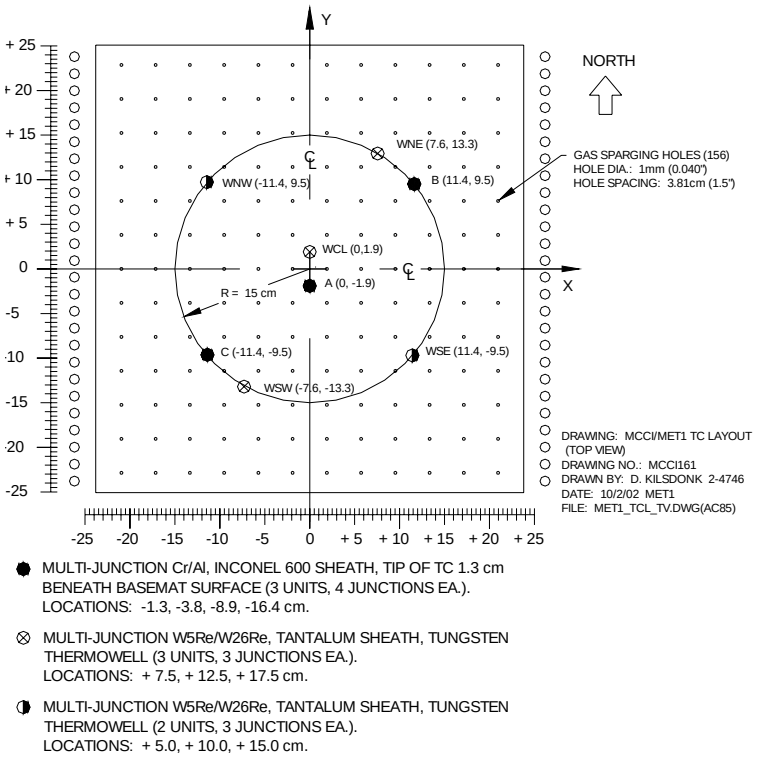

Figure 4-4. Plan View of the MET MgO Basemat Instrument Layout.

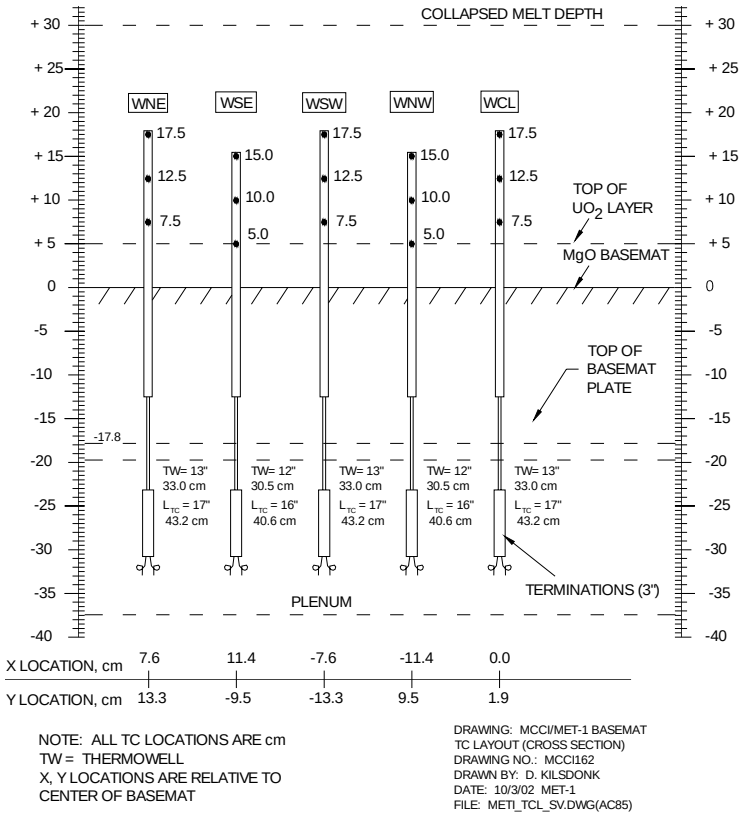

Figure 4-5. Elevation View of MET Type C Thermocouple Junction Locations.

Table 4-3. MET-1 Event Sequence.

Time (Minutes)	Event
0.0	Thermite ignition.
0.4	Thermite burn completed; T_{melt} ~ 1860 ˚C. DEH power ramp to preheat level initiated.
4.6	Power input reaches 140 kW. Melt resistive load is very unstable. The load remained unstable over the balance of power supply operations.
6.1	Melt temperature falls to ~ 1840 ˚C and then starts to increase.
11.3	Average melt temperature climbs to ~ 2000 ˚C. Power input reduction to the target of 70 kW for water addition stage initiated.
15.4	Target power of 70 kW is reached, but the melt temperature falls from 2000 ˚C to < 1400 ˚C during the power reduction. On this basis, the preheat is continued.
18.5	Power supply increase initiated; melt temperature falls to a minimum of ~1270 ˚C.
20.4	Input power reaches ~ 110 kW where it is kept for the balance of the test.
18.5-56.0	Average melt temperature steadily increases to 1500 ˚C. Basemat and melt zone sidewall surface temperatures steadily increase, but all remain at or below 550 ˚C.
16.2-52.5	Basemat gas flowrate varied in the range of 60-290 slpm to increase convection and reduce temperature variations in the melt.
56.4	Flash seen on melt surface video camera. Melt discharge from the bottom of the test section is evident on surveillance cameras. Power input terminated.
58.5-69.5	Water added to the test section to cool the melt spread onto the containment floor.

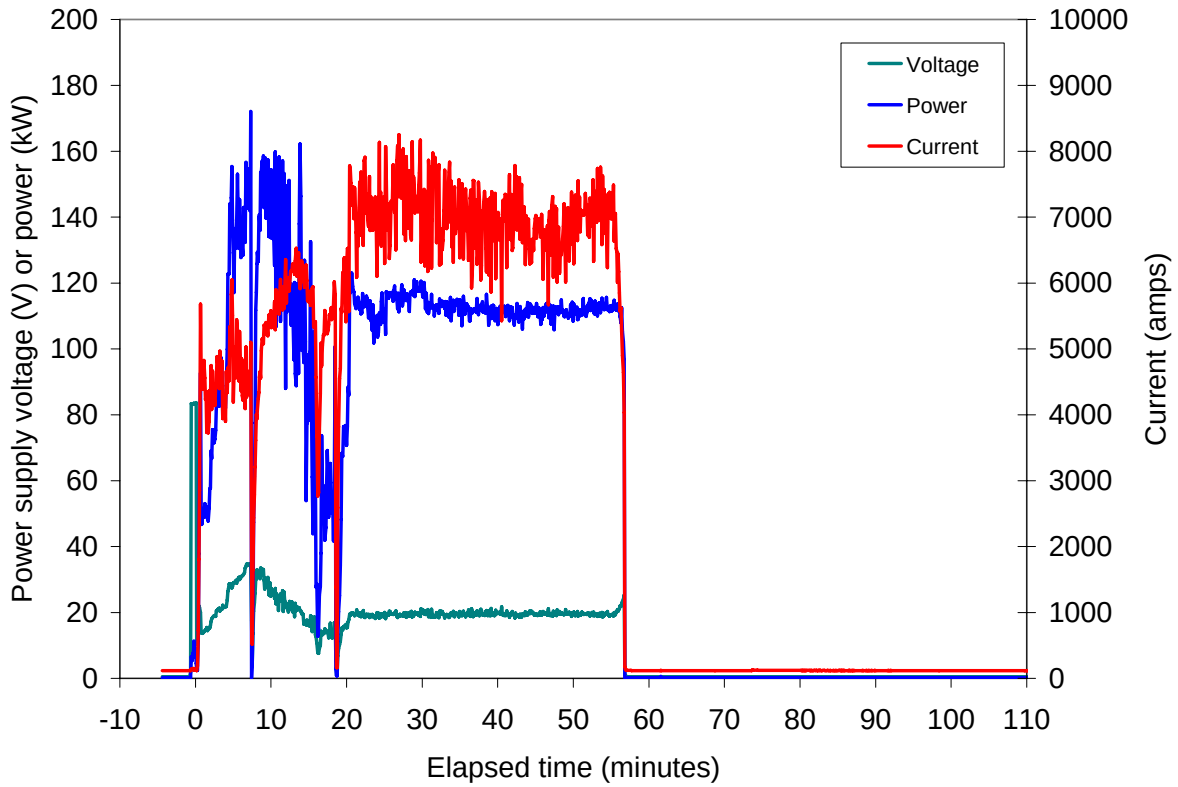

Figure 4-6. Power Supply Voltage, Current, and Power.

Despite the instability, preheat continued, and the melt temperature gradually climbed to the target level of 2000 ˚C for cavity flooding. At this point, the power was gradually reduced to the prescribed level of 70 kW for the water addition stage.

However, following the power reduction to target power of ~ 70 kW, the melt temperatures plummeted to ~ 1270 ˚C. The experimentalists were concerned that the melt may have resolidified at this temperature. As a result, an attempt was made to reheat the melt to a temperature at which melt fluidity would be expected (~ 1800 ˚C). After ~ 40 minutes of reheat at ~ 110 kW input power, the apparent corium temperature had climbed back to ~ 1600 ˚C. As shown in Figures 4-9 and 4-10, the basemat and test section inner sidewall temperatures stayed relatively cool (i.e., < 600 ˚C) during this phase.

At 56 minutes in the experimental sequence, the test section assembly failed, leading to discharge of ~ 250 kg of molten corium from the bottom of the test section that was spread onto the floor of the containment cell. A photograph showing the spread material at the base of the test section is provided in Figure 4-11. The experiment was subsequently terminated on the basis that worthwhile operation was no longer feasible.

The posttest examinations indicated that the melt had penetrated the 1.6 cm opening between the electrodes and MgO basemat in the southwest corner of the test section; a photograph is provided in Figure 4-12. As

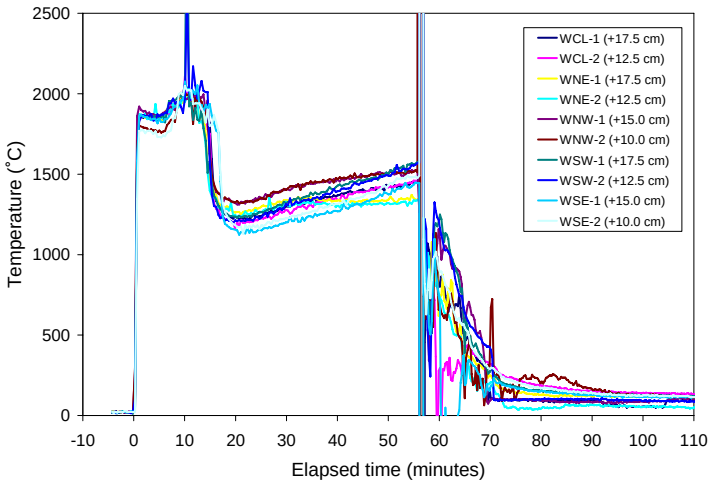

Figure 4-7. Temperatures in the Upper Melt Region.

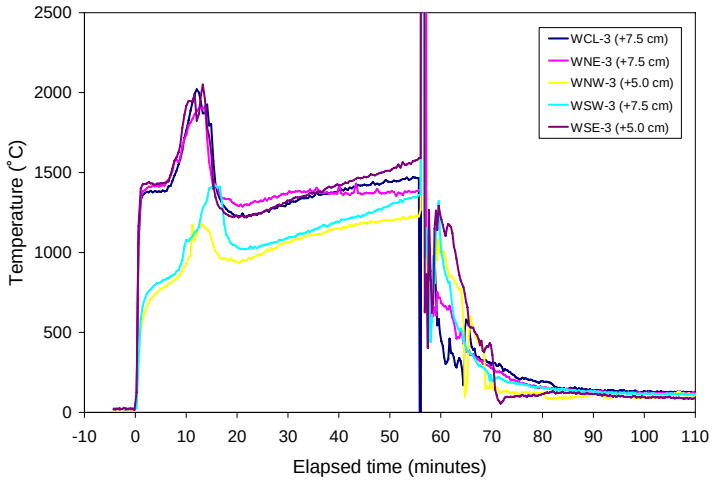

Figure 4-8. Temperatures in the Lower Melt Region.

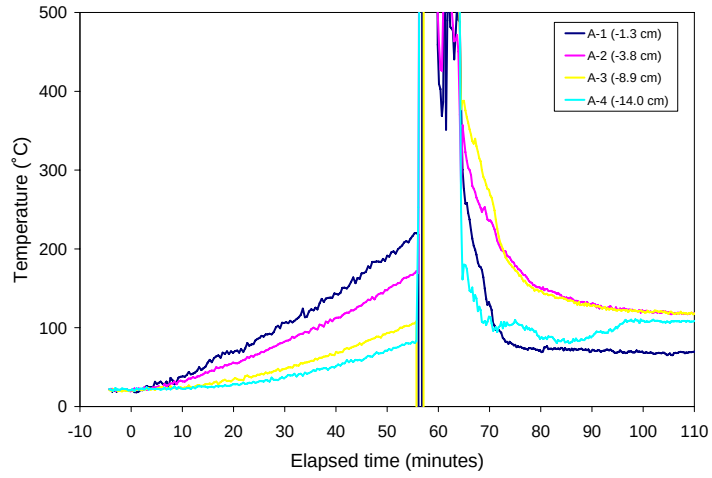

Figure 4-9. Basemat Thermal Response Near Centerline.

described earlier, this gap was filled with crushed UO_2 pellets. The data indicates that excessive heatup of the material in the gap (most likely driven by positive feedback of the resistance heating method) caused a local hot spot to form. As a result, the melt gradually penetrated down into the gap through the pellets until it reached the gas sparging plenum. The plenum and test section bottom support plate were both constructed from aluminum (to prevent inductive heating from the power supply). As a result, the melt readily penetrated these structures and subsequently spread onto the containment floor.

Further examinations indicated that the melt had aggressively attacked the tungsten electrodes, as well as the tungsten thermowells that protected the melt temperature thermocouples. As a result, the temperatures shown in Figures 4-7 and 4-8 probably represent measurements from false junctions that formed at, or just below, the UO_2 pellet layer protecting the basemat surface (see Figure 4-5). Thus, the temperature decline in these figures is most likely fictitious, and the actual bulk melt temperature was probably much closer to the corium liquidus temperature. This conjecture is supported by the fact that the melt readily spread after failing the test section, indicating that the melt was very fluid at the time the test section failed.

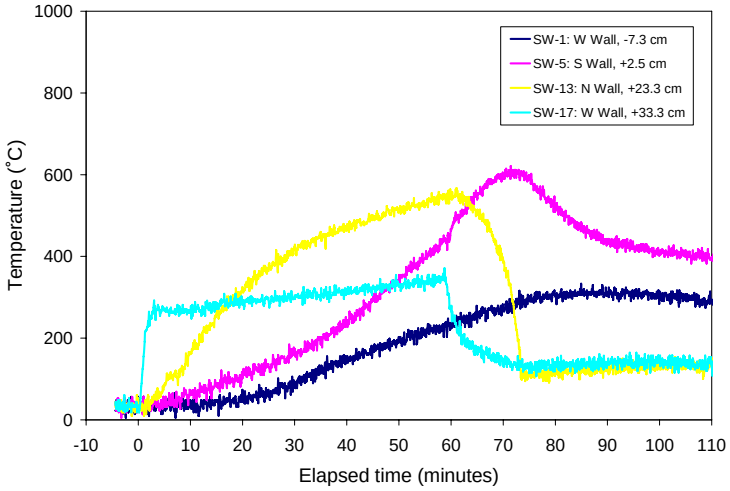

Figure 4-10. MgO Sidewall Inner Surface Temperatures.

Figure 4-11. Southwest View of Test Section Showing Corium Spread onto the Test Section Bed.

Figure 4-12. West View of Electrodes Showing Melt-through of Gas Plenum (Lower Right Hand Side).

No physical evidence of a corium interaction with the MgO sidewalls or basemat was discovered during the disassembly process. In addition, chemical analysis of several samples of the spread melt indicated that the composition of the spread material agreed with the initial composition (Table 4-2) to within the measurement uncertainty associated with the chemical analysis. On these bases, chemical interaction with the MgO crucible was ruled out as a potential contributor to the failure of the test section.

Although MET-1 did not provide data for estimating the melt entrainment rate during eruptions, entrainment rate data was nonetheless obtained as part of the CCI test series (see Section 3.0), as well as in other reactor material test programs[1-2] that formed the technical basis for the current work. These results are summarized next in order to support the modeling basis for the plant calculations that are provided in Section. 6.0.

4.4 Review of Reactor Material Melt Eruption Database

As part of the project efforts to assess the melt eruption cooling mechanism, the reactor material database was reviewed[29] to provide a technical basis for model development and validation activities. In addition to the current program, melt eruption data was obtained as part of the MACE test series,[1-2] which included both separate[31] and integral effect[32-35] tests. In that program, tests were conducted with both siliceous and limestone/common sand concrete types.

Average entrainment coefficient estimates for these tests were made[29] based on the measured mass of erupted material, as well as the measured (or estimated) total gas release over the time intervals in which the melt was deduced to be in contact with the crust. In general, melt dispersal during eruptions is calculated by assuming that the melt entrainment rate is proportional to the gas volumetric flowrate times an entrainment coefficient; i.e.,[14]

$$j_m = K_e j_g \tag{4-1}$$

where K_e is the entrainment coefficient, j denotes superficial gas velocity, and subscripts m and g denote the melt and sparging gas phases, respectively. For the tests, the average entrainment coefficient was estimated from the equation:

$$K_e = \frac{V_m}{V_g} \tag{4-2}$$

where V_m is the total volume of erupted material, and V_g is the total hot gas volume of concrete decomposition gases released during the estimated periods of melt-crust contact. The entrainment coefficient estimates developed on this basis are provided in Table 4-4. As shown in the table, eruption data was obtained for all tests (both integral and separate effect) conducted with limestone/common sand concrete. The entrainment coefficients ranged from 0.06 to 0.25 % for these tests; the melts contained 8 to 60 wt % LCS concrete. The entrainment data for CCI-2 is particularly important since the eruptions occurred under a floating crust boundary condition and while the input power was decreasing, so that the melt zone was not over-powered during the eruption process.[15] Thus, the entrainment coefficient estimate for this test is believed to be representative of prototypic conditions.

Table 4-4. Melt Entrainment Estimates for Various Reactor Material Separate and Integral Effect Tests.

Project and Test	Test Type – Scale	Concrete Type	Average Entrainment Coefficient (%)	Entrainment Coefficient From Rico-Spalding Correlation (%)	Notes
MACE MSET-1	Separate Effect, 1-D, 50 cm x 50 cm	LCS	0.078-0.25	0.045	Anchored crust.
MACE M4	Integral, 1-D, 50 cm x 50 cm	SIL	0.0	0.058	Anchored crust; analysis indicated that melt did not re-contact crust after the initial separation. Thus, eruptions not possible.
MACE M3b	Integral, 1-D, 120 cm x 120 cm	LCS	0.063	0.055	Anchored crust; significant power increase during eruption time interval.
MACE M1b	Integral, 1-D, 50 cm x 50 cm	LCS	0.072	0.050	Anchored crust.
MACE M0	Integral, 3-D, 30 cm x 30 cm	LCS	0.099	0.062	Anchored crust. Elevated power density over the entire test.
MCCI CCI-3	Integral, 2-D, 50 cm x 50 cm	SIL	0.0	0.058	Partial crust anchoring that may have adversely affected the melt eruption process.
MCCI CCI-2	Integral, 2-D, 50 cm x 50 cm	LCS	0.11	0.063	No crust anchoring. Eruptions occurred while power was decreasing. Thus, most prototypic eruptions produced to date.
MCCI CCI-1	Integral, 2-D, 50 cm x 50 cm	SIL	0.0	0.055	DEH power input terminated 10 minutes after cavity flooding.

Further examination of Table 4-3 indicates that no spontaneous eruptions occurred after cavity flooding for the three tests conducted with siliceous concrete. As discussed by Bonnet and Seiler[14], the gas sparging rate during core-concrete interaction is the key parameter influencing the melt entrainment process during eruptions. Thus, the reduced gas content for this concrete type may have been a key contributor to the lack of eruptions for these tests. Test occurrences may have also contributed to the lack of eruptions. In particular, in Test CCI-1 input power was terminated 10 minutes after cavity flooding,[15] and this short operational duration could have adversely affected the eruption process. For Tests CCI-3[15] and MACE M4,[32] anchored bridge crusts formed during the test sequences that could have precluded eruptions from occurring.

In terms of extrapolating the entrainment rate data to plant conditions, a correlation for the entrainment coefficient in Eq. 4-1 is required. As part of the PERCOLA simulant experiment test program,[36] Tourniaire and Seiler[37] have developed detailed models of the entrainment rate for both ejection and extrusion-type eruption processes during core-concrete interaction. In addition, Cheung and Epstein[38] have pointed out that the entrainment coefficient for gas-liquid systems under a wide variety of flow conditions can be evaluated with the following correlation that was originally developed by Ricou and Spalding for the evaluation of entrainment from turbulent jets,[39]

$$K_e = E\left(\frac{\rho_g}{\rho_m}\right)^{1/2} \tag{4-3}$$

where E is a proportionality constant which ranges from 0.06 to 0.12. Equation 4-3 is compared with the entrainment coefficient estimates for the various tests in Table 4-4 with the proportionality constant set at $E = 0.08$. As is evident, this correlation provides a conservative estimate of the actual entrainment coefficients for the various tests in which eruptions occurred. On this basis, this simple correlation is adopted for the purposes of carrying out plant calculations that are provided in Section 6.0.

5.0 CORRELATION OF FINDINGS

The previous sections of this report have summarized key findings from the three test series that were conducted as part of the program (Table 1-1). Data from the tests were used to develop and validate correlations for the coolability mechanisms that were originally targeted for investigation (Table 1-2). These correlations form the basis for extrapolating the results to plant conditions. The objectives of this section are to: i) summarize these correlations in a consolidated format, and ii) outline a methodology by which the correlations can be employed in an overall numerical scheme for extrapolating the findings to plant conditions. A summary of the key coolability-related modeling results developed as part of the program is provided in Table 5-1.

5.1 Bulk Cooling

Upon initial cavity flooding, the melt sparging rate may be sufficiently high enough to preclude stable crust formation at the melt-water interface. In this case, efficient heat transfer will occur due to conduction and (predominately) radiation heat transfer across the agitated (i.e., area-enhanced) melt-water interface. However, due to the high heat transfer rate, the melt temperature will decrease, which will cause the gas sparging rate due to core-concrete interaction to decrease. Thus, a point will eventually be reached at which a stable crust will form, thereby terminating the bulk cooling transient.

Bulk cooling was not explicitly targeted for investigation as part of this program since the existing database[1,2] was deemed to be adequate, and validated models of this heat transfer mechanism had already been developed.[40,41] These models are summarized here for completeness.

In cases where the melt/water interfacial temperature lies above the corium freezing temperature, crust formation is clearly not possible. However, when the interface temperature falls below freezing temperature, a stable crust may form if it is mechanically stable with respect to the sparging gases. If the crust has insufficient strength, then thin crust segments will form, but the segments will be continuously broken up by the sparging gas and mixed back into the melt. The formation of the crust segments effectively fixes the melt pool surface temperature at the corium freezing temperature. Under these conditions, the heat transfer coefficient between the melt pool and overlying water can be evaluated from the following equation:[39]

$$h_w \sim A_* h_r, \tag{5-1}$$

where h_r is the radiant heat transfer coefficient and A_* is the dimensionless surface area enhancement, respectively. These parameters are evaluated through the expressions,

$$h_r = \eta\varepsilon(T_f^2 + T_{sat}^2)(T_f + T_{sat}), \tag{5-2}$$

$$A_* = 1 + 4.5\frac{j_g}{U_T}, \tag{5-3}$$

where η = Stefan-Boltzman constant, ε = melt emissivity, T_f = melt freezing temperature, T_{sat} = coolant saturation temperature, j_g = melt sparging rate, and U_T is the sparging gas bubble radius which is evaluated through the expression:[42]

Table 5-1. Summary of Principal Modeling Results for the MCCI Program.

No.	Research Objective:	Principal Research Result	Ramifications for Severe Accident Management:
1	Quantify corium dryout heat flux as a function of corium composition and system pressure	C ~ 5.5 for: $$q''_{dry} = C\left(\frac{h_{lv}(\rho_l-\rho_v)g}{\nu_v}\right)^{5/13}\left(\frac{Nk^2\Delta e^i_{sat}}{c(1-\eta)}\right)^{4/13}\bullet \left(\alpha_{\exp}\left[T_{sol}-\left(T_{sat}+\frac{\sigma_{tensile}}{\alpha_{\exp}E}\right)\right]\right)^{15/13}$$	Dryout heat flux decreases rapidly with concrete content. Thus, for this mechanism to be effective, early water addition following vessel failure is important.
2	Obtain crust macroscopic strength data to determine if crusts are mechanically stable at plant scale.	Crust failure strength σ_f ~ 1- 3 MPa for: $$\left(\rho_{cr}\delta_{\min}g+\rho_l H_w g+m''_{bed}g\right)A \geq C_{geom}\sigma_f\delta^2_{\min}$$	Crust will not be mechanically stable at plant scale for virtually all conceivable crust thicknesses. Resultant crust failures will allow coolability mechanisms (i.e., water ingression and melt eruptions) to proceed to their full physical limitations.
3	Quantify the entrainment coefficient for melt eruptions during core-concrete interaction.	E ~ 0.08 for: $$K_e = E\left(\frac{\rho_g}{\rho_m}\right)^{1/2}$$	Test results indicate that K_e is in the range of 0.06 to 0.25 % for the case of LCS concrete, which is within the range of that required to achieve debris coolability for a wide range of melt depths.[13,14] Eruptions were not observed in tests with siliceous concrete, but the lack of eruptions may be attributable to test occurrences that precluded eruptions from occurring.

$$U_T = 1.4\left(\frac{g(\rho_m - \rho_g)\sigma_m}{\rho_m^2}\right)^{1/4}, \tag{5-4}$$

where g = gravitational constant, ρ_m = melt density, ρ_g = gas density, and σ_m = melt surface tension.

Equations 5-2 and 5-3 are valid as long as a stable crust is not able to form at the interface. The correlation for the critical superficial gas velocity below which a stable crust forms can be estimated from the following correlation:[40]

$$j_{g,crit} = \frac{0.445Rh_m(T_m - T_f)}{\delta_{crit}\rho_{cr}\Delta e_{cr}\left\{\frac{k_{cr}(T_f - T_{sat})}{\delta_{crit}h_m(T_m - T_f)}\ln\left[\frac{1}{1-\xi}\right] - 1\right\}}, \tag{5-5}$$

where:

$$\xi = \frac{h_m h_r (T_m - T_f)\delta_{crit}}{k_{cr}\left\{h_r(T_f - T_{sat,}) - h_m(T_m - T_f)\right\}}, \tag{5-6}$$

And h_m = heat transfer coefficient from melt to crust, T_m = melt freezing temperature, k_{cr} = crust thermal conductivity, ρ_{cr} = crust density, Δe_{cr} = crust latent heat of fusion, R = sparging gas bubble radius, and δ_{crit} = critical crust thickness at failure under the applied buoyancy load of a gas bubble impacting the bottom of the crust, viz.,

$$\delta_{crit} = 0.69\left(\frac{R^3(\rho_m - \rho_g)g}{\sigma_y}\right)^{1/2}, \tag{5-7}$$

where σ_y is the crust tensile strength for fully dense material without any crack structure present.

The above equations describe the melt/water heat transfer rate in the early part of the interaction prior to formation of a stable crust. After the crust forms, the water ingression, melt eruption, and crust breach cooling mechanisms become active. The correlations that were developed on the basis of the test results for these three mechanisms are summarized next.

5.2 Water Ingression

After stable crust growth is initiated, the particular form of the boundary condition at the crust upper surface depends upon whether there is an overlying particle bed that develops due to melt eruptions. In the outline presented below, the presence of a particle bed is neglected since it simplifies the presentation; the reader is referred elsewhere[13] for a description of appropriate modeling corrections when a particle bed is present. For situations in which a bed is absent and the crust is impervious to water ingression, then the crust growth rate equation under the assumptions of uniform crust physical properties and decay heat distribution is of the form:

$$\rho_{cr}\Delta e_{cr}\frac{d\delta}{dt} = k_{cr}\frac{(T_f - T_{sat})}{\delta} - \frac{\chi_{UO_2}\rho_{cr}q_{dec}\delta}{2} - h_m(T_m - T_f) \tag{5-8}$$

where χ_{UO_2} = weight fraction fuel in the crust and q_{dec} = decay heat level (assumed to be proportional to fuel density). In this formulation, it is assumed that film boiling has broken down and thus the crust upper surface temperature has fallen to near the coolant saturation temperature. In general, water ingression cannot commence until film boiling has broken down and the coolant is in sustained contact with the crust. The reader is spared a detailed evaluation of boiling regime maps that would be used to predict when film boiling would break down, since that would detract from the primary subject.

Assuming that the crust contains porosity (cracks, fissures) that are permeable and the crust can be characterized by an effective dryout heat flux q''_{dry}, then the condition for onset of water ingression is that the total heat flux from the crust upper surface falls below the dryout limit; i.e.,

$$q''_{dry}(P, \chi^m_{con}) \geq k_{cr} \frac{(T_f - T_{sat})}{\delta} + \frac{\chi_{UO_2} \rho_{cr} q_{dec} \delta}{2} + \rho_v h_{lv} j_{nc}\Big|_{T_{sat}} \qquad (5\text{-}9)$$

where ρ_v = steam density, h_{lv} = coolant latent heat of vaporization, j_{nc} = superficial velocity of noncondensables (H_2, CO, CO_2) sparging through the melt due to core-concrete interaction, P = system pressure, and χ^m_{con} = concrete content within the melt. In this equation, the assumption has been made that the noncondensable gas flow is vented uniformly across the extent of the crust. Note, however, that the MACE test data[1,2] indicates that at least part of these gases are vented at discrete locations through the crust. Thus, the above equation makes the conservative assumption that the MCCI gas flow acts as a counter-current flow limitation if the flow rate is sufficiently high. Further note that the gas flow rate is evaluated at water saturation temperature based on the assumption that the debris above the dryout front is maintained at saturation temperature. Finally, note the functional dependence of the dryout limit on the system pressure, but most importantly, the time-dependent concrete content in the melt, χ^m_{con}. In particular, this equation implies that for water-ingression to proceed, the dryout limit corresponding to the particular melt composition at a given time (corrected for counter-current noncondensable gas flow) must exceed the convective heat transfer to the underside of the crust, plus the thermal load due to decay heat within the crust.

Equation 5-9 defines the conditions for onset of water ingression. After ingression begins, the crust growth rate equation takes the form:

$$\rho_{cr} \Delta e_{m,sat} \frac{d\delta}{dt} = q''_{dry}(P, \chi^m_{con}) - \chi_{UO_2} \rho_{cr} q_{dec} \delta - \rho_v h_{lv} j_{nc}\Big|_{T_{sat}} - h_m (T_m - T_f) \qquad (5\text{-}10)$$

where $\Delta e_{m,sat}$ = corium specific enthalpy change upon quench from the T_m to T_{sat}. Under these conditions, the thermal boundary condition on the melt zone remains the same (i.e., the melt is cooled by convective heat transfer to an overlying crust that is maintained at a constant temperature, T_f). However, the heat flux to the overlying water pool approaches a constant that corresponds to the crust dryout limit, q''_{dry}.

In terms of thermalhydraulic results, the main finding from the SSWICS test series (Section 2.0) was a correlation for the dryout heat flux, $q''_{dry}(P, \chi^m_{con})$, as a function of system pressure and corium concrete content. This correlation is of the form:

$$q''_{dry} = C\left(\frac{h_{lv}(\rho_l - \rho_v)g}{\nu_v}\right)^{5/13}\left(\frac{Nk_{cr}^2(\Delta e_{sat})^2}{c_{cr}\Delta e_{crack}}\right)^{4/13}\left(\alpha_{\exp}\left[T_{sol} - \left(T_{sat} + \frac{\sigma_y}{\alpha_{\exp}E_{cr}}\right)\right]\right)^{15/13} \quad (5\text{-}11)$$

where C = empirical constant, c_{cr} = crust specific heat, Δe_{sat} = corium specific enthalpy change upon quench from the T_f to T_{sat}, Δe_{crack} = corium specific enthalpy change upon cooldown from T_f to T_{crack}, E_{cr} = corium elastic modulus, α_{exp} = corium linear expansion coefficient, T_{sol} = crust solidus temperature, N = numerical constant = 0.1 K-m$^{1/2}$, ρ_l = coolant density, and ν_v = steam kinematic viscosity. Based on the results of the SSWICS test series, the empirical constant C is ~ 5.5 for the case of debris solidification under the conditions in which gas sparging is absent.

In integrated analyses, water ingression-driven crust growth will proceed until ongoing concrete erosion reduces the dryout limit of the material in the melt zone below that which can support additional crust growth. (However, for sufficiently shallow melt depths, the possibility exists that the entire pool could be quenched before this point is reached). At this time, the crust will cease to grow. Thereafter, the crust will act as an interstitial heat transfer medium, with the upper portion of the material quenched and stabilized. A thin thermal boundary layer at the crust/melt interface will control the heat transfer from the melt zone to the overlying water pool. The possibility exists for additional water-ingression driven crust growth to occur later in the accident sequence as the decay heat level and concrete erosion rates decrease. Onset of this late phase cooling behavior is detected by tracking Eq. 5-9 during the course of the calculation.

5.3 Melt Eruptions

Once a stable crust forms, the second cooling mechanism that can contribute to debris stabilization is melt eruptions through cracks and fissures in the crust. In general, melt dispersal during eruptions is calculated by assuming that the melt entrainment rate is proportional to the gas volumetric flowrate times an entrainment coefficient; i.e.,[14]

$$j_m = K_e j_g \quad (5\text{-}12)$$

where j_m = superficial gas velocity of melt into the overlying water pool, and K_e = melt entrainment coefficient. The database review provided in the previous section indicates that the following correlation by Ricou and Spalding[39] provides a conservative estimate of the actual entrainment coefficient for the various tests in which eruptions were observed:

$$K_e = E\left(\frac{\rho_g}{\rho_m}\right)^{1/2} \quad (5\text{-}13)$$

where E *is* a proportionality constant which ranges from 0.06 to 0.12. Based on the data review, a mid-range value of E = 0.08 is recommended for analysis of melt eruption behavior during

core-concrete interaction for the case of limestone/common sand concrete. As noted in the review, no melt eruptions were observed for tests involving siliceous concrete. As is evident from Eq. 5-12, the entrainment rate is directly proportional to the melt sparging rate. Thus, the reduced gas content for this concrete type may have been a key contributor to the lack of eruptions. Moreover, test occurrences may have also contributed to the lack of eruptions.

Aside from providing estimates of the entrainment coefficients, the test data[15,31,33-35] also indicates that the erupted material is rapidly quenched in the form of a discrete layer that gradually accumulates over the crust. Given this rapid quenching, then the augmentation of the heat flux to the overlying water due to melt eruptions can be evaluated through the following equation:

$$q_e^{"} = j_m \rho_m \Delta e_{m,sat} \tag{5-14}$$

The test data[15,31,33-35] further indicates that the erupted material is rendered in the form of particle bed and lava-type structures with a high degree of porosity. Analysis of these structures[43] indicates that they have extremely high dryout limits (i.e., several MW/m^2) that are readily amendable to long-term cooling. Thus, the overall heat flux to the water as a result of melt solidification and quench and decay heat within the bed is evaluated from the equation:

$$q_b^{"} = j_m \rho_m \Delta e_{m,sat} + \chi_{UO_2}^b m_{bed}^{"} q_{dec} \tag{5-15}$$

where $\chi_{UO_2}^b$ = mass fraction fuel in the bed and $m_{bed}^{"}$ = particle bed mass per m^2 of crust surface area. Given the mass of the particle bed and the bed porosity, the height of the bed is evaluated through the expression,

$$H_b = \frac{m_{bed}^{"}}{\rho_{bed}(1-\varepsilon_{bed})} \tag{5-16}$$

Where ρ_{bed} = bed theoretical density and ε_{bed} = bed porosity. As is evident from Eq. 5-15, the particle bed is treated as a discrete region with time-dependent mass composition. The decay heat within the bed is then calculated based on the fission product inventory. Due to the high dryout limit of the bed, the decay heat is fully transferred to the overlying coolant, as opposed to the underlying concrete basemat.

5.4 Crust Breach

After a stable crust forms, the potential exists for the crust to bond to the reactor cavity walls. As observed in various reactor material tests,[31-35] an intervening gap can form between the melt and crust as the core-concrete interaction continues downwards if the crust has sufficient mechanical strength. Moreover, the water ingression and melt eruption cooling mechanisms are effectively deactivated once this gap forms, since the melt source that feeds these mechanisms is removed from the crust interface. Thus, another key program objective was to obtain crust strength data that could be used to validate the hypothesis that a plant-scale crust over a corium pool would be an unstable structure.

For a given cavity span, the minimum crust thickness required to be mechanically stable due to the combined weights of the overlying water pool, particle bed, and the crust itself is evaluated from the following first-order equation by Young and Budynas:[26]

$$\left(\rho_{cr}\delta_{\min}g + \rho_l H_w g + m''_{bed}g\right)A \geq C_{geom}\sigma_f \delta^2_{\min} \quad (5\text{-}17)$$

where δ_{min} = minimum crust thickness for mechanical stability, H_w = water depth over crust, A = basemat surface area covered by melt, C_{geom} = constant that is determined by the cavity geometry, crust edge boundary condition, and crust failure mode (e.g., C_{geom} = 2.53 for the case of brittle failure of a circular plate with simply supported edges[26]), and σ_f is the crust strength.

As discussed in Section 2.0, the SSWICS and CCI test results indicate that the mechanical strength of a corium crust quenched by an overlying water pool is in range of 1-3 MPa regardless of crust concrete content. Evaluation of Eq. 5-17 with this data indicates that a plant-scale crust would not be mechanically stable. Rather, it will most likely fail and reestablish contact with the melt. Therefore, for plant accident conditions, the continued contact between the melt and crust will allow water ingression and melt eruption cooling mechanisms to proceed and contribute to termination of the core-concrete interaction. This finding greatly simplifies the modeling of corium coolability at plant scale, since there is not a need to model the crust anchoring and gap formation process as the core-concrete interaction evolves. This is the principal finding of the crust strength measurements made as part of this program.

6.0 APPLICATION OF RESULTS TO PLANT SCALE

The previous sections of this report have summarized key results from the various test series conducted as part of the program (Table 1-1), and outlined a modeling methodology by which these results may be extrapolated to plant conditions (Table 5-1). The objective of this section is to utilize a simplified, but integrated, computational tool[12-13] that includes this modeling methodology to scope out the extent that core debris can be rendered coolable under the conditions of top flooding during an ex-vessel severe accident. To this end, the modeling approach is summarized first, followed by presentation of a few validation calculations that illustrate the predicative capability of the modeling tool. With this background in place, the model is then used to carry out a parametric set of calculations that define approximate coolability envelopes for the two concrete types that have been evaluated in the program.

6.1 Methodology

The simplified computational tool employed in the analysis that follows is CORQUENCH 2.0. This model is described in detail in References 12-13. A summary description follows.

The core-concrete interaction model is capable of performing either a 1-D or simplified 2-D ablation calculation (2-D geometry is assumed to be cylindrical, with axial and radial ablation calculated). The conservation of energy equation includes the following energy source/sink terms: i) decay heat, ii) chemical reactions between metallic melt constituents Zr, Cr, Fe, and Si (in sequence) and concrete decomposition gases H_2O and CO_2, iii) condensed phase chemical reactions between Zr and SiO_2, iv) downwards (and sidewards for 2-D case) heat transfer to concrete, including slag heat sink, and v) heat transfer to overlying atmosphere (wet or dry). The melt composition can range from fully metallic to fully oxidic; in all cases, the two phases are assumed to be well mixed (i.e., phase stratification is not modeled). The conservation of mass equations and thermophysical property subroutines consider most core and concrete metals and their corresponding oxides, so that a wide range of cases can be considered. Melt viscosity is calculated using the Andrade formula (see Nazare et al[44]) with a correction for SiO_2 as developed by Shaw.[45] Viscosity enhancement due to buildup of solids within the melt is calculated using the Ishii-Zuber model.[46] Melt void fraction, which is highly relevant in determining the location where the crust anchors to the test section sidewalls in experiments, can be evaluated from one of several different correlations; the one used in the calculations presented herein was developed by Brockmann et al.[47]

In terms of heat transfer at the melt/concrete interface, a transient concrete ablation/decomposition model based on integral thermal boundary layer theory is utilized.[48] The inclusion of a concrete decomposition model is considered to be important in the evaluation of long-term CCI phenomena involving debris coolability, since the downwards heat transfer rate to underlying concrete can fall to very low levels as the decay heat decreases and the debris is quenched. The heat transfer coefficient at the melt/concrete interface can be selected from a variety of options; Bradley's[49] modification to the bubble agitation heat transfer model of Kutateladze and Malenkov[50] is used in the calculations provided below.

At the melt upper surface, radiant heat transfer to overlying structure is calculated when the cavity is dry. When water is present, the modeling methodology outlined in Section 4.0 is utilized. The melt-side convective heat transfer coefficient can be selected from a variety of

models; the model of Kutateladze and Malenkov[50] is used in the calculations presented below. As part of this work, the water ingression model was upgraded to evaluate the crust dryout limit according to Eq. 5-11. The mechanical properties in this equation were evaluated using a volume weighting method based on the composition of these two regions at any given time.[24]

Although the crust strength data indicates that sustained crust anchoring to the cavity sidewalls does not affect plant analyses, effort was devoted to modeling this type of behavior in CORQUENCH so that the model could realistically be applied to integral effect tests in which this type of behavior was observed.[1,2] In particular, the crust thickness is compared with that predicted from the solution of Eq. 5-17. When the thickness exceeds δ_{min}, the crust is assumed to attach to the test section sidewalls with the upper surface elevation fixed at the location at the time of anchoring. Thereafter, the voided melt upper surface location is tracked relative to the crust location so that the onset of gap formation can be predicted. When a gap does form, debris quenching by the mechanisms of crust water ingression and melt eruptions is terminated, and there is a corresponding reduction in upwards heat transfer due to solidification (latent heat) processes. Moreover, a heat transfer resistance across the gap is introduced into the upwards heat balance, which causes a further reduction in upwards heat transfer. This methodology allows the prediction of the crust anchoring time/location in the integral effect tests,[1-2] as well as the subsequent gap formation process. These predictions can be compared with posttest examination results to gauge the accuracy of the model. Moreover, the model allows the prediction of the upwards heat flux both before and after separation, which can be compared with information logged during the tests. Thus, the model can be more rigorously validated against test data, which increases the confidence level when the model is used to extrapolate to plant conditions.

6.2 Model Validation

The model has been validated against a variety of reactor material integral effect tests conducted under both wet and dry cavity conditions.[12-13] In terms of dry cavity tests, the model was previously validated against ACE/MCCI tests L2, L4, L5, L6, and L8,[5-6] as well as the SURC-1 and SURC-2 tests conducted at SNL.[4,51] This validation matrix includes tests with four types of concrete, both BWR and PWR melt compositions, and cladding oxidation states ranging from 30 to 100 %. The interfacial heat transfer models were specified as described above for all test cases. The end-of-test ablation depth (including concrete/metal inserts for ACE/MCCI tests[5-6]) was predicted to within 25 % on average for all seven tests. The maximum deviation between the measured and predicted melt temperature over the course of the experiment averaged 8 %. These calculations provided a sense of the uncertainty involved in the application of the model to reactor material tests under dry cavity conditions.

In terms of tests conducted with water, the upgraded model has been applied to MACE tests M1b[34] and M3b[33] to check the selection of empirical constants and to gauge the overall predictive capability. The melt/water interfacial heat transfer models used in these calculations were described in Section 5.0. In both sets of calculations, the proportionality constant in the entrainment coefficient correlation (Eq. 5-13) was set equal to E=0.08, which is the value that was found to conservatively reproduce the melt eruption results for a variety of reactor material separate and integral effect tests (see Section 4.0). With the entrainment coefficient fixed, the empirical constant C in the crust dryout heat flux model (Eq. 5-11) was adjusted until calculated results reasonably agreed with the debris-water heat flux measured during the tests, as well as the

crust thickness and mass of erupted material found during posttest examinations for both tests. The results of this study indicate that the value C ~ 9.0 produced the best fit to the test results. For reference, the results of the SSWICS test series indicated that this constant should be set to ~ 5.5 for the case of debris solidification under the condition in which gas sparging is absent (see Section 2.0). The required increase in the empirical constant by ~ 60 % to match the integral effect test results could possibly be explained by the presence of the sparging concrete decomposition gases, which cause the level of interconnected porosity within the crust to increase above that formed during quench under inert (i.e., non-sparged) conditions.

Aside from the selection of empirical constants related to the melt eruption and water ingression cooling mechanisms, the failure stress utilized in the crust anchoring model (viz. Eq. 5-17) was set at 3.0 MPa, which is at the upper end of the range measured for the SSWICS and CCI crusts (see Figure 2-19). The decay heat input into the crust and particle bed regions was assumed to equal zero, and all heat input was assumed to be deposited in the melt. This modeling assumption is consistent with the DEH heating technique used in the MACE (and current CCI) test series. The particle bed formed due to melt eruptions was assumed to solidify with a porosity of 40 %.[13]

The melt temperature, ablation depth, and melt/water heat flux predictions are compared with the MACE Test M1b results in Figures 6-1 through 6-3, respectively, while the predicted debris distribution is shown

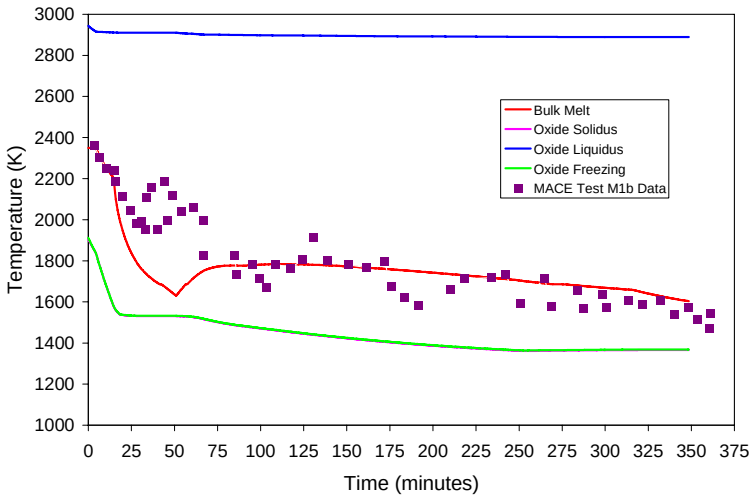

Figure 6-1. Melt Temperature Prediction for M1b.

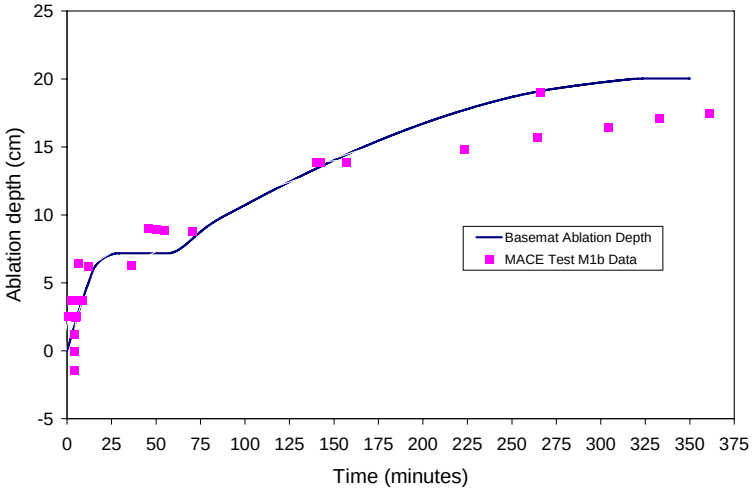

Figure 6-2. Axial Ablation Prediction for M1b.

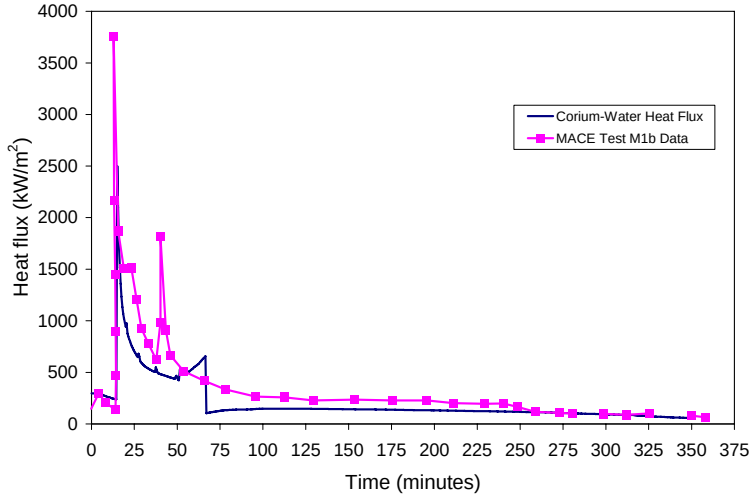

Figure 6-3. Melt-Water Heat Flux Prediction for M1b.

in Figure 6-4. In these figures, time zero corresponds to onset of ablation, and the cavity was flooded at 14.7 minutes relative to onset of ablation.

Examination of the figures indicates that the model reasonably reproduces the melt temperature, ablation, and melt/water heat transfer during the bulk cooling transient, which lasts until ~ 35 minutes. Following initial crust formation at 35 minutes, the upwards heat transfer is dominated by the water ingression and melt eruption cooling mechanisms, which effectively leads to the development of a quench front progressing downwards through the debris. Sustained crust growth occurs at the calculated dryout limit for the crust material which was ~ 500 kW/m^2 during this time interval, while the balance of the upwards heat transfer (i.e., up to 100 kW/m^2) is due to quench of melt droplets generated as a result of the melt eruption cooling mechanism. Note that the experimentally observed spike in the upwards heat transfer rate to a level of ~ 1.8 MW/m^2 at 40 minutes is due to a melt eruption event.[34] Thus, the model prediction of escalating heat flux due to eruptions at this time is at least qualitatively consistent with the overall phenomenology observed in the experiment.

As is evident from Figure 6-4, the melt/crust separation for this test is predicted to occur at ~ 54 minutes, which is in reasonable agreement with the estimated separation time of ~ 50 minutes.[34] As described previously, the empirical constant in the dryout heat flux model was specified such that the predicted crust thickness at the time of separation (5.3 cm) was in the 5-6 cm range measured during posttest

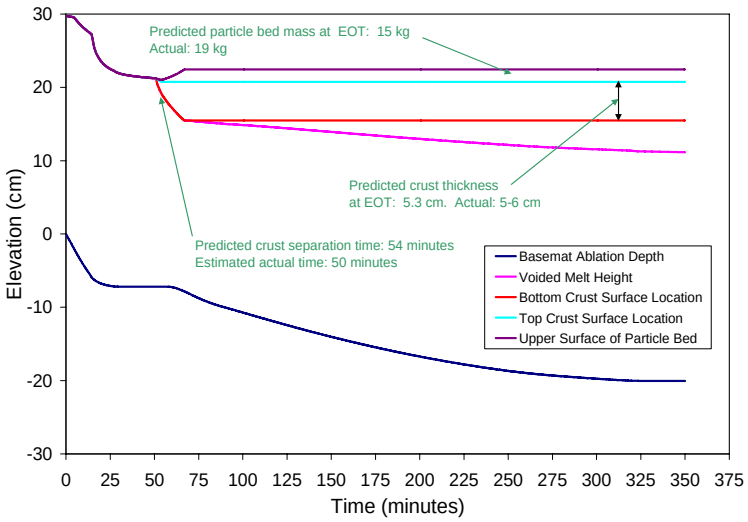

Figure 6-4. Debris Distribution Predictions for M1b.

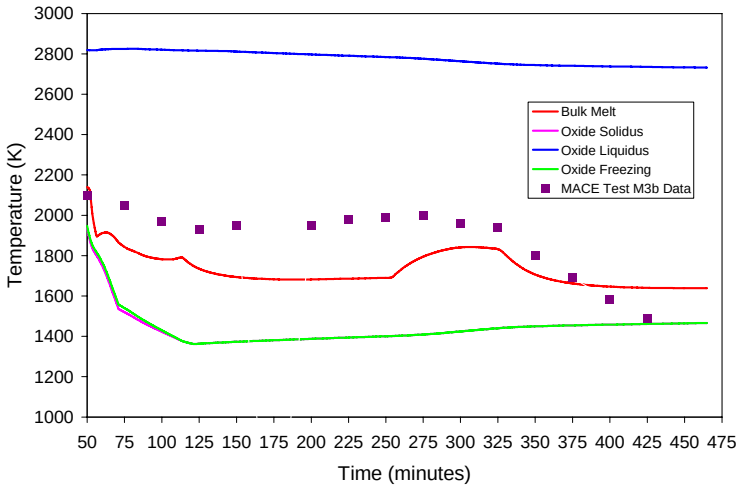

Figure 6-5. Melt Temperature Prediction for M3b.

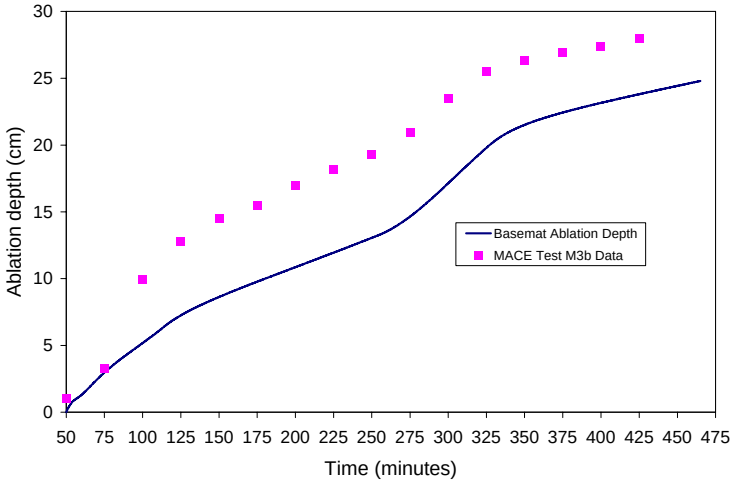

Figure 6-6. Axial Ablation Prediction for M3b.

examinations. Furthermore, the selection of the entrainment coefficient constant at K_e ~ 0.08 results in a reasonable prediction of ejected melt mass at the time of separation (i.e., 15 kg; see Figure 6-4) in comparison to the posttest measurement of 19 kg. Further examination of Figure 6-4 indicates that the upper crust anchored at an elevation of + 21 cm with respect to the initial concrete surface, which is in reasonable agreement with the actual +23 cm elevation location measured for the test.

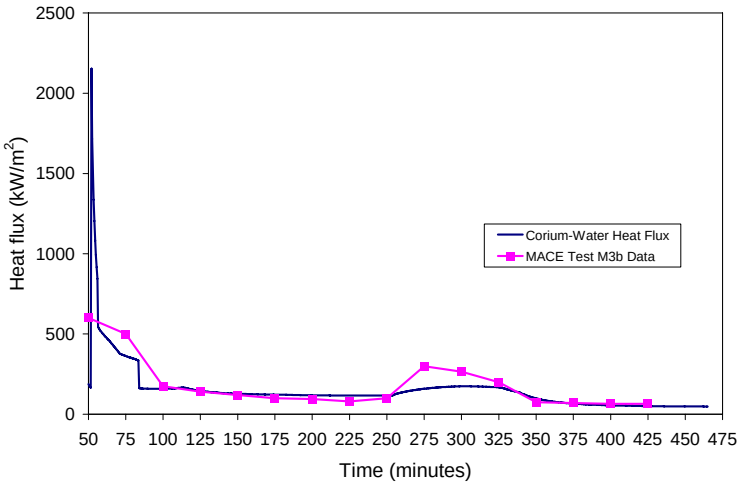

Figure 6-7. Melt-Water Heat Flux Prediction for M3b.

The analogous set of calculations are shown in Figures 6-5 through 6-8 for MACE Test M3b. These calculations were performed using identical modeling assumptions as those utilized for the Test M1b comparison. For this test, onset of sustained basemat ablation was delayed until ~50 minutes due to the formation of a stable insulating crust at the core-concrete interface; cavity flooding was essentially coincident with the onset ablation.

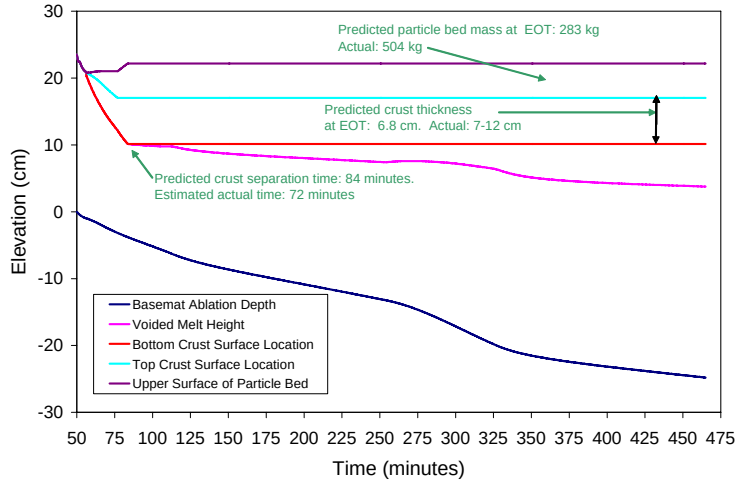

Figure 6-8. Debris Distribution Predictions for M3b.

As shown in the figures, the model generally underpredicts the melt temperature and ablation progression over the course of the experiment, while the debris/water heat flux prediction is in reasonable agreement. The bulk cooling transient was much shorter for this test, with incipient crust formation predicted to occur at ~ 56 minutes. Thereafter, a floating crust boundary condition was calculated until ~ 83 minutes, at which point the ~ 7 cm thick crust had achieved sufficient mechanical strength to bond to the test section sidewalls in the 120 cm x 120 cm test section. During this time interval, sustained crust growth occurs at the calculated dryout limit for the crust material which averaged ~ 400 kW/m^2, while the balance of the upwards heat transfer (i.e., up to 100 kW/m^2) is due to quench of melt droplets generated as a result of the melt eruption cooling mechanism. .

As is evident from Figure 6-8, crust separation for this test is predicted to occur at ~ 84 minutes, which is slightly longer than the estimated separation time of ~ 72 minutes.[33] The predicted crust thickness at the time of separation (6.8 cm) is at the lower end of the 7-12 cm measurement range determined during posttest examinations. Furthermore, the predicted particle bed mass of 283 kg is ~ 40 % less than the posttest measurement of 504 kg. A possible explanation for the underprediction of the mass of these two regions is that a power increase at ~

250 minutes during the test[33] caused the melt to recontact the bridge crust, resulting in additional debris cooling by the melt eruption and water ingression cooling mechanisms. As shown in Figure 6-8, the model does not predict sufficient pool voiding for the melt to recontact the crust during this stage, and therefore additional mass accumulation in these two regions is not possible according to the calculation.

To summarize, the incorporation of bulk cooling, water ingression, melt eruption, and crust anchoring models into a traditional core-concrete interaction modeling approach significantly improves the ability to reproduce the melt/water heat flux data for integral debris coolability tests. Furthermore, the incorporation of these models allows a realistic prediction of the posttest debris configuration, including ablation depth, timing/extent of gap formation, crust thickness, and the mass of the ejected material.

6.3 Plant Predictions

The objective of this section is to utilize the upgraded model[12-13] in order to scope out an approximate debris coolability envelope for the two concrete types that were evaluated as part of the program. One of the key challenges involved with this task was to define a general methodology that would illustrate the overall effect of cavity flooding on mitigating the accident sequence without making specific assumptions regarding accident progression, plant geometry, or the accident management procedure. For instance, initial melt depths can range considerably depending upon the melt mass and the containment floor area available for spreading. In addition, some accident management strategies call for early cavity flooding prior to pressure vessel breach, such that water will be present as an initial condition at the start of the core-concrete interaction. In other instances, dictated either by planning or by physical occurrences, water may be added at some point after the CCI has been initiated, or not at all. In cases involving delayed cavity flooding, the melt composition and temperature will have evolved according to a dry cavity erosion process, and test results described earlier in this report have clearly shown that melt composition has a strong influence on debris coolability.

Approach

With these challenges outlined, the following general approach was adopted for carrying out the parametric calculations. For a given concrete type, the initial collapsed melt depth (based on the core melt pour mass) was defined as the independent variable; parametric calculations were carried out for depths in the range of 15-40 cm. For a given initial depth, the concrete (slag) content at the time of cavity flooding was systematically varied over the range of 0-20 wt % in increments of 5 wt %. Thus, for cases involving concrete as an initial constituent, the actual melt depth at flooding was deeper than the initial depth based on the melt pour mass, reflecting the fact that slag had been introduced into the melt during the dry cavity erosion phase. Clearly, this approach increased the overall volume of melt to be quenched for a given concrete content, but more importantly, it maintained the decay heat level the same for all cases since the fission product inventory was fixed by the initial melt pool conditions.

For future reference, it is instructive to relate the incremental increase in the melt pool depth to the amount of concrete that has been incorporated into the melt. For a given concrete type and initial pool depth, the incremental change in height is given by the expression:

$$\Delta h_s = \frac{\chi_s \rho_m^o h_m^o}{\rho_s (1-\chi_s)} \tag{6-1}$$

where χ_s = weight fraction slag in melt, ρ_s = slag density, ρ_m^o = initial melt pool density (with χ_s = 0), and h_m^o = initial collapsed pool depth. Similarly, the basemat erosion depth at which a given slag content is achieved in the melt pool is given by:

$$\delta_c = \frac{\chi_s \rho_m^o h_m^o}{\rho_c (1-\chi_s)(1-\chi_g)} \tag{6-2}$$

where χ_g = weight fraction gas (H_2O and CO_2) in concrete, and ρ_c = concrete density.

With the melt pool composition defined in terms of the initial pool depth and the extent of ablation, the next requirements are to define the initial melt temperature and decay heat function. The initial temperature is determined by the overall course of the core-concrete interaction up to the point of cavity flooding, while the decay heat function is determined not only by the fission product inventory, but also by the elapsed time up to the point at which the cavity is flooded. For the purposes of this analysis, the initial melt temperature is set midway between the oxide phase liquidus and solidus temperatures computed by the model for the melt composition at the time of cavity flooding. In general, the time lapse in the evaluation of the decay heat function corresponds to the time required for the ablation depth to reach that given by Eq. 6-2 for the specified corium concrete content. This time interval is model (and sequence) dependent, and to simplify the current analysis, the core-concrete interaction is assumed to be flooded two hours after scram regardless of initial melt concrete content. Note that this assumption is conservative with respect to decay heat input to the melt for cases involving a significant initial concrete content.

In terms of general assumptions, the case of a PWR corium melt interacting with both LCS and siliceous concrete basemats is considered. The corium cladding content is taken to be fully oxidized at the time of cavity flooding. The corresponding melt composition is thus set at 80/20 wt % UO_2/ZrO_2. The concrete compositions are shown in Table 6-1, while the initial melt temperatures for the various compositions considered in the computational matrix are shown in Table 6-2.[a] The concrete compositions are noted to be similar to those utilized

Table 6-1. Chemical Composition of Concretes Assumed in the Analyses.

Oxide	Limestone-Common Sand	Siliceous
Al_2O_3	3.6	3.6
CaO	26.5	17.2
Fe_2O_3	1.6	1.5
MgO	9.7	0.9
K_20	0.6	0.8
SiO_2	28.8	61.3
Na_2O	1.1	0.7
TiO_2	0.2	0.2
CO_2	21.7	10.0
H_2O, Free	2.0	2.4
H_2O, Bound	4.2	1.4

[a] In the range of concrete contents up to 20 wt %, the model[13] property subroutines, which are based on the data of Roche et al.,[25] predict a fairly small (i.e., a few degree) difference in the solidus and liquidus temperatures for the two concrete types; these minor differences are neglected in the specification of the initial melt temperature.

in Tests CCI-2 and CCI-3, which were conducted with LCS and siliceous concrete types, respectively (see Section 3.0). The containment pressure is assumed to equal 4 Bar. Any limitations on water supply are neglected in this analysis, so that the quench process is not water starved. The decay heat curve is evaluated using the Revised American National Standard for a PWR at ~ 1000 days burnup.[52] The decay heat is assumed to be partitioned between the melt and crust zones depending upon the fuel mass present in each of these zones at any given time. As noted above, the pressure vessel is assumed to fail at two hours into the accident sequence. At this time, the decay heat level (neglecting volatiles) corresponds to ~ 300 W/kg fuel. To decouple the results from the details of any particular plant design, the calculations are performed using a 1-D modeling approach (i.e., strictly axial ablation). The interfacial heat transfer modeling assumptions and user input constants are identical to those used in the model validation calculations described above. In particular, the key assumptions related to the melt eruption and water ingression cooling mechanism models are the empirical constants E in Eq. 5-13 and C in Eq. 5-11. Consistent with the validation calculations, these constants are set equal to E = 0.08 and C = 9.0, respectively. The model is applied under the assumption that melt/crust contact is maintained over the course of the accident sequence, which is the expected plant condition based on the results of the crust strength data obtained as part of this work.

Table 6-2. Initial Melt Temperatures Employed in Analyses.

Corium Concrete Content (Wt %)	Oxide Phase Liquidus (K)	Oxide Phase Solidus (K)	Initial Melt Temperature (K)
0	2928	2850	2889
5	2923	2326	2624
10	2918	1877	2398
15	2913	1541	2227
20	2908	1471	2190

Limestone/Common Sand Concrete Results

The principal results of the parametric calculations for the case of Limestone-Common Sand (LCS) concrete are shown in Figure 6-9, which provides the total axial ablation depth at stabilization versus initial melt depth for various corium concrete contents. To aid in the interpretation of the results, the incremental time at which melt stabilization is achieved after dry cavity ablation is plotted in Figure 6-10, while the fraction of core material stabilized by the water ingression mechanism is shown in Figure 6-11. Finally, the basemat ablation depth to achieve an initial concrete content in the melt at the time of cavity flooding (i.e., Eq. 6-2) is shown in Figure 6-12 for the

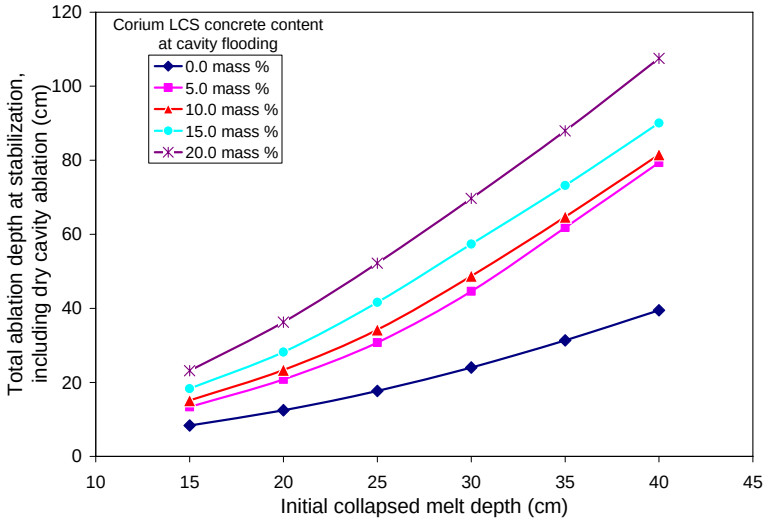

Figure 6-9. Maximum Basemat Ablation (LCS Concrete).

case of LCS concrete.[b] Note that the total ablation depth at stabilization shown in Figure 6-9 includes the initial depth incurred during dry cavity ablation (Figure 6-12), as well as the incremental ablation that accrues after flooding.

To illustrate the utility of Figure 6-12 in the interpretation of these results, consider the case of a 30 cm deep melt pool flooded when the melt concrete content reaches 10 wt %. From Figure 6-12, the ablation depth to achieve this concrete level is found as 15 cm. Assuming an average ablation rate of 5 cm/hour during the dry cavity ablation (model-dependent), then 3 hours would elapse between vessel breach and cavity flooding. From Eq. 6-1, the incremental change in melt depth after 15 cm of axial erosion is found as 10 cm. Thus, the total melt depth at the time of cavity flooding would be 40 cm.

Examination of Figure 6-9 indicates the expected result that the total ablation depth at stabilization increases systematically with the initial melt depth spread on the containment floor. For cases in which the initial concrete fraction is zero, basemat ablation is fairly limited, even for melt depths up to 40 cm, at which point peak ablation is predicted to reach ~ 40 cm. As shown in Figure 6-11, the fraction of corium solidified by the water ingression mechanism decreases relative to the melt eruption mechanism as initial depth increases. This is due to the fact that deeper melts require a longer time to cool (Figure 6-10), and more concrete slag is incorporated into the melt as the time progresses. As described in Section 2.0, the effectiveness of the water ingression mechanism decreases

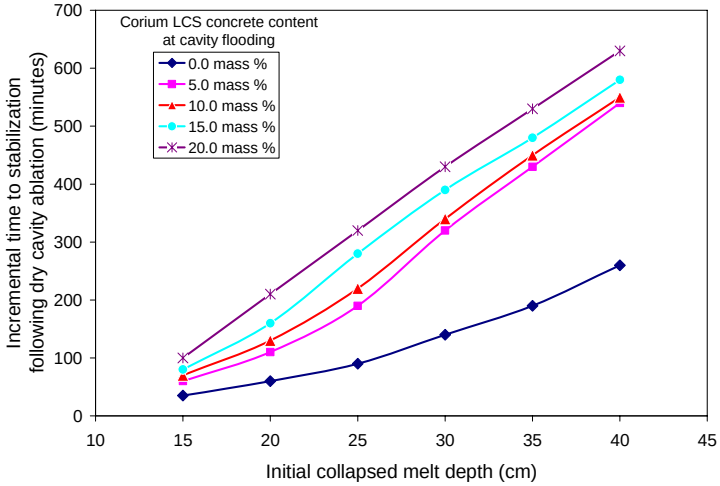

Figure 6-10. Incremental Time to Stabilization (LCS Concrete).

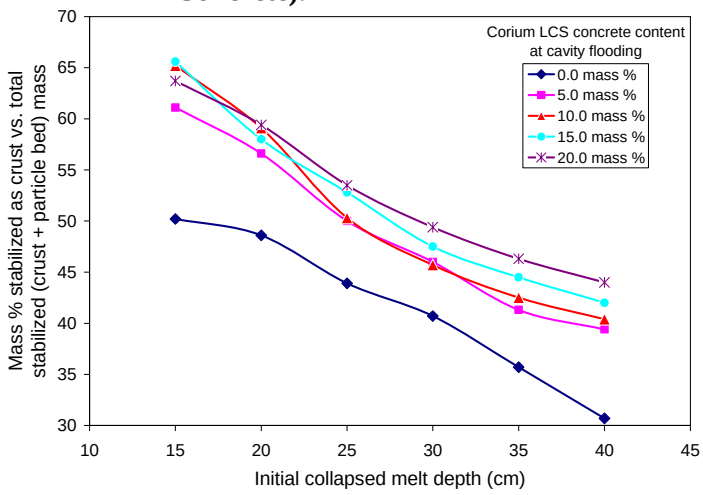

Figure 6-11. Relative Contribution of Cooling Mechanisms to Debris Stabilization (LCS Concrete).

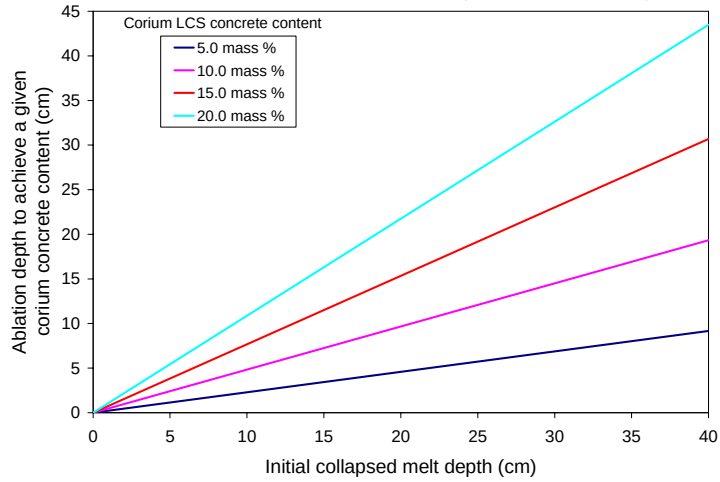

Figure 6-12. Ablation Depth to Achieve a Given Corium Concrete Content (LCS Concrete).

[b]The following property data (based on the model property subroutines) were employed in the evaluation of Eq. 6-2 for the case of LCS concrete: χ_g =0.279, ρ_m^o = 8000 kg/m^3, ρ_c = 2432 kg/m^3, and ρ_s = 2586 kg/m^3.

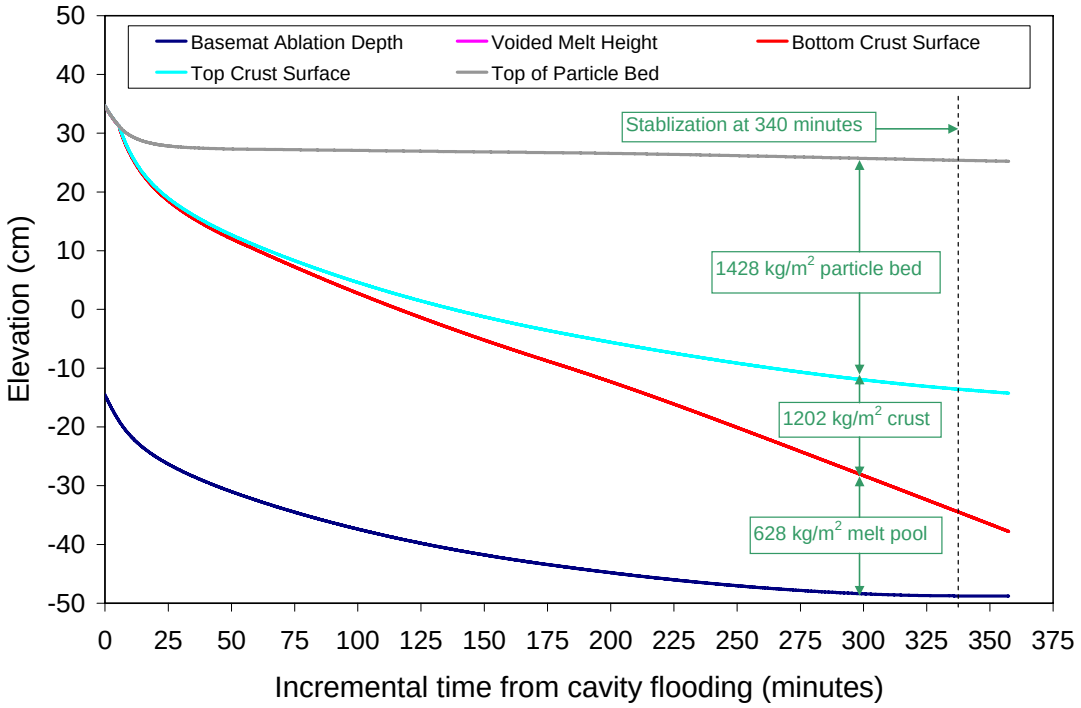

Figure 6-13. Debris Distribution Evolution for the Case of a 30 cm Initial Collapsed Melt Depth Containing 10 wt % Concrete.

as the corium concrete content increases (see Figures 2-14 and 2-15).

Additional examination of Figure 6-10 indicates that the ablation depth at stabilization increases systematically with initial concrete content for a given initial melt depth. This trend is also due to the reduced efficiency of the water ingression mechanism as concrete content increases. However, further examination of Figure 6-11 indicates the somewhat surprising trend that the overall contribution of the water ingression mechanism increases relative to the melt eruption mechanism as concrete content increases. The explanation for this trend becomes evident by examining a representative set of results for one of the cases considered as part of this study. These results are shown in Figure 6-13, which illustrates the overall evolution of the debris distribution for the previously mentioned case of an initial 30 cm melt depth containing 10 wt % concrete. As is evident, melt stabilization for this case is predicted to occur at 340 minutes, at which point the total ablation depth has reached 49 cm (34 cm of which is accrued after cavity flooding). Further examination of the figure indicates that water ingression does not begin to play a significant role in the overall cooling behavior until ~ 180 minutes into the transient. At this point, the overall reduction in the decay heat level, in conjunction with melt zone depletion by the eruption cooling mechanism, has reduced the decay heat in the remaining melt to the point that water ingression begins to contribute significantly to the overall debris cooling rate (i.e., Eq. 5-9 is satisfied). This results in an accelerated crust growth rate that is evident in Figure 6-13. In addition, the effectiveness of the melt eruption mechanism is diminished at this stage due to the reduced melt sparging rate. These combined affects cause the mass of material stabilized by water ingression cooling to increase rapidly, resulting in a significant overall contribution by the time basemat ablation is arrested. This late phase cooling behavior explains the trend of increased debris stabilization by water ingression cooling relative to melt eruptions as concrete content increases that is evident in Figure 6-11.

Note that the overall debris morphology shown in Figure 6-13 is typical of all cases calculated as part of this study. In particular, a porous particle bed (typically porosity is 40 %

based on MACE test results[33-34]) forms by the melt eruption mechanism over a porous crust that forms by the water ingression mechanism. Beneath the crust lies a shallow (in this case, 13 cm) melt pool that is highly diluted (i.e., 35 wt %) in concrete oxides. Melt stabilization occurs on the basis that the heat transfer rate to the underlying concrete is insufficient to sustain an ablation front (recall that a concrete dryout model is employed in this analysis). The residual heat transfer rate to the underlying concrete is typically ~ 4 kW/m^2 at stabilization; this heat is removed from the core-concrete interface by conduction into the remaining concrete basemat. After stabilization, the remaining melt is slowly cooled by water ingression until the material is completely frozen.

Siliceous Concrete Results

The principal results for the case of siliceous concrete are shown in Figure 6-14, which shows the total axial ablation depth at stabilization versus initial melt depth for various corium concrete contents. In addition, the incremental time to achieve stabilization after dry cavity ablation is shown in Figure 6-15, while the relative contribution of the various cooling mechanisms is shown in Figure 6-16. Finally, the basemat ablation depth to achieve an initial corium concrete content is shown in Figure 6-17 for the case of siliceous concrete.[c] The total ablation depth at stabilization is again noted to include both the initial depth incurred during the dry cavity ablation (Figure 6-17), as well as the incremental ablation that accrues after flooding.

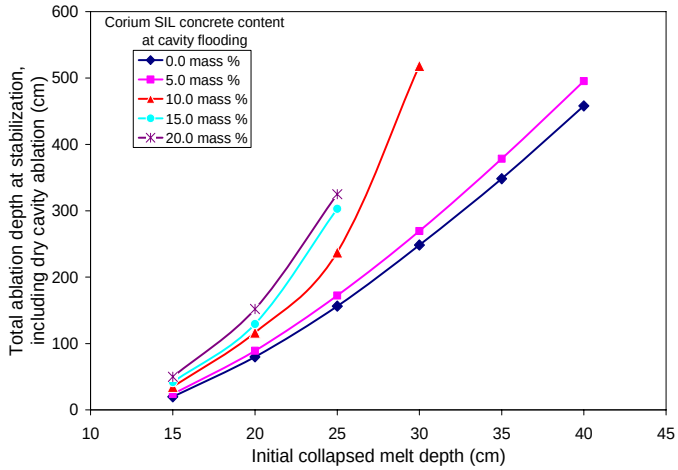

Figure 6-14. Maximum Basemat Ablation (Sil. Concrete).

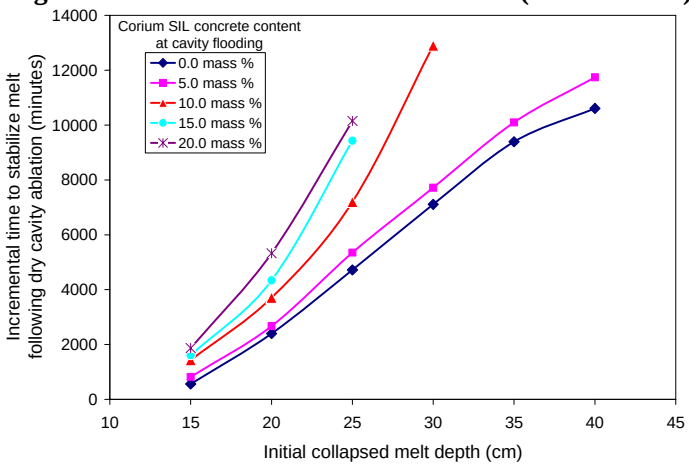

Figure 6-15. Incremental Time to Stabilization (Sil. Concrete).

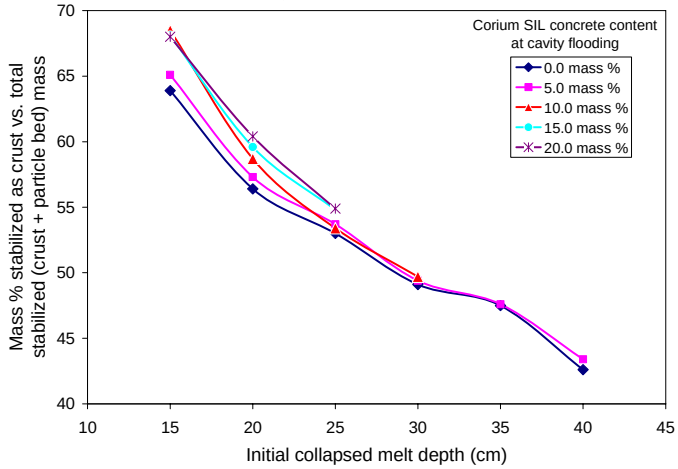

Figure 6-16. Relative Contribution of Cooling Mechanisms to Debris Stabilization (Sil. Concrete).

[c]The following property data were employed in the evaluation of Eq. 6-2 for the case of siliceous concrete: χ_g = 0.135, ρ_m^o = 8000 kg/m^3, ρ_c = 2217 kg/m^3, and ρ_s = 2295 kg/m^3.

Examination of Figure 6-14 indicates that the total ablation depth increases systematically with the initial melt depth. This same trend was found for the case of LCS concrete. However, comparison of Figures 6-9 and 6-14 indicates that the ablation depth at stabilization is much larger for case of siliceous concrete in comparison to the LCS type. This trend is principally due to the fact that siliceous concrete has much lower gas content than LCS concrete (i.e., ~ 50 % less; see Table 6-1), which reduces the effectiveness of the melt eruption cooling mechanism. In addition, the water ingression mechanism was found to be slightly less effective for melts containing siliceous concrete relative to those containing LCS (see Figures 2-14 and 2-15, and Eq. 5-11). As is evident by comparing Figures 6-11 and 6-16, the net effect on the overall behavior is that the water ingression mechanism plays a more important role in stabilizing the melt for siliceous concrete relative to LCS. However, it is clear from these results that basemat attack may be much more severe in plants constructed from siliceous concrete relative to those constructed from the LCS type.

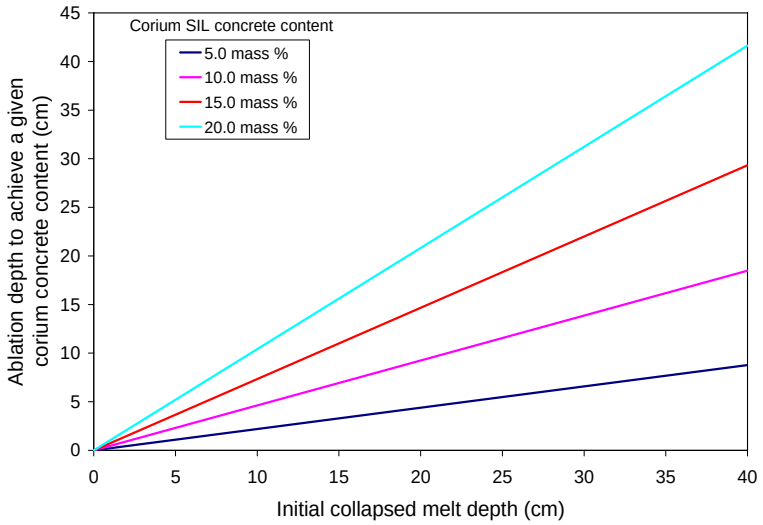

Figure 6-17. Ablation Depth to Achieve a Given Corium Concrete Content (Sil. Concrete).

For the siliceous concrete study, cases in which the calculated ablation depth significantly exceeded 5 m before stabilization was achieved were (somewhat arbitrarily) neglected in the presentation of the results. Examination of Figures 6-14 through 6-16 indicates that this includes the 35 and 40 cm melt depth cases when the initial concrete content was 10 wt %, and all cases above the 25 cm melt depth when the concrete content was in the range of 15 - 20 wt %.

Discussion

Definition of a coolability envelope based on these results is clearly a function of the concrete type, containment design, and the accident management strategy. However, for illustrative purposes, it is arbitrarily assumed that up to 1 meter of axial ablation can be accommodated while maintaining containment integrity, and that sufficient floor area is present to maintain the initial collapsed melt depth at or below 40 cm. Under these conditions, the results for LCS concrete (Figure 6-9) indicate that melt stabilization can be achieved as long as the cavity is flooded before the melt concrete content exceeds 15 wt %. As shown in Figure 6-12, up to 30 cm of dry cavity ablation can be accommodated before the concrete content reaches this level. However, if cavity flooding is delayed past this point, then melt stabilization cannot be assured. As shown in Figure 6-10, melt stabilization will take up to 10 hours to achieve after flooding is initiated.

Under a similar set of assumptions, the results for siliceous concrete indicate a much narrower coolability envelope. In particular, examination of Figure 6-14 indicates that the melt cannot be stabilized before incurring up to 1 meter of axial ablation unless the initial melt depth is fairly shallow (i.e., $\leq$ 20 cm), and the cavity is flooded before the melt concrete content exceeds 10 wt %. As shown in Figure 6-17, only ~ 10 cm of dry cavity ablation can be accommodated before the concrete content reaches this level in this melt depth range. Under these conditions, coolability may take up to 2 days to achieve (see Figure 6-15). Conversely, if the containment design is such that melt depths up to 40 cm may be encountered, then permanent melt stabilization cannot be achieved unless the containment design can accommodate up to 5 m of axial ablation, and only if the cavity is flooded early (i.e., concrete content $\leq$ 5 wt %). Under these conditions, melt stabilization will take in excess of a week to achieve.

In closing, it is important to highlight key assumptions that underlie the results presented above. These analyses have considered the case of a fully oxidized PWR core melt undergoing one-dimensional interaction with LCS and siliceous concrete types. In real plant analyses, a significant metal fraction may be present in the melt as an initial condition, and/or the fuel-cladding ratio in the melt may be different representing other reactor types (i.e., BWR). The calculations further assume that the containment is pressurized to 4 bar. Reduction in pressure will increase the efficiency of the melt eruption cooling mechanism, while decreasing the effectiveness of the water ingression mechanism. Moreover, the test data does not clearly demonstrate that melt eruptions are a viable cooling mechanism for the case of siliceous concrete.

The calculations further assume that sufficient water is present in containment so that the quench process is not water starved. In many plants, providing the necessary water flowrate to meet this criterion may be problematic. Finally, the calculations have focused on axial ablation as the key factor involved in maintaining containment integrity. In other instances, radial ablation with the potential for undermining key support structures, or penetration of access ways that can bypass containment, may be more important from a risk perspective. In any of these cases, models that have been validated against the type of data generated in this and other programs are required to extrapolate to plant-specific conditions.

7.0 SUMMARY AND CONCLUSIONS

The purpose of the OECD/MCCI Program was to carry out reactor materials experiments and associated analysis to achieve the following two technical objectives: 1) resolve the ex-vessel debris coolability issue by providing both confirmatory evidence and test data for coolability mechanisms identified in previous integral effect tests, and 2) address remaining uncertainties related to long-term 2-D core-concrete interaction under both wet and dry cavity conditions. This report has summarized the results of eleven reactor material tests that were carried out to achieve these objectives.

In terms of the ex-vessel debris coolability issue, two types of separate effects tests were conducted to provide data on key melt coolability mechanisms that could provide a pathway for achieving long-term debris cooling and stabilization. The results of these tests provided both confirmatory evidence and test data to support the development and validation of models that form the technical basis for extrapolating to plant conditions. In particular, the Small Scale Water Ingression and Crust Strength (SSWICS) tests[10-11] provided data on the ability of water to ingress into core material, thereby augmenting the otherwise conduction-limited heat transfer process. Dryout heat flux data obtained from these experiments can be used directly in existing models for evaluating the effect of water ingression on mitigation of ex-vessel accident sequences involving core-concrete interaction.[12-13] The crust strength data obtained as part of this work can be used to verify the concept[11] of sustained melt/crust contact due to crust instability in the typical 5-6 m cavity span of most power plants.

The Melt Eruption Test (MET) focused on providing data on the melt entrainment coefficient under well-controlled experimental conditions. In particular, the experiment featured an inert basemat with remotely controlled gas sparging, since this is the most important parameter in determining the entrainment rate.[14] Entrainment rate data obtained from this and other tests can be used directly in existing models[13-14] for evaluating the effect of melt ejection on mitigation of the core-concrete interaction.

In terms of 2-D core-concrete interaction, there is significant uncertainty regarding the lateral vs. axial power split,[3] which is principally due to a lack of experimental data to adequately qualify the computer codes insofar as long-term behavior is concerned. To help bridge this data gap, the approach was to conduct integral effect Core Concrete Interaction (CCI) tests that replicate as close as possible the conditions at plant scale, thereby providing a database that can be used to verify and validate the codes directly. To augment the amount of information gathered from these tests, the experiments[15] were flooded from above after a pre-defined concrete ablation depth was reached to provide debris coolability data under conditions involving late phase flooding. The input power levels for the tests were selected so that the heat fluxes from the melt to concrete surfaces and the upper atmosphere were initially in the range of that expected early in the accident sequence (i.e., 150-200 kW/m^2).

The specific findings from the separate effect tests conducted to investigate individual coolability mechanisms are summarized as follows:

1. The SSWICS test results indicate that water is able to ingress into core material during quench, thereby augmenting the otherwise conduction-limited heat transfer rate. The effectiveness of this mechanism was found to decrease with increasing corium concrete content, but was not sensitive to concrete type. The data did not show a significant effect of system pressure on the cooling rate, which contrasts with particle bed dryout models that are based on the concept of a counter-current flow limitation.

2. The SSWICS dryout heat flux data was used to empirically adjust and validate the Lister/Epstein dryout heat flux model for direct application to plant accident sequences. As part of this work, a simple expression for the crust cracking temperature was developed on the basis of the crust mechanical properties. This definition, in conjunction with the adjustment of a single empirical constant, allows the dryout limit to be evaluated for a wide range of compositions based on the corium and coolant thermophysical properties alone.

3. The SSWICS crust strength measurements demonstrated that the actual mechanical strength of core material quenched by an overlying water pool is far weaker (by as much as two orders of magnitude) than that estimated for solid corium. This indicates that the crack structure formed during quench, not the composition, is the main determinant of crust strength. Moreover, extrapolation of the data indicates that a plant-scale crust would not be mechanically stable. Rather, it will most likely fail and reestablish contact with the melt. Therefore, for plant accident conditions, the continued contact between the melt and crust will allow water ingression and melt eruption cooling mechanisms to proceed and contribute to termination of the core-concrete interaction.

4. In terms of the MET investigation of the melt eruption cooling mechanism, the reactor material database was reviewed to provide a technical basis for model development and validation activities. This review indicated that the database includes both siliceous and limestone/common sand concrete types. Melt eruption data was obtained for all tests (both integral and separate effect) conducted with limestone/common sand concrete. The melt entrainment coefficients ranged from 0.06 to 0.25 %; the melts contained from 8 to 60 wt % LCS concrete. The entrainment data obtained as part of the CCI-2 experiment was particularly important since the eruptions occurred while the crust was floating and the input power was decreasing, so that the melt zone was not over-powered during the eruption process.[15] Thus, the entrainment coefficient estimate for this test is believed to be representative of prototypic conditions.

5. The MET database review further indicated that no spontaneous eruptions occurred after cavity flooding for the three tests conducted with siliceous concrete. As discussed by Bonnet and Seiler[14], the gas sparging rate during core-concrete interaction is the key parameter influencing the melt entrainment process. Thus, the reduced gas content for this concrete type may have been a key contributor to the lack of eruptions for these three tests. This review also indicated that test occurrences (i.e., crust anchoring and early termination of power input) may have precluded eruptions from occurring in the tests with this concrete type.

The CCI tests featured late phase flooding to provide coolability data after ablation had proceeded for some time. In terms of phenomenology, the tests provided data on the bulk cooling, water ingression, melt eruption, and transient crust breach cooling mechanisms. In addition, Test CCI-2 provided data on water ingress at the interface between the core material and concrete sidewalls. This mechanism had been previously identified in the COTELS reactor material test series.[11] Principal findings from these tests related to debris coolability are summarized as follows:

1. The heat flux during the first five minutes following cavity flooding was high for all tests. For the two tests conducted with siliceous concrete, the initial heat fluxes were close to the Critical Heat Flux (CHF) limitation of ~ 1 MW/m^2 under saturated boiling conditions. Thus, the heat fluxes were indicative of quenching of the upper surface crust that was present as an initial condition for both tests. However, for test CCI-2, the upper surface was essentially devoid of a surface crust when water was introduced. Thus, water was able to directly contact the melt, resulting in a bulk cooling transient in which the initial cooling rate approached 3 MW/m^2. The heat flux eventually fell below 1 MW/m^2 after ~ 5 minutes. At this time, a stable crust most likely formed at the melt-water interface, thereby terminating the bulk cooling transient.

2. The tests did not generally exhibit a pronounced decrease in overall melt temperature after cavity flooding. This is despite the fact that the heat flux and power supply responses both indicated substantial debris cooling. This type of behavior can be rationalized by a latent heat transfer process in which a quench front develops at the melt/water interface, as opposed to a sensible heat transfer process in which the entire melt mass is cooled by convective heat transfer with the heat dissipated to the overlying water by conduction across a thin crust at the melt/water interface. The posttest debris morphologies were also consistent with development of quenched debris zones, as opposed to bulk cooldown of the entire melt mass by conduction-limited cooling across a thin crust.

3. After the initial transient, the debris/water heat fluxes ranged from 250 to 650 kW/m^2. Heat fluxes for both siliceous concrete tests were lower than the test conducted with LCS concrete. In general, the data indicates that the heat flux increases with concrete gas content. The heat fluxes realized in the tests were several times higher than that predicted by the SSWICS water ingression correlation. Thus, the data suggests that the degree of interconnected cracks/fissures/porosity that form the pathway for water to ingress into solidifying core material is increased by the presence of gas sparging, particularly for the case in which the melt contains a high concrete fraction (e.g., > 15 wt %).

4. Aside from the water ingression mechanism, these tests also provided integral data on the melt eruption cooling mechanism. As noted earlier, significant eruptions were observed for Test CCI-2. However, no spontaneous eruptions were observed after cavity flooding for the two tests conducted with siliceous concrete. The melt entrainment coefficient for CCI-2 was ~ 0.11 %, which is in the range of that required to stabilize a core-concrete interaction over a fairly significant range of melt depths.

5. In terms of the crust breach cooling mechanism, both siliceous concrete tests provided data on *in-situ* crust strength, while Test CCI-1 also provided data on the extent of cooling after crust breach. The crust strength data indicates that crust material formed during quench is very weak. This finding is consistent with the previously described SSWICS test series crust strength measurements. However, the CCI measurements were significant because they were carried out under prototypic temperature boundary conditions before the material had cooled to room temperature.

6. Aside from the strength measurements, the crust breach event in CCI-3 caused a significant transient increase in the debris cooling rate. In particular, a large melt eruption occurred, resulting in a transient cooling event in which the peak heat flux

exceeded 3 MW/m^2. After the breach, the heat flux from the debris upper surface steadily declined over the next five minutes to a plateau in the range of 250-300 kW/m^2, which is similar to the plateau observed prior to the breach event. In general, the data obtained from this procedure indicates that breach events may lead to significant transient increases in the debris cooling rate at plant scale.

Principal findings from the CCI tests that were focused on providing data on two-dimensional cavity erosion behavior are summarized as follows:

1. All tests showed the overall trend of decreasing melt temperature as ablation progressed, which was due to a heat sink effect as relatively cool concrete slag was introduced into the melt, as well as the increasing heat transfer surface area as the melts expanded into the concrete crucibles. The reduction in melt temperature may have further reflected the evolution of the pool boundary freezing temperature that decreased as additional concrete was eroded into the melt over the course of the tests.

2. Tests CCI-1 and CCI-2 showed evidence of initial crust formation on the concrete basemat and sidewalls that resulted in an incubation period in which the ablation rates were very low and the melt temperature was relatively stable. Test CCI-3 also showed evidence of initial crust formation on the concrete basemat, but there was no evidence of sidewall crust formation for this test. In all cases, the crusts eventually failed, thereby allowing ablation to proceed. The duration of the incubation period for CCI-1 and CCI-2 appeared to be inversely proportional to concrete gas content, which suggests that crust failure may be driven in part by the mechanical forces that arise from the production of concrete decomposition gases at the core-concrete interface.

3. Long-term ablation behavior was found to be closely linked to concrete type. Lateral and axial ablation rates for the LCS concrete test were virtually indistinguishable; the concrete erosion rate averaged 4 cm/hr over several hours of interaction before gradually decreasing. The corresponding surface heat flux was ~ 60 kW/m^2. Thus, the lateral/axial heat flux ratio for this concrete type was ~ 1.

4. The relatively uniform power split for CCI-2 can be contrasted with the results of the two tests conducted with siliceous concrete. For test CCI-1, the ablation was highly non-uniform, with most of the ablation concentrated in the North sidewall of the apparatus. Crust stability may have played a major role in determining the ablation progression for this experiment; i.e., the data suggests that after the crust failed on the North concrete sidewall, the input power was predominately dissipated through ablation of this sidewall, while crusts continued to protect the basemat and south sidewall surfaces during the balance of the interaction.

5. In contrast to Test CCI-1, Test CCI-3 exhibited fairly symmetrical behavior insofar as the progression of lateral ablation is concerned. However, unlike Test CCI-2, the lateral ablation was highly pronounced in comparison to axial ablation. In this regard, the results of tests CCI-1 and CCI-3 are consistent. Lateral ablation in CCI-3 averaged 10 cm/hr over the last hour of the experiment, while the axial ablation rate was limited to 2.5 cm/hr over the same time interval. The corresponding heat fluxes in the lateral and axial directions were 100 and 25 kW/m^2, respectively. On this basis, the lateral/axial surface heat flux ratio for test CCI-3 was estimated as ~ 4, which is significantly higher than the near-unity ratio deduced for test CCI-2 with LCS concrete.

6. Between the two concrete types, possible explanations for differences in the erosion behavior are chemical composition and concrete gas content. A third possible explanation was revealed during posttest examinations. In particular, the core-concrete interface for the siliceous concrete tests consisted of a region where the core oxide had locally displaced the cement that bonded the aggregate. Conversely, the ablation front for the LCS test consisted of a powdery interface in which the core and concrete oxides were clearly separated. Variations in the interface characteristics may have influenced the ablation behavior for the two concrete types.

7. In terms of the chemical analysis results obtained as part of the test series, the corium in the central region of the test section was found to have a higher concentration of core oxides in comparison to that adjacent to the two ablating concrete sidewalls for all tests. Conversely, core oxides were found to be slightly concentrated near the concrete basemat in comparison to that found in the bulk of the corium. For both siliceous concrete tests, two zones appeared to be present: a heavy monolithic oxide phase immediately over the basemat that was enriched in core oxides, with a second overlying light oxide phase that was enriched in concrete oxides. The overlying oxide phase was porous and appeared to have been quenched after the cavity was flooded. This well-defined phase distribution can be contrasted with the debris morphology for CCI-2. In this test, the debris was highly porous and fragmented over the entire axial extent of the material remaining over the basemat. This open structure is consistent with the high degree of debris cooling that occurred after cavity flooding.

In terms of the applicability to plant conditions, these tests have provided information that will contribute to the database for reducing modeling uncertainties related to two-dimensional molten core-concrete interaction under both wet and dry cavity conditions. Furthermore, the tests have provided additional confirmatory evidence and test data for coolability mechanisms identified in earlier integral effect tests. Data from this and other test series thus forms the technical basis for developing and validating models of the various cavity erosion and debris cooling mechanisms. These models can then be deployed in integral codes that are able to link the interrelated phenomenological effects, thereby forming the technical basis for extrapolating the results to plant conditions.

One such model was upgraded to include the experimental findings related to debris coolability, and the model was used to scope out an approximate debris coolability envelope for the two concrete types that were evaluated as part of the program. The results for LCS concrete indicate that melt stabilization may be achievable in under one meter of axial ablation as long as the cavity is flooded before the melt concrete content exceeds 15 wt % for initial melt depths ranging up to 40 cm. Under these conditions, stabilization may take up to 10 hours to achieve. However, if flooding is delayed past this point, then the possibility of stabilizing the melt becomes much less likely.

Under the same set of modeling assumptions, the results for siliceous concrete indicate a much narrower coolability envelope. In particular, the results indicate that melt stabilization may not be achieved in under one meter of axial ablation unless the initial melt depth is fairly shallow (i.e., $\leq$ 20 cm), and the cavity is flooded before the melt concrete content exceeds 10 wt %. In this range, coolability may take up to two days to achieve assuming that melt eruptions are active during the quenching process. However, note that spontaneous eruptions have not been observed with water present in experiments conducted to date with this concrete type. Conversely, if the containment design is such that melt depths of up to 40 cm may be

encountered, then stabilization may not be achieved unless the design can accommodate up to five meters of axial ablation, and only if the cavity is flooded early (i.e., concrete content $\leq$ 5 wt %). Under these conditions, stabilization will take in excess of one week to achieve. Note again that this result is based on the assumption that melt eruptions are active for the case of siliceous concrete, which has not been experimentally observed.

In summary, the tests carried out as part of this particular program have examined core-concrete interaction and debris coolability for the case of fully oxidized core melts. As a whole, the results of the two-dimensional CCI tests have indicated trends in the ablation front progression that cannot be explained on the basis of our current understanding of the phenomenology involved with this type of physical process. These trends need to be understood before the results can be extrapolated to plant scale. Furthermore, in real plant accident sequences, a significant melt metal fraction could be present that may result in a stratified pool configuration. This type of pool structure was not evaluated in the program. Thus, additional analysis and testing may be required with melts containing a significant metal fraction to further reduce phenomenological uncertainties related to core-concrete interaction, and to evaluate the effects of melt metal content on debris coolability.

8.0 REFERENCES

1. M. T. Farmer, B. W. Spencer, D. J. Kilsdonk, and R. W. Aeschlimann, "Results of MACE Corium Coolability Experiments M0 and M1b," Proc. 8th Int. Conf. on Nucl. Eng., ICONE-8175, April 2-6, 2000.

2. M. T. Farmer, B. W. Spencer, J. L. Binder, and D. J. Hill, "Status and Future Direction of the Melt Attack and Coolability Experiments (MACE) Program at Argonne National Laboratory," Proc. 9th Int. Conf. on Nucl. Eng., ICONE-9697, April 8-12, 2001.

3. J. J. Foit, "Modeling of Oxidic Molten Core-Concrete Interaction in WECHSL," Nucl. Eng. and Design, Vol. 170, p. 73-79, 1999.

4. E. R. Copus et al, "Core-Concrete Interactions Using Molten UO_2 with Zirconium on a Basaltic Basemat : the SURC-2 Experiment," NUREG/CR-5564, 1990.

5. D. H. Thompson, et al., "Thermal-hydraulic Aspects of the Large-Scale Integral MCCI Tests in the ACE program," Proc. 2nd OECD (NEA) CSNI Specialist Meeting on Molten Core Debris-Concrete Interaction, Karlsruhe, Germany, April 1992.

6. D. H. Thompson, et al., "ACE Phase C Final Report: Volume I – MCCI Thermalhydraulic Results," ACE-TR-C42 Volume I, September, 1997.

7. J. K. Fink et al., "Aerosol and Melt Chemistry in the ACE Molten Core-Concrete Interaction Experiments," High Temperature and Materials Science, Vol. 33, pp. 51-75, 1995.

8. H. Nagasaka, "COTELS Project (3): Ex-Vessel Debris Cooling Tests," 2nd OECD (NEA) CSNI Specialist Meeting on Molten Core Debris-Concrete Interaction, Karlsruhe, Germany, April 1992.

9. H. Alsmeyer, "BETA Experiments on Zirconium Oxidation and Aerosol Release During Molten Corium/Concrete Interaction," Proc. 2nd OECD (NEA) CSNI Specialist Meeting on Molten Core Debris-Concrete Interaction, Karlsruhe, Germany, April, 1992.

10. S. Lomperski, M. T. Farmer, D.J. Kilsdonk, and R. W. Aeschlimann, "Small-Scale Water Ingression and Crust Strength Tests (SSWICS) SSWICS Final Report: Thermal Hydraulic Results," OECD/MCCI-2005-TR03, June 2005.

11. S. Lomperski, M. T. Farmer, D. J. Kilsdonk, and R. W. Aeschlimann, "Project Small-Scale Water Ingression and Crust Strength Tests (SSWICS) SSWICS Final Report: Crust Strength Measurements," OECD/MCCI-2005-TR02, June 2005.

12. M. T. Farmer and B. W. Spencer, "Status of the CORQUENCH Model for Calculation of Ex-Vessel Corium Coolability by an Overlying Water Layer," OECD (NEA) CSNI Workshop on Ex-Vessel Debris Coolability, Karlsruhe, Germany, November 15-18, 1999.

13. M. T. Farmer, "Modeling of Ex-Vessel Corium Coolability with the CORQUENCH Code," Proc. 9th Int. Conf. on Nucl. Eng., ICONE-9696, April 8-12, 2001.

14. J. M. Bonnet and J. M. Seiler, "Coolability of Corium Spread Onto Concrete Under Water, the PERCOLA Model," 2nd OECD (NEA) CSNI Specialist Meeting on Molten Core Debris-Concrete Interaction, Karlsruhe, Germany, April, 1992.

15. M. T. Farmer, S. Lomperski, D. J. Kilsdonk, and R. W. Aeschlimann, "OECD MCCI Project 2-D Core Concrete Interaction (CCI) Tests: Final Report," OECD/MCCI-2005-TR05, February 28, 2006.

16. M. T. Farmer, S. Lomperski, and S. Basu, "Results of Reactor Materials Experiments Investigating 2-D Core-Concrete Interaction and Debris Coolability," Proc. ICAPP '04, Pittsburgh, PA, June 13-17, 2004.

17. M. T. Farmer, S. Lomperski, and S. Basu, "The Results of the CCI-2 Reactor Material Experiment Investigating 2-D Core-Concrete Interaction and Debris Coolability," 11th International Topical Meeting on Nuclear Reactor Thermal-Hydraulics (NURETH-11), Avignon, France, October 2-6, 2005.

18. M. T. Farmer, S. Lomperski, and S. Basu, "Status of the Melt Coolability and Concrete Interaction (MCCI) Program at Argonne National Laboratory," Proc. ICAPP '05, Seoul, Korea, May 15-19, 2005.

19. M. T. Farmer, S. Lomperski, and S. Basu, "The Results of the CCI-3 Reactor Material Experiment Investigating 2-D Core-Concrete Interaction and Debris Coolability," Proc. ICAPP '06, Reno, Nevada, June 6-8, 2006.

20. S. Lomperski, M. T. Farmer, and S. Basu, "Experimental Investigation of Corium Quenching at Elevated Pressure," Accepted for Publication in Nucl. Eng. and Design, December, 2003.

21. S. Jones et al., "Dryout Heat Fluxes in Particle Beds Heated Through the Base," J. Heat Transfer, Vol. 106, pp. 176-183, 1983.

22. C. R. B. Lister, "On the Penetration of Water into Hot Rock," Geophys. J. R. Astr. Soc., Vol. 39, pp. 465-509, 1974.

23. M. Epstein, "Review of Water Ingression Models," ACEX-TR-C31, March 2000.

24. M. T. Farmer, J. J. Sienicki, and A. Kovtonyuk, "OECD MCCI Analytical Support (Stand Alone Task): Water Ingression Modeling of the OECD/MCCI SSWICS Tests," NRC/MCCI/2003-TR01, October 15, 2003.

25. M. F. Roche, et al., "Solidus and Liquidus Temperatures of Core-Concrete Mixtures," U.S. Nuclear Regulatory Commission Report NUREG/CR-6032, 1993.

26. W. C. Young and R. G. Budynas, Roark's Formulas for Stress and Strain, 7th Ed., McGraw-Hill Book Company, New York, NY, 2002.

27. J. J. Sienicki and B. W. Spencer, "The Jet Impingement Stage of Molten Core-Concrete Interactions," OECD CSNI Specialist Meeting on Core Debris/Concrete Interactions, Electric Power Research Institute, Palo Alto, CA, September 3-5, 1986.

28. M. T. Farmer et al., "Results of MACE Test M1b Posttest Debris Property Measurements," EPRI/ACEX-TR-C23, February, 1998.

29. M. T. Farmer, "Review and Assessment of the Melt Eruption Database," Presentation at the 7th OECD-MCCI Program Review Meeting, Consejo Seguridad Nuclear, Madrid, Spain, 6-8 April, 2005.

30. M. T. Farmer, S. Lomperski, D. J. Kilsdonk, and R. W. Aeschlimann, "Melt Eruption Test (MET) Design Report," Rev. 1, OECD/MCCI-2002-TR03, October 12, 2002.

31. M. T. Farmer, D. J. Kilsdonk, and R. W. Aeschlimann, "MSET-1 Test Data Report," EPRI/MACE-TR-D18, January, 2002.

32. M. T. Farmer, B. W. Spencer, D. R. Armstrong, D. J. Kilsdonk, and R. W. Aeschlimann, "MACE Test M4 Data Report," EPRI/MACE-TR-D15, August, 1999.

33. M. T. Farmer et al., "MACE Test M3b Data Report - Vols. I-II," EPRI/ MACE-TR-D13, April 1997.

34. M. T. Farmer, B. W. Spencer and D. R. Armstrong, "MACE Test M1b Data Report," EPRI/MACE-TR-D06, September 1992.

35. B. W. Spencer, M. Fischer, M. T. Farmer and D. R. Armstrong, "MACE Scoping Test Data Report," EPRI/MACE-TR-D03, June 1991.

36. B. Tourniaire, J. M. Seiler, J. M. Bonnet, and M. Amblard, "Liquid Ejection Through Orifices by Sparging Gas – The PERCOLA Program," Proc. 10th Int. Conf. on Nucl. Eng., ICONE-22431, April 2-6, 2000.

37. B. Tourniaire and J. M. Seiler, "Modeling of Viscous and Inviscid Fluid Ejection Through Orifices by Sparging Gas," Proc. ICAPP '04, Pittsburgh, PA, June 13-17, 2004.

38. F. B. Cheung and M. Epstein "Two-Phase Bubble-Liquid Boundary Layer Flow along Vertical and Inclined Surfaces," Nucl. Eng. and Design, Vol. 99, pp. 93-100, 1987.

39. F. B. Ricou and D. B. Spalding, "Measurements of Entrainment of Axisymmetrical Turbulent Jets," J. Fluid Mechanics, Vol. 11, pp. 21-32, 1961.

40. M. T. Farmer, J. P. Schneider, B. Bonomo, G. Theofanous and B. W. Spencer, "Modeling and Database for Melt-Water Interfacial Heat Transfer," 2nd CSNI Specialist Meeting on Core Debris-Concrete Interactions, Karlsruhe, Germany, April 1-3, 1992.

41. M. T. Farmer et al., "CORQUENCH: A Model for Gas Sparging-Enhanced, Melt-Water, Film Boiling Heat Transfer," ANS Winter Meeting Session on Thermal Hydraulics of Severe Accidents, Washington, DC, November 11-15, 1990.

42. G. B. Wallis, One-Dimensional Two-Phase Flow, McGraw-Hill Book Co., New York, NY, 1969.

43. M. T. Farmer et al., "Results of MACE Test M3b Posttest Debris Characterization," EPRI/ACEX-TR-C32, January, 2000.

44. G. Nazare, G. Ondracek, and B. Schulz, "Properties of Light Water Reactor Core Melts," Nucl. Tech. Vol. 32, pp. 239-255, 1977.

45. H. R. Shaw, "Viscosities of Magmatic Silicate Liquids: An Empirical Method of Prediction," American Journal of Science, Vol. 272, pp. 870-893, 1972.

46. M. Ishii and N. Zuber, "Drag Coefficient and Relative Velocity in Bubbly, Droplet, or Particle Flows," AIChE Journal, Vol. 25, pp. 843-855, 1979.

47. J. E. Brockmann, F. E. Arellano, and D. A. Lucero, "Validation of Models of Gas Holdup in the CORCON Code," NUREG/CR-5433, December 1989.

48. M. L. Corradini, "A Transient Model for the Ablation and Decomposition of Concrete," Nucl. Tech., Vol. 62, pp. 263-273, 1983.

49. D. R. Bradley, "Modeling of Heat Transfer Between Core Debris and Concrete," 1988 National Heat Transfer Conf., July 24-28, 1988.

50. S. S. Kutateladze and I. G. Malenkov, "Boiling and Bubbling heat Transfer under the Conditions of free and Forced convection," 6th Int. Heat Transfer Conf., Toronto, Canada, 1978.

51. E. R. Copus, "Sustained Uranium Dioxide/Concrete Interaction Tests: The SURC Test Series," Proc. 2nd OECD (NEA) CSNI Specialist Meeting on Molten Core Debris-Concrete Interaction, Karlsruhe, Germany, April, 1992.

52. Revised American National Standard, 1979. Decay Heat Power in Light Water Reactors, ANSI/ANS-5.1-1979.

APPENDIX A:
BIBLIOGRAPHY OF MCCI PROJECT PUBLICATIONS

Journal Publications

1. S. Lomperski, M. T. Farmer, and S. Basu, "Experimental Investigation of Corium Quenching at Elevated Pressure," Accepted for Publication in Nuclear Eng. Design, December, 2003.

Conference Proceedings

1. M. T. Farmer, S. Lomperski, and S. Basu, "The Results of the CCI-3 Reactor Material Experiment Investigating 2-D Core-Concrete Interaction and Debris Coolability," Proceedings ICAPP '06, Reno, Nevada, June 6-8, 2006.

2. S. Basu, M. T. Farmer, and S. Lomperski, "Significance of the OECD-MCCI Program in Relation to Severe Accident Uncertainties Evaluation," CSNI Workshop on Evaluation of Uncertainties in Relation to Severe Accidents and Level 2 Probabilistic Safety Analysis, Aix-en-Provence, France, 7-9 November, 2005.

3. M. T. Farmer, S. Lomperski, and S. Basu, "The Results of the CCI-2 Reactor Material Experiment Investigating 2-D Core-Concrete Interaction and Debris Coolability," 11th International Topical Meeting on Nuclear Reactor Thermal-Hydraulics (NURETH-11), Avignon, France, October 2-6, 2005.

4. M. T. Farmer, S. Lomperski, and S. Basu, "Status of the Melt Coolability and Concrete Interaction (MCCI) Program at Argonne National Laboratory," Proceedings ICAPP '05, Seoul, Korea, May 15-19, 2005.

5. M. T. Farmer, S. Lomperski, and S. Basu, "Results of Reactor Material Experiments Investigating 2-D Core-Concrete Interaction and Debris Coolability," Paper 4102, Proceedings ICAPP '04, Pittsburgh, PA USA, June 13-17, 2004.

MCCI-Program Technical Reports

1. M. T. Farmer, S. Lomperski, D. J. Kilsdonk, and R. W. Aeschlimann, "OECD MCCI Project Final Report," OECD/MCCI-2005-TR06, February 28, 2006.

2. M. T. Farmer, S. Lomperski, D. J. Kilsdonk, and R. W. Aeschlimann, "OECD MCCI Project 2-D Core Concrete Interaction (CCI) Tests: Final Report," OECD/MCCI-2005-TR05, February 28, 2006.

3. M. T. Farmer, S. Lomperski, D. J. Kilsdonk, R. W. Aeschlimann, "2-D Core Concrete Interaction (CCI) Tests: CCI-3 Test Data Report-Thermalhydraulic Results," Rev. 0, OECD/MCCI-2005-TR04, October 15, 2005.

4. S. Lomperski, M. T. Farmer, D.J. Kilsdonk, and R. W. Aeschlimann, “Small-Scale Water Ingression and Crust Strength Tests (SSWICS) SSWICS Final Report: Thermal Hydraulic Results,” OECD/MCCI-2005-TR03, June 2005.

5. S. Lomperski, M. T. Farmer, D. J. Kilsdonk, and R. W. Aeschlimann, “Project Small-Scale Water Ingression and Crust Strength Tests (SSWICS) SSWICS Final Report: Crust Strength Measurements,” OECD/MCCI-2005-TR02, June 2005.

6. S. Lomperski, M. T. Farmer, D. J. Kilsdonk, and R. W. Aeschlimann, “Small-Scale Water Ingression and Crust Strength Tests (SSWICS); SSWICS-7 Test Data Report: Thermalhydraulic Results,” Rev. 0, OECD/MCCI-2005-TR01, January 11, 2005.

7. M. T. Farmer, S. Lomperski, D. J. Kilsdonk, R. W. Aeschlimann, and S. Basu, “2-D Core Concrete Interaction (CCI) Tests: CCI-2 Test Data Report-Thermalhydraulic Results,” Rev. 0, OECD/MCCI-2004-TR05, October 15, 2004.

8. S. Lomperski, M. T. Farmer, D. J. Kilsdonk, and R. W. Aeschlimann, “Small-Scale Water Ingression and Crust Strength Tests (SSWICS); SSWICS-6 Test Data Report: Thermalhydraulic Results,” Rev. 0, OECD/MCCI-2004-TR03, March 19, 2004.

9. M. T. Farmer, S. Lomperski, D. J. Kilsdonk, R. W. Aeschlimann, and S. Basu, “2-D Core Concrete Interaction (CCI) Tests: CCI-1 Test Data Report-Thermalhydraulic Results,” Rev. 0, OECD/MCCI-2004-TR01, January 31, 2004.

10. M. T. Farmer, D. J. Kilsdonk, S. Lomperski, R. W. Aeschlimann, and S. Basu, “2-D Core Concrete Interaction (CCI) Tests: CCI-2 Test Plan,” Rev. 0, OECD/MCCI-2004-TR02, January 31, 2004.

11. S. Lomperski, M. T. Farmer, D. J. Kilsdonk, and R. W. Aeschlimann, “SSWICS-5 Test Data Report – Thermalhydraulic Results,” Rev. 0, OECD/MCCI-2003-TR06, October 22, 2003.

12. M. T. Farmer, D. J. Kilsdonk, P. Pfeiffer, and S. Lomperski, “Crust Failure Test Design Report,” Rev. 0, OECD/MCCI-2003-TR05, March 31, 2003.

13. S. Lomperski, M. T. Farmer, D. J. Kilsdonk, and R. W. Aeschlimann, “Small-Scale Water Ingression and Crust Strength Tests (SSWICS); SSWICS-4 Test Data Report: Thermalhydraulic Results,” Rev. 0, OECD/MCCI-2003-TR05, March 21, 2003.

14. S. Lomperski, M. T. Farmer, D. J. Kilsdonk, and R. W. Aeschlimann, “Small-Scale Water Ingression and Crust Strength Tests (SSWICS); SSWICS-3 Test Data Report: Thermalhydraulic Results,” Rev. 0, OECD/MCCI-2003-TR03, February 19, 2003.

15. S. Lomperski, M. T. Farmer, D. J. Kilsdonk, and R. W. Aeschlimann, “Small-Scale Water Ingression and Crust Strength Tests (SSWICS); SSWICS-2 Final Data Report,” Rev. 0, OECD/MCCI-2003-TR02, February 12, 2003.

16. S. Lomperski, M. T. Farmer, D. J. Kilsdonk, and R. W. Aeschlimann, "Small-Scale Water Ingression and Crust Strength Tests (SSWICS); SSWICS-1 Final Data Report," Rev. 1, OECD/MCCI-2003-TR01, February 10, 2003.

17. M. T. Farmer, S. Lomperski, D. J. Kilsdonk, and R. W. Aeschlimann, "Long-Term 2-D Molten Core Concrete Interaction Test Design Report," Rev. 0, OECD/MCCI-2002-TR05, September 30, 2002.

18. S. Lomperski, M. T. Farmer, D. J. Kilsdonk, and R. W. Aeschlimann, "SSWICS-1 Test Data Report – Thermalhydraulic Results," Rev. 0, OECD/MCCI-2002-TR04, September 20, 2002.

19. S. Lomperski, M. T. Farmer, D. J. Kilsdonk, and R. W. Aeschlimann, "SSWICS-2 Test Data Report – Thermalhydraulic Results," Rev. 0, OECD/MCCI-2002-TR06, September 20, 2002.

20. M. T. Farmer, S. Lomperski, D. J. Kilsdonk, and R. W. Aeschlimann, "Melt Eruption Test (MET) Design Report," Rev. 1, OECD/MCCI-2002-TR03, October 12, 2002.

21. M. T. Farmer, S. Lomperski, D. J. Kilsdonk, R. W. Aeschlimann, and P. Pfeiffer, "Small-Scale Water Ingression and Crust Strength Tests (SSWICS) Design Report," Rev. 2, OECD/MCCI-2002-TR01, October 31, 2002.

22. S. Lomperski, "Enhancing Instrumentation for Reactor Material Experiments," OECD/MCCI-2002-TR02, September 3, 2002.

NRC-Sponsored Technical Reports and Conference Proceedings

1. M. T. Farmer, "Phenomenological Modeling of the Melt Eruption Cooling Mechanism During Molten Core-Concrete Interaction," Proc. ICAPP '06, Reno, Nevada, June 6-8, 2006.

2. M. T. Farmer, J. J. Sienicki, and A. Kovtonyuk, "OECD MCCI Analytical Support (Stand Alone Task): Water Ingression Modeling of the OECD/MCCI SSWICS Tests," NRC/MCCI/2003-TR01, October 15, 2003.

3. H. Ley, "MELCOR Parameter Studies for 2-D Molten Core Concrete Interaction Experiments," September 30, 2002.